

UCSF

UC San Francisco Electronic Theses and Dissertations

Title

Modeling and treating chemotherapy-induced gastrointestinal neurotoxicity

Permalink

<https://escholarship.org/uc/item/4p93c8z9>

Author

Richter, Mikayla Noelle

Publication Date

2023

Peer reviewed|Thesis/dissertation

Modeling and treating chemotherapy-induced gastrointestinal neurotoxicity

by
Mikayla Richter

DISSERTATION
Submitted in partial satisfaction of the requirements for degree of
DOCTOR OF PHILOSOPHY

in
Pharmaceutical Sciences and Pharmacogenomics

in the
GRADUATE DIVISION
of the
UNIVERSITY OF CALIFORNIA, SAN FRANCISCO

Approved:

DocuSigned by:

Hani Goodarzi

Hani Goodarzi

FDD44359FCC6487...

Chair

DocuSigned by:

Seyedeh Faranak Fattahi

Seyedeh Faranak Fattahi

DocuSigned by:

Bruce Conklin

Bruce Conklin

DocuSigned by:

Deanna Kroetz

Deanna Kroetz

0611A116B51E4AA...

Committee Members

Copyright 2022

by

Mikayla Richter

Dedication

I dedicate this dissertation to my father, Dale R. Richter, who was diagnosed with esophageal cancer in 2002. After undergoing radiation therapy, cisplatin and fluorouracil chemotherapy, and an esophagectomy, he has been cancer-free for the past 20 years, as of writing this dissertation. He lives with the adverse consequences of his cancer treatment every day. His resilience and perseverance are an inspiration to me.

Acknowledgements

I first would like to acknowledge my PhD advisor and mentor Dr. Faranak Fattahi. Your support, optimism, and confidence in both me and my research has never wavered and has buoyed me through the hardest times of my graduate training. I look forward to our future collaborations and opportunities to continue to learn from you both as a scientist and as a person.

Thank you to the Fattahi lab, which I've seen grow from a handful of people in 2018 to the dynamic and lively lab it is today. Over the years you have become like family; I have spent more waking hours with you than anyone else in my life. Thank you for being the biggest supporters and cheerleaders of my research. Nearly everyone directly helped with some aspect of my dissertation project and the research was better for it.

I would like to acknowledge my dissertation committee members. Dr. Hani Goodarzi is not only my dissertation committee chair but has been a longstanding collaborator and supporter of my research and ideas. Thank you for normalizing my PhD experience and always treating me like a colleague rather than a student. Dr. Deanna Kroetz was my program director and my second mentor throughout my PhD experience. As a first year PhD student, she guided me to Faranak. Thank you for always making yourself available to meet with me and discuss aspects of my project, providing your unique perspective. Besides being my dissertation committee member, Dr. Bruce Conklin was also my qualification exam committee chair. Bruce, you have the unique ability to focus

what seems like over 100% of your attention on me and my project when we meet.

Thank you for always finding ways to make me more excited and motivated about my research than I was before.

I want to thank the Pharmaceutical Sciences and Pharmacogenomics PhD program and my cohort of fellow students. I consider myself lucky to be in a program that permits so much student involvement and feedback. Throughout my PhD I have participated on the curriculum committee, the diversity, equity, and inclusion committee, the admissions and recruitment committees, and have been a retreat and alumni event organizer.

These experiences have given me opportunities to explore and practice skills not acquirable through benchwork and have made me into a stronger and more confident leader and collaborator. To my fellow cohort, I held onto you all like a life raft through my first two years. Thank you for normalizing and validating my experience at every turn.

I would like to acknowledge my family who have been uniquely supportive and engaged in my research. Nearly every year throughout my PhD, you have listened to the latest version of my research talk and are always excited to hear about updates. My mom, Susan L. Richter and my stepdad, Sean S. Baker are the only parents I know of that attended their child's practice qualification exam. Everyone in my family has seen the lab and seen my cells and science first-hand. Throughout my academic career, my eldest sibling, Kris R. Richter, has proofread nearly everything I have written. Every time I'm complimented on my writing skills, I have you to thank. My brother, Ryan M. Richter,

is the original science nerd of the family. Thank you for being a role model of scientific curiosity for me at a young age and always being excited to discuss new topics you or I have learned. Mom and Sean, you were the first to introduce me to the gut-brain axis. I remember calling you after first meeting Faranak and essentially deciding in that moment that I would join the lab; we were so excited about the research and uncovering the molecular mechanisms of conditions you have encountered for years as trauma therapists.

I would like to thank my cat, King Curtis, who slept on my lap for the majority of writing this dissertation. For that, I consider you a co-author. Thank you for choosing me as your owner, being a true source of unconditional love, and providing me (and others) with never ending entertainment and joy over the years.

Lastly, I would like to thank my partner Danny M. Wilson Jr, Esq. After starting our graduate school application journey in 2016 (yours for law schools, mine for PhD programs) we both are finally done! Thank you for being my family, supporting me in every way throughout our relationship, but especially over the past few years. You've heard every fear, every failure, every success. You are my rock. Thank you for going through this life with me.

Contributions

Chapter 2 of this dissertation contains material under review at a peer-reviewed journal. Therefore, the content here may differ from the final published form. Sina Farahvashi performed the immunostaining of the paraffin-embedded human stomach sections and assisted with the mouse assays and tissue preparation. Ryan M Samuel performed the phosphorylated protein kinase C distribution analysis and assisted with the single nuclei RNA sequencing data analysis. Homa Majd, PhD assisted with *in vitro* experiments, protein-protein interaction network analysis, preparation of paraffin-embedded human stomach sections, and mouse assays and tissue preparation. Angeline K Chemel assisted with the mouse assays and tissue preparation. Alireza Majd, MD and Megan D Scantlen assisted with the mouse assays. Andrius Cesiulis assisted with the single nuclei RNA sequencing data analysis and mouse tissue preparation. Kristle Garcia, Tanvi Joshi, and Keyi Yin performed injections for the mouse experiment and assisted with mouse assays. Matthew G Keefe performed microelectrode array data curation. Bardia Samiakalantari assisted with colorectal cancer cell line experiments. Elena M Turkal assisted with quantifying CHRM3 and CHRM5 protein levels in CHRM3 and CHRM5 CRISPR ribonucleoprotein targeted cell lines by Western blot. Johnny Yu, PhD assisted with bulk RNA sequencing library preparation. Abolfazl Arab performed bulk RNA sequencing data curation. Bruce Culbertson assisted with acquiring and establishing cancer cell lines. Bianca Vora, PhD assisted with UCSF Research Data Browser analysis. Chenling Xiong, PhD assisted with neurite length analysis. Michael G Kattah, MD, PhD acquired the paraffin-embedded human stomach sections. Roshanak Irannejad, PhD assisted with the cell viability assays.

Modeling and treating chemotherapy-induced gastrointestinal neurotoxicity

Mikayla N. Richter

Abstract

In recent years, the complexity of chemotherapies and their interactions with the peripheral nervous system have come into focus but limitations in experimental models have remained a significant challenge in the field. As evidence, despite most chemotherapy drugs being around for decades, there are currently no therapies approved that target chemotherapy-peripheral nervous system interactions as an anti-neurotoxic agent. Human pluripotent stem cells offer an appealing model system that, unlike rodent models, are compatible with high throughput, high content applications that reflect modern drug discovery methodologies. Thus, utilizing the key advantages of stem cell-based models in tandem with the strengths of traditional animal models offers a complementary and interdisciplinary strategy to advance chemotherapy-peripheral nervous system research and drug discovery.

This dissertation begins with an overview of the current status of chemotherapy-peripheral nervous system research, describing examples of taxane chemotherapy-induced damage to sensory nerves and platin chemotherapy-induced damage to enteric nerves. Avenues where stem cell-based models may further advance the field are also presented. Based on this foundation, I established a stem cell-based model of

chemotherapy-induced enteric neuropathy, focusing my efforts on the platinum chemotherapy drug class as they are heavily prescribed and highly neurotoxic to enteric neurons, which innervate and control the gastrointestinal tract.

To uncover the mechanism of platinum-induced gastrointestinal neurotoxicity, I leveraged my scalable stem cell-derived enteric neuron model, performing high throughput screens and transcriptomic analyses to reveal excitotoxicity through muscarinic cholinergic signaling as a key driver of platinum-induced enteric neuropathy. Single nuclei transcriptomics identified inhibitory nitrergic neurons as selectively vulnerable to platinum, which we validated through histological analysis of the enteric nervous system in platinum chemotherapy-treated patients. Lastly, we found that dampening muscarinic signaling through either pharmacologic or genetic methods is sufficient to prevent platinum-induced excitotoxicity *in vitro* and platinum-induced constipation and degeneration of nitrergic neurons in mice.

Altogether, this work succeeds in defining a therapeutic mechanism capable of preventing platinum-induced gastrointestinal neurotoxicity. Furthermore, it serves as an example and framework for how stem cell-based models of the peripheral nervous system can be utilized to rapidly deconvolute mechanisms of chemotherapy-induced neurotoxicity and power drug discovery pipelines to tackle numerous peripheral neuropathies that have been intractable to date.

Table of Contents

Chapter 1 Stem cell-based models for studying the effects of chemotherapeutic drugs on the peripheral nervous system	1
1.1 Introduction	1
1.2 Technical challenges and translational limitations of studying the peripheral nervous system in animals	2
1.3 Chemotherapy	4
1.3.1 The sensory nervous system: paclitaxel	7
1.3.2 The enteric nervous system: oxaliplatin	10
1.4 Leveraging stem cell-based models and animals to advance chemotherapy-peripheral nervous system research.....	13
Chapter 2 Inhibition of muscarinic receptor signaling protects human enteric inhibitory neurons against platin chemotherapy toxicity	15
2.1 Abstract.....	15
2.2 Introduction	16
2.3 Results	19
2.3.1 Enteric neurons are directly susceptible to platin chemotherapies	19
2.3.2 Phenotypic screen identifies platin-induced excitotoxicity mechanism	31
2.3.3 Muscarinic cholinergic signaling promotes platin-induced enteric neurotoxicity	39

2.3.4 Enteric nitrergic neurons are selectively vulnerable to platin-induced excitotoxicity	46
2.3.5 Oxybutynin prevents oxaliplatin-induced enteric neuropathy in mice	60
2.6 Tables	66
2.7 Methods	74
Chapter 3 Concluding Remarks	104
3.1 Overview of our findings	104
3.2 Perspectives and future directions.....	108
References	111

List of Figures

Figure 1.1 Chemotherapy adverse reactions.	6
Figure 2.1 Evaluating platin-induced neurotoxicity in patient data and hPSC-derived enteric and control peripheral neurons.....	21
Figure 2.2 Enteric neurons are selectively vulnerable to platin chemotherapies	24
Figure 2.3 High throughput screen uncovers mechanism of platin-induced excitotoxicity in enteric neurons	32
Figure 2.4 Effect of drug screen hits on platin antineoplastic efficacy and G _i protein inhibitor on platin-induced enteric neuropathy.....	35
Figure 2.5 Reducing muscarinic cholinergic receptor signaling prevents platin-induced excitotoxicity in enteric neurons.....	41
Figure 2.6 Effect of muscarinic antagonism on platin toxicity hallmarks and CHRM3 and CHRM5 CRISPR-cas9 targeted hPSC-derived enteric neuron characterization	43
Figure 2.7 Single nuclei transcriptomic profiling identifies subtypes susceptible to platin-induced excitotoxicity.....	47
Figure 2.8 hPSC-derived 2D enteric neurons recapitulate human enteric neuron neurochemical diversity.....	49
Figure 2.9 Cell type specific transcriptional profiling of platin-induced excitotoxicity susceptibility	55
Figure 2.10 Selective loss of nitrergic enteric neurons during platin treatment can be prevented by oxybutynin	62

List of Tables

Table 1.1 Chemotherapy drug classes and adverse reactions from package inserts.....	5
Table 2.1 Characteristics of individuals with colorectal cancer extracted from UCSF Research Data Browser	66
Table 2.2 Characteristics of individuals with ovarian cancer extracted from UCSF Research Data Browser	66
Table 2.3 Prevalence of constipation in patients that received platin chemotherapy and untreated patients.....	67
Table 2.4 Cytokine array results showing average MFI (n=3) normalized to vehicle	67
Table 2.5 List of predicted drug targets using compound-protein interaction analysis...	69
Table 2.6 List of predicted targets for experimentally validated hit compounds.....	70
Table 2.7 List of transcripts and functional categories in excitotoxicity transcriptional program	70
Table 2.8 List of quality control metric cutoffs for the snRNAseq dataset.....	71
Table 2.9 Principal components used for SNN and UMAP calculation and the resolution used for clustering of each dataset.....	71
Table 2.10 List of transcripts used to define neurochemical identities	72
Table 2.11 List of antibodies	73

List of Abbreviations

PNS: peripheral nervous system

hPSC: human pluripotent stem cell

SARS-CoV-2: severe acute respiratory syndrome coronavirus 2

GWAS: genome wide association studies

GI: gastrointestinal

ENS: enteric nervous system

LDH: lactate dehydrogenase

CCCP: carbonyl cyanide m-chlorophenyl hydrazone

GSEA: gene set enrichment analysis

GROA: C-X-C motif chemokine ligand 1

I309/CCL1: chemokine C-C motif ligand 1

IL8/CXCL8: interleukin-8

MCP3/CCL7: chemokine C-C motif ligand 7

MIF: macrophage migration inhibitory factor

SFAS/TNFRSF6: tumor necrosis factor receptor superfamily member 6

TGFA: transforming growth factor alpha

BCA1/CXCL13: chemokine C-X-C motif ligand 13

TUBB3: tubulin beta 3 class III

iPSC: induced pluripotent stem cell

ESC: embryonic stem cell

SMILES: simplified molecular-input line-entry system

SEA: similarity ensemble approach

GPCRs: G protein-coupled receptors

PLC: phospholipase C

PIP2: phosphatidylinositol biphosphate

IP3: triphosphate

DAG: diacylglycerol

PKC: protein kinase C

CHRM1: muscarinic cholinergic receptor 1

CHRM3: muscarinic cholinergic receptor 3

CHRM5: muscarinic cholinergic receptor 5

TUNEL: terminal deoxynucleotidyl transferase dUTP nick end labeling

RNPs: CRISPR-cas9 ribonucleoproteins

snRNA-seq: single nuclei RNA sequencing

NO: nitric oxide

OR: odds ratio

UKBB: UK Biobank

p-PKC: phosphorylated protein kinase C

ENC: enteric neural crest

PCA: Principal Components Analysis

UMAP: Uniform Manifold Approximation and Projection

SNN: shared nearest neighbors

BSA: bovine serum albumin

Chapter 1 Stem cell-based models for studying the effects of chemotherapeutic drugs on the peripheral nervous system

1.1 Introduction

To date the interfaces between chemotherapeutic drugs and the peripheral nervous system (PNS) have been primarily studied in animal models or primary tissue samples harvested from animals. These studies have provided the field with key insights including uncovering key pathological phenotypes and the potential proteins involved in drug-induced peripheral neuropathies. However, despite these advancements, these traditional models have failed to deliver any therapies approved to target and prevent these adverse events. For example, despite many neurotoxic chemotherapeutics being on the market for decades, there are no treatments available that prevent or ameliorate their effects on the nervous system. These clinical failings are largely due to the technical challenges and translational limitations of the experimental models routinely used for studying PNS disorders. To make research in the evolving area of chemotherapy-induced peripheral neuropathy more translational and compatible with drug discovery, an interdisciplinary approach utilizing tools that span cancer biology, developmental biology, functional genomics, neuroscience, and pharmacology must be employed. Here, human stem cell derived cultures are discussed as exciting model systems that may help incorporate novel methodologies into chemotherapy-PNS research.

1.2 Technical challenges and translational limitations of studying the peripheral nervous system in animals

The PNS is inaccessible. Unlike the brain, the PNS is diffuse throughout the body and innervates all vital organs. This makes isolating pure populations of specific peripheral nerve or glia subtypes from animals technically challenging. For example, many sympathetic and parasympathetic ganglia do not reside in the spinal cord but rather reside adjacent to the tissue the nerve innervates¹. Moreover, enteric neurons reside solely within the gastrointestinal (GI) tract, where they make up 1% of the tissue². The inaccessibility of these divisions of the PNS makes them extremely difficult to isolate and study at large scale. Therefore, deriving these tissues *in vitro* using human pluripotent stem cell (hPSC) technology offers an elegant and feasible solution to access these inaccessible cell types.

Although genetically similar, mice are not humans. Mouse models have been extremely effective for drug discovery in the context of oncology. However, diseases affecting the PNS have not experienced the same clinical success. In the past twenty years, over eighty clinical trials for amyotrophic lateral sclerosis, a progressive motor neuron disease, have been conducted, yet currently there are no effective treatments that can prevent disease progression³. These clinical failures are driven by the absence of models that properly replicate human PNS disease phenotypes and pathologies, leading to an incomplete understanding of key pathogenic pathways. Therefore, to discover and develop novel therapies that are effective in humans, PNS disease research must

incorporate tools that better recapitulate human tissue biology and protein dynamics. Given that tissue from human surgical or post-mortem samples is limited, hPSC-derived tissue offers a suitable solution to model and study human PNS biology at the cellular level. Furthermore, with that advancement of induced pluripotent stem cell technology, stem cell models can be generated from any individual. This has improved the ability of scientists to capture inter-individual genetic variability in their derived tissues and study cellular biology in the genetic context of an affected patient.

Mouse models and primary tissue samples are low throughput and therefore incompatible with newer high throughput methodologies such as pharmacologic or genetic screening. Leveraging hPSCs, it is now possible to derive human tissues at large scale that are compatible with high throughput screening technologies, which in recent years have been critical for uncovering biological mechanisms and druggable targets. Within the PNS, large-scale screens of hPSC-derived neural crest and enteric neural crest cells have helped to uncover mechanisms underlying *IKBKAP* expression in familial dysautonomia and enteric neural crest migration in Hirschsprung's disease, respectively^{4,5}. More broadly, high throughput screens of hPSC-derived cardiomyocytes helped to identify androgen signaling as a key regulator of *ACE2* expression enabling severe acute respiratory syndrome coronavirus 2 (SARS-CoV-2) viral entry and nominate antiadrenergic drugs as an effective therapeutic strategy for SARS-CoV-2⁶. Together, these examples emphasize how hPSC technology can help rapidly advance drug discovery efforts in chemotherapy-PNS research.

Thus, utilizing the key advantages of stem cell-based models in tandem with the strengths of traditional animal models offers a complementary strategy to uncover mechanisms and pharmacological modulators of chemotherapy-PNS interactions. Conducting research with these two model systems offers tremendous hope toward advancing drug discovery and development pipelines in this field.

1.3 Chemotherapy

Traditional methods of cancer therapy, such as radiation and chemotherapy have been around for decades, yet their adverse effects, particularly on the PNS, remain poorly understood. Chemotherapeutic drugs largely target DNA replication mechanisms, thereby blocking tumor growth and cancer progression (Table 1.1). Given that all human tissues contain DNA, it is not surprising that chemotherapies have many off-target effects on healthy tissues. However, despite sharing a general mechanism of DNA damage, the specific organs and tissues affected varies broadly across different molecules (Table 1.1). Furthermore, the mechanisms underlying this variability remain unidentified and there are no available biomarkers that can predict toxicity risk or measure toxicity severity.

Table 1.1 Chemotherapy drug classes and adverse reactions from package inserts

Drug Class	Mechanism of Action	Examples	Vulnerable Tissues
Alkylating	Directly binds and damages the DNA	Oxaliplatin	Bone marrow Gastrointestinal tract Liver Lung Sensory nerves
Antimetabolites	Integrates into DNA, making it unreadable and uncopiable	5-fluorouracil	Bone marrow Brain Gastrointestinal tract Heart Skin
Anthracyclines	Blocks enzymes involved in DNA replication	Daunorubicin	Bone marrow Gastrointestinal tract Heart Skin
Topoisomerase inhibitors	Blocks topoisomerases, preventing DNA separation during replication	Irinotecan	Bone marrow Gastrointestinal tract Immune system ^{a)} Kidneys Liver Lungs Skin
Taxanes	Stabilizes microtubules, preventing cell division	Paclitaxel	Bone marrow Gastrointestinal tract Heart Immune system ^{a)} Liver Motor nerves Sensory nerves Skin

^{a)}Immune system includes hypersensitivity reaction

Neurotoxicity is a common adverse reaction that spans every class of chemotherapy. However, the neurotoxic effects are varied, affecting the sensory nervous system, motor nervous system, enteric nervous system (ENS), or some combination of the three. The ENS innervates and controls the GI tract⁷. Notably, the GI tract is the most impacted by chemotherapy treatment, with virtually every chemotherapy causing some form of GI

toxicity (Figure 1.1). This includes chemotherapy-induced diarrhea and chemotherapy-induced constipation, common motility disorders which have recently been linked with chemotherapy-induced damage to the ENS^{8–11}. Additionally, chemotherapy-induced sensory neuropathy and motor neuropathy can cause pain and numbness in the extremities and muscle weakness, respectively¹². Notably, in most cases these chemotherapy-induced forms of peripheral neuropathy are dose dependent and can be irreversible. Given the high burden of these disorders on the quality of life of patients and cancer survivors, research efforts must be invested in preventing and treating these side effects.

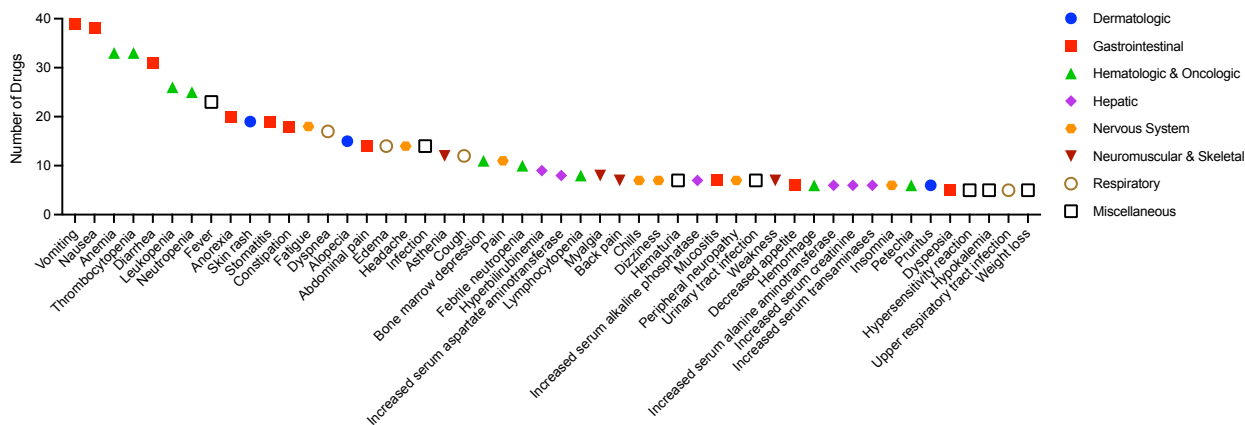


Figure 1.1 Chemotherapy adverse reactions. Includes adverse reactions that affect >10% of patients across 43 chemotherapeutic drugs.

The promise of stem cell-based modeling to uncover mechanisms of chemotherapy-induced toxicity and to predict chemotherapy-induced side effects has been demonstrated for anthracyclines. Anthracyclines, such as doxorubicin and daunorubicin, are cardiotoxic and can cause heart failure. By differentiating patient derived hPSCs into cardiomyocytes and treating them with doxorubicin, key pathways underlying

doxorubicin-induced cardiotoxicity have been uncovered. These pathways include decreased mitochondrial and metabolic function, calcium handling, and antioxidant pathway activity, all of which ultimately decrease cardiomyocyte viability¹³. Additionally, by detecting microRNAs released by hPSC-derived cardiomyocytes treated with doxorubicin, novel biomarkers of myocardial damage have been identified for doxorubicin-induced cardiotoxicity¹⁴. Unfortunately, little is known about the mechanisms of chemotherapy-induced peripheral neuropathy and there are no methods available to predict a patient's risk for neurotoxicity. Furthermore, few groups have used stem cell-based models to address these gaps. However, paclitaxel-induced sensory neuropathy and oxaliplatin-induced enteric neuropathy have been studied extensively, and the current status of these two indications will be discussed.

1.3.1 The sensory nervous system: paclitaxel

Paclitaxel is a taxane chemotherapy which promotes the assembly of microtubules thereby preventing depolymerization, an activity required for mitosis¹⁵. This mechanism of action therefore halts cancer cell division and progression. Paclitaxel was approved for breast and ovarian cancers in 1994. It has become a first line therapy for these indications and has been further developed into an albumin-bound product, nab-paclitaxel¹⁶. Despite its clinical promise, paclitaxel's most common and dose-limiting side effect is sensory neuropathy. Over 50% of patients given paclitaxel experience symptoms of sensory neuropathy, including tingling, numbing, or burning pain in the extremities, particularly the hands and feet¹⁷⁻¹⁹. This neurotoxicity is dose-dependent and progressive, such that

larger cumulative doses of paclitaxel increase the risk of developing sensory neuropathy or more severe symptoms of sensory neuropathy, which can be irreversible¹⁷⁻¹⁹. There are currently no effective treatments that can prevent paclitaxel-induced neurotoxicity, other than reducing the drug dose or discontinuing treatment^{18,19}. Therefore, physicians and patients must balance the curative benefit of the chemotherapy with the tissue damage the therapy incurs.

Recent approaches to uncover proteins involved in paclitaxel-induced sensory neuropathy include the use of isolated rodent dorsal root ganglia neurons, *in vivo* rodent studies, and human genome wide association studies (GWAS)^{18,19}. *In vitro* rodent studies utilizing embryonic sensory neurons isolated from the dorsal root ganglia have identified multiple proteins linked with paclitaxel-induced changes in neuronal sensitivity, excitability, and axonal degeneration¹⁹. Aberrant calcium signaling mediated via toll like receptor 4, B-cell lymphoma-w, and inositol 1,4,5-trisphosphate receptor type 1 leads to calpain-dependent axonal fragmentation in paclitaxel treated cells^{20,21}. GWAS studies, on the other hand, have identified single nucleotide polymorphisms in the DNA of patients that experience paclitaxel-induced sensory neuropathy. These variants map to proteins involved in RhoGTPase signaling pathways which are essential for axonal guidance and neuronal extension¹⁸. This suggests that patients with variants that are more prone to axonal degeneration or have reduced regenerative properties may be more susceptible to peripheral neuropathy. These findings have led to the identification of novel drug targets for paclitaxel-induced sensory neuropathy that are currently being evaluated in the clinic (NCT03941643, NCT03943498). These *in vitro*, *in vivo*, and pharmacogenomic

findings highlight the polygenic nature of paclitaxel-induced sensory neuropathy. These studies do not converge on a single protein that causes the toxicity, but multiple proteins involved in axon maintenance. This suggests that nominating an effective drug target may not be as simple as drugging a hit from a single experiment or GWAS study, but perhaps a protein that regulates the shared protein network.

Stem cell-based models of paclitaxel-induced sensory neuropathy have recently been established²²⁻²⁴. Via a two week differentiation protocol, sensory neurons that replicate the transcriptional and functional properties of their *in vivo* counterparts can be derived from hPSCs²⁵. Leveraging this model to study paclitaxel-induced sensory neuropathy, two groups have established that their stem cell-based models can robustly recapitulate hallmarks of paclitaxel-induced neurotoxicity, including reduced viability, ineffective mitochondrial transport, aberrant neuron electrophysiology, and extensive neurite degeneration in a dose-dependent and time-dependent manner. Moreover, these models can validate the functional importance of proteins identified via unbiased GWAS. For example, *S1PR1* (sphingosine-1-phosphate receptor 1) is associated with chemotherapy-induced sensory neuropathy²⁴. Notably, when a sphingosine-1-phosphate receptor 1 functional antagonist is dosed in combination with paclitaxel in hPSC-derived sensory neurons, the antagonist reduces the extent of paclitaxel-induced neurite degeneration²⁴. This is the first example of its kind, validating the functional role of a protein in chemotherapy-induced sensory neuropathy and demonstrates the promise of utilizing stem cell-based models to advance chemotherapy-PNS research.

1.3.2 The enteric nervous system: oxaliplatin

Oxaliplatin is a chemotherapeutic drug within the alkylating drug class, meaning that it directly binds and disrupts DNA, triggering DNA damage response pathways that ultimately lead to cell death if the damage is overwhelming²⁶. Oxaliplatin was approved for colorectal cancer in 2004 and, due to the prevalence of colorectal cancer in recent years, is one of the most prescribed chemotherapies on the market. Despite its clinical utility, oxaliplatin is neurotoxic, particularly in the ENS, causing chemotherapy-induced diarrhea in over 40% of patients and chemotherapy-induced constipation in over 30% of patients, as reported in its package insert. Moreover, 49% of patients report continuing symptoms post-treatment, indicating the neuropathy is irreversible²⁷. However, a robust longitudinal analysis of chemotherapy-induced diarrhea, constipation, or other GI disorders related to the ENS is lacking. Despite being approved for nineteen years, there are no therapies approved to prevent or treat oxaliplatin-induced enteric neuropathy.

Oxaliplatin causes GI dysmotility by directly damaging enteric neurons in the GI tract. Oxaliplatin causes mitochondrial stress, increasing reactive oxygen species levels and disrupting mitochondrial membrane integrity^{8,9}. The overall number of enteric neurons is reduced by oxaliplatin^{8-10,28}. Likewise, enteric glia cells are also affected by oxaliplatin, increasing S100 β and decreasing GFAP levels in the ileum²⁸. However, it is unclear how these hallmarks relate to enteric glial cell biology and ENS function during oxaliplatin treatment. Notably other healthy tissues, such as those residing in the mucosa, are unaffected by oxaliplatin⁸. Ultimately, oxaliplatin causes colonic motility to become

increasingly ineffective in mice, manifesting in the clinically relevant phenotype of constipation^{8,9}.

Enteric neurons are comprised of diverse neuronal subtypes, expressing every class of neurotransmitter and numerous neuropeptides in combinations unique to the ENS^{29,30}. The complexity and functional meaning of this neuronal diversity is not yet fully understood. Intriguingly, there is evidence oxaliplatin affects enteric neuron subtypes differently. For example, oxaliplatin affects the representation of enteric neuron populations and the functional properties of nitrergic neurons^{8,9}. Nitrergic neurons are inhibitory motor neurons within the ENS³¹. Notably, nitrergic neuron-mediated electrophysiological properties and motility phenotypes are disrupted following oxaliplatin treatment, indicating that inhibitory motor neuron functions may be specifically affected by oxaliplatin⁹. However, these effects have not been characterized at single cell resolution and it remains unclear if neuronal imbalances in proportion, neuron subtype functional changes, or the general loss of enteric neurons causes motility disturbances and clinical symptomatology.

These studies have solidified the link between the clinical manifestations of oxaliplatin-induced GI toxicity and cellular phenotypes of ENS toxicity, specifically enteric neuropathy. Unfortunately, despite building a robust *in vivo* model of oxaliplatin-induced enteric neuropathy, the protein pathways underlying the toxicity mechanism remain unidentified and no druggable targets have been nominated. Furthermore, the dynamics between oxaliplatin's mechanism of action and the toxicity hallmarks of oxaliplatin-

induced enteric neuropathy along with why certain enteric neurons may be affected over others are still unknown.

A method for deriving enteric neurons from hPSCs has recently been developed^{5,32,33}. Following a two week enteric neuron induction protocol and a one month neuronal maturation period, enteric neurons can be derived from hPSCs. These hPSC-derived enteric neurons express key lineage markers and include representation from all neuronal subtypes found in the ENS. Furthermore, stem cell derived enteric neuron progenitors are engraftable and can rescue GI motility in functionally impaired mice. Utilizing this *in vitro* ENS system, it is now feasible to establish a stem model of oxaliplatin-induced enteric neuropathy to uncover the mechanism of toxicity. This model is compatible with genetic and pharmacologic phenotypic high throughput screens which can enable identifying the protein network involved in the toxicity. The model may also be used to investigate the dynamics of drug toxicity. For example, determining how the proteins involved in the toxicity mechanism affect hallmarks of the toxicity, such as neuropathy, oxidative stress, mitochondrial membrane permeability, and electrophysiology. Furthermore, hPSC-derived enteric neurons will enable robust characterization of toxicity biomarkers, including factors released from damaged neurons or nerve conductance changes, allowing clinicians to more accurately measure oxaliplatin-induced enteric neuropathy occurrence and severity. Finally, with a robust understanding of the toxicity mechanism, druggable proteins capable of modulating the protein network may be identified and tested for safety and efficacy *in vivo*. These studies would provide incredible advancements towards understanding oxaliplatin-induced enteric neuropathy. Besides

offering strategies to prevent oxaliplatin toxicity in the clinic, it would also inform the development of new platin derivatives, with less toxic side effects.

1.4 Leveraging stem cell-based models and animals to advance chemotherapy-peripheral nervous system research

Many of the biological interactions between chemotherapies and the PNS remain to be uncovered. Much of the progress within this growing area of research has been accomplished with animal models. Animal models have many strengths including capturing the interfaces between multiple interconnected tissues and organ systems. Furthermore, animal models capture how these complex interactions are incorporated into behavioral or functional outcomes. This complexity is unmatched even by organoid models. Thus, animal models can clearly address how a mutation, drug, or gene editing tool manifests in an organism in all relevant tissues and how this manifests behaviorally or functionally.

However, this complexity can make it difficult to decipher experimental results since it is impossible to control for all the system-level interactions that occur in an organism. For example, it can be challenging to determine if results are due to direct or indirect effects on an organ or cell type. Additionally, as discussed at the beginning of this introduction, it can be difficult to isolate rare or diffuse cell types, such as peripheral nerves. Animal models may not accurately or reliably recapitulate disease symptomatology or pathology.

Lastly, animal models and their primary tissues are not scalable, making unbiased, high throughput analyses infeasible.

hPSC-based models have the potential to fill these gaps. By deriving peripheral nerve populations *in vitro*, rare or inaccessible cell types are now accessible. hPSC-derived PNS lineages are scalable and compatible with high throughput, high content applications. They are a human model which recapitulates the genetics, transcriptional properties, and cellular hallmarks of human disease, making it easier to decipher the role of specific cell types in a disease. Thus, stem cell-based models offer a major technological tool that may be adopted to advance chemotherapy-induced peripheral neuropathy research.

For my dissertation work in Chapter 2, I utilize a stem cell-based enteric neuron model system to uncover the mechanism of platin-induced enteric neuropathy. I then validate these *in vitro* findings using a mouse model. This work not only advances our understanding of this drug toxicity and how to prevent it, but also exemplifies how stem cell-based models and animal models can be used in a complementary manner to rapidly advance drug discovery for peripheral neuropathies.

Chapter 2 Inhibition of muscarinic receptor signaling protects human enteric inhibitory neurons against platin chemotherapy toxicity

2.1 Abstract

Gastrointestinal toxicity is a common dose-limiting adverse effect of platin chemotherapy treatment. Up to 50% of cancer survivors continue to experience symptoms of chronic constipation or diarrhea induced by their chemotherapy for many years after their treatment. This drug toxicity is largely attributed to damage to enteric neurons that innervate the gastrointestinal tract and control gastrointestinal motility. The mechanisms responsible for platin-induced enteric neurotoxicity and potential preventative strategies have remained unknown. Here, we use human pluripotent stem cell-derived enteric neurons to establish a new model system capable of uncovering the mechanism of platin-induced enteric neuropathy. Utilizing this scalable system, we performed a high throughput screen and identified drug candidates and pathways involved in the disease. Our analyses revealed that excitotoxicity through muscarinic cholinergic signaling is a key driver of platin-induced enteric neuropathy. Using single nuclei transcriptomics and functional assays, we discovered that this disease mechanism leads to increased susceptibility of specific neuronal subtypes, including inhibitory nitroergic neurons, to platins. Histological assessment of the enteric nervous system in platin-treated patients confirmed the selective loss of nitroergic neurons. Finally, we demonstrated that pharmacological and genetic inhibition of muscarinic cholinergic signaling is sufficient to rescue enteric neurons from platin excitotoxicity *in vitro* and can prevent platin-induced

constipation and degeneration of nitrergic neurons in mice. These studies define mechanisms of platin-induced enteric neuropathy and serve as a framework for uncovering cell type-specific manifestations of cellular stress underlying numerous intractable peripheral neuropathies.

2.2 Introduction

Platin chemotherapies, including cisplatin, carboplatin, and oxaliplatin, have been approved and used widely to treat cancer for decades. They inhibit cancer progression by binding DNA, forming DNA adducts that induce DNA strand breaks, which ultimately lead to cell death if the damage is overwhelming²⁶. This mechanism of action is highly effective at treating a variety of cancers. For example, since the introduction of cisplatin in 1978, the prognosis of testicular, ovarian, and bladder cancers has improved tremendously (Seer Cancer Statistics Review 1975-2015). Furthermore, platins are prescribed for highly prevalent cancers, including colorectal, lung, and bladder cancers, making up about 50% of all cancer patients³⁴. However, despite their clinical efficacy and applicability, a major adverse effect that limits the utility of platins is GI dysmotility, resulting from platin-induced damage to the ENS³⁵⁻³⁸.

The ENS is the division of the PNS embedded in the GI tract that regulates GI functions, including motility, secretion, and immune response³⁰. It contains a diverse network of neurons that express specific neurotransmitters and neuropeptides corresponding with distinct functional roles, including excitatory and inhibitory activity²⁹. Responding to local

stimuli in the lumen, the ENS neuronal network coordinates the contraction and relaxation of smooth muscle fibers to orchestrate complex patterns of motility in different parts of the GI tract. Disruptions to one or more components of the circuit can lead to motility disorders including achalasia, gastroparesis, intestinal pseudo-obstruction, chronic constipation, or chronic diarrhea³⁹⁻⁴¹.

Platin-induced GI toxicities replicate many symptomatic aspects of GI motility disorders, including, most commonly, platin-induced constipation or diarrhea. For example, oxaliplatin causes diarrhea in over 20% of patients and constipation in over 60% of patients, as reported during clinical trials^{37,38}. Importantly, 49% of patients report continuing symptoms post-treatment, suggesting damage to a non-regenerative tissue, such as neurons²⁷. This hypothesis has been supported by recent reports of platin-induced damage to the ENS in mice, including increases in mitochondrial stress, reactive oxygen species levels, and disrupted mitochondrial membrane integrity which coincide with a decrease in the total number of enteric neurons^{8-11,28,42}. These studies also report no significant damage to the muscle or mucosal tissue along the GI tract, which aligns with the low incidence of mucositis reported in humans³⁶⁻³⁸. Furthermore, there is evidence that platin-induced enteric neuropathy may be cell type-specific. For example, platins affect the proportion of enteric neuron subtypes in the ENS and the functional properties of nitrergic neurons, which are inhibitory enteric neurons^{8-10,31,42}. Notably, nitrergic neuron-mediated electrophysiological properties and motility phenotypes are disrupted following oxaliplatin treatment, indicating that inhibitory motor neuron functions may be specifically affected by platins⁹. Ultimately, platins cause colonic motility to

become increasingly ineffective in mice, manifesting in the clinically relevant phenotype of constipation⁸⁻¹¹.

These studies have solidified the link between the clinical manifestations of platin-induced GI dysmotility and cellular phenotypes of enteric neuropathy. Unfortunately, despite having a robust mouse model, the molecular pathways underlying the toxicity mechanism remain unidentified and no druggable targets have been nominated. Furthermore, it remains unclear why certain enteric neurons may be affected more than others. This is largely because of the technical challenges and translational limitations of studying platin-induced enteric neuropathy in animals. For example, enteric neurons reside solely within the GI tract, where they make up about 1% of the tissue making them inaccessible and difficult to study at large scale². Furthermore, mouse models and primary tissue samples are not scalable and therefore incompatible with high throughput methodologies such as unbiased pharmacologic screening that enable the discovery of disease mechanisms and drug targets.

Here, we utilized our established method of deriving enteric neurons from hPSCs^{5,32,33} to build a robust *in vitro* model of platin-induced enteric neuropathy and uncover the mechanism of toxicity. Using this system, we determined the cellular and molecular hallmarks of platin-induced enteric neuropathy through comprehensive phenotypic and transcriptomic profiling. Leveraging this model, we performed a high throughput screen, defined the toxicity mechanism, and identified drug candidates and potential therapeutic targets. The results revealed the excitotoxicity signaling network responsible for cell type

specific susceptibility of nitrergic neurons to platins. Finally, we demonstrated that blocking this disease pathway using our drug candidate can prevent platin-induced enteric neuropathy in mice.

2.3 Results

2.3.1 Enteric neurons are directly susceptible to platin chemotherapies

Despite platin chemotherapy drugs being approved and in use for decades, their adverse effects on GI functions have only been documented in clinical trials. To evaluate the prevalence of these adverse effects in the real world, we leveraged electronic medical record data from the UCSF Research Data Browser to investigate the propensity of a patient to develop chemotherapy-induced constipation after undergoing oxaliplatin or carboplatin treatment. For both oxaliplatin and carboplatin, we followed a similar analysis workflow (Figure 2.1A). We identified and extracted patients diagnosed with colorectal cancer (for the oxaliplatin analysis) or ovarian cancer (for the carboplatin analysis). To limit confounding the data, in both analyses, we excluded all patients who were diagnosed with constipation prior to their cancer diagnosis. The resulting patients in the platin chemotherapy treated and untreated groups were then matched based on age, sex, and race/ethnicity for each analysis. This ultimately resulted in sample sizes of 215 patients with colorectal cancer (46 patients prescribed oxaliplatin, 169 patients not prescribed oxaliplatin) and 4087 patients with ovarian cancer (438 patients prescribed carboplatin, 3649 patients not prescribed carboplatin), which were used for our analysis (Tables 2.1

and 2.2). The patients were then subset into four groups based on whether they were diagnosed with constipation. Patients prescribed oxaliplatin are 3.4 times more likely to develop constipation compared to patients not prescribed oxaliplatin with a p-value of < 0.001 (Figure 2.1B and Table 2.3). Similarly, patients prescribed carboplatin are 8.2 times more likely to be diagnosed with constipation (compared to patients not prescribed carboplatin) with a p-value of < 0.001 (Figure 2.1B and Table 2.3). These data highlight the detrimental effect of this chemotherapy drug class on GI motility. Furthermore, in our analysis, 57% of patients prescribed oxaliplatin and 49% of patients prescribed carboplatin were diagnosed with constipation, which does coincide with percentages reported in some clinical trials^{36,37}. However, our calculations are much higher than the prevalence of constipation reported in the package inserts for oxaliplatin and carboplatin, 31% and 6%, respectively, highlighting potential inconsistencies between the reported drug adverse effects and the actual prevalence of the adverse effect in a large, more diverse, real world patient population.

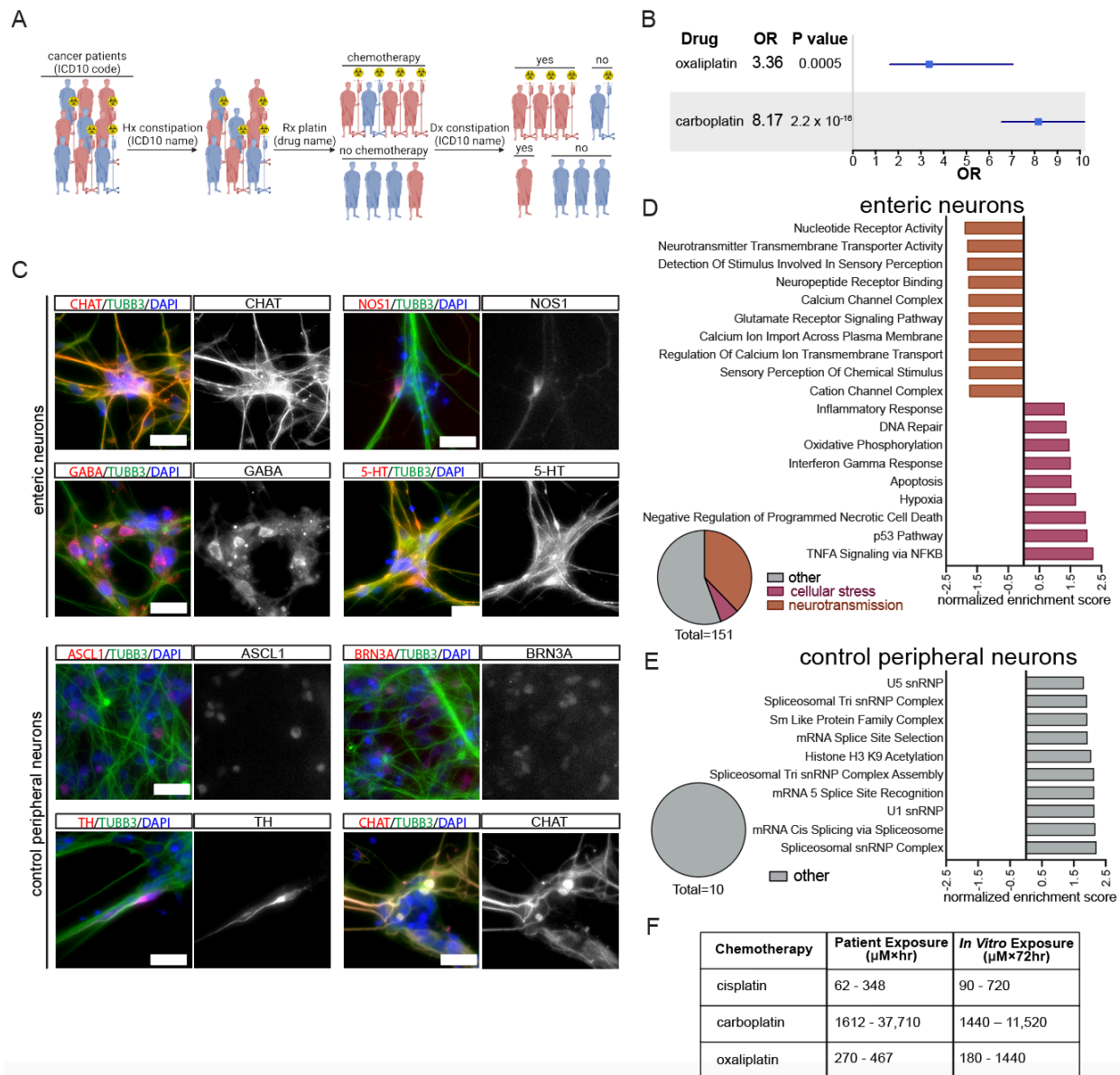


Figure 2.1 Evaluating platin-induced neurotoxicity in patient data and hPSC-derived enteric and control peripheral neurons

A) Schematic illustration of methods used to extract information from electronic medical records. Cancer patients were identified based on the relevant ICD10 codes. Patients with a prior history of constipation were removed based on a diagnosis of constipation (ICD10 name) prior to their cancer diagnosis. The patients were stratified depending on whether they were prescribed the relevant platin or not based on the drug name. Finally, the number of patients in each group that were diagnosed with constipation based on ICD10 name were quantified. The same analysis pipeline was used for both the oxaliplatin and carboplatin analyses.

B) Odds ratio (OR) and p-values comparing the prevalence of constipation in patients that received platin chemotherapy to patients that did not.

C) Representative images of enteric (CHAT, NOS1, GABA, 5-HT), sensory (BRN3A), sympathetic (ASCL1, TH), and parasympathetic (CHAT) markers in hPSC-derived enteric and control peripheral neurons. Scale bar: 50 μm .

D) Summary of gene sets significantly enriched in the \log_2 fold-change gene expression list comparing 50 μM oxaliplatin-treated enteric neurons to vehicle (medium containing 5% water)-treated enteric neurons. The bar graph highlights the top neurotransmission and cellular stress related pathways, and the pie chart shows the proportion of significantly enriched gene sets relating to neurotransmission or cellular stress.

E) Summary of gene sets significantly enriched in the \log_2 fold-change gene expression list comparing 50 μM oxaliplatin-treated control peripheral neurons to vehicle (medium containing 5% water)-treated control peripheral neurons. The bar graph highlights the gene sets significantly enriched in the gene list.

F) Table including calculated platin patient exposures and hPSC-derived enteric neuron exposures. Patient exposures were calculated based on each drug's reported clearance and a 1.79 m^2 patient body surface area for each indication the drugs are approved for. *In vitro* exposures were calculated by multiplying the drug treatment concentrations by the duration of the experiment (72 hours).

Animal studies have established the role of ENS damage in platin-induced GI dysmotility⁸⁻¹¹, but it remains unclear if this toxicity is due to a potentially higher exposure of the ENS tissue during drug delivery or an inherent susceptibility of enteric neurons to platins. We sought to address this possibility by exposing different peripheral neurons to identical platin treatment conditions and compare their response. Due to the limitations associated with isolation and maintenance of human neurons from primary tissue, we used our previously established hPSC differentiation system to generate human enteric neurons^{5,32,33}. Following approximately 40 days of differentiation, these hPSC-derived enteric neurons express a diverse array of neurotransmitter subtype markers, indicative of their successful recapitulation of the human ENS (Figure 2.1C). Similarly, we utilized an established protocol for generating cranial neural crest-derived peripheral neuron lineages from hPSCs⁴³. Following approximately 40 days of differentiation, this protocol can successfully generate a mixture of ASCL1+ and TH+ sympathetic neurons, BRN3A+ sensory neurons, and CHAT+ parasympathetic neurons, making it an ideal peripheral neuron control group to compare with enteric neurons (Figure 2.1C).

Leveraging these *in vitro* models, we aimed to characterize the direct effects platins have on enteric neurons as compared to control peripheral neurons (Figure 2.2A). Platin-induced cytotoxicity was measured in both neuronal populations by measuring the activity of lactate dehydrogenase released by dead cells in the cell culture supernatant. For each platin, the three day treatment resulted in the enteric neuron population having a significantly higher cytotoxicity response relative to the peripheral neuron control group, suggesting that enteric neurons are more vulnerable to platin toxicity relative to other peripheral neurons (Figure 2.2B). No differences in cytotoxicity were observed when the two neuron populations were treated with the mitochondrial toxin carbonyl cyanide m-chlorophenyl hydrazone (CCCP), indicating that the differential sensitivity to platins is not due to a higher general susceptibility to cellular stress.

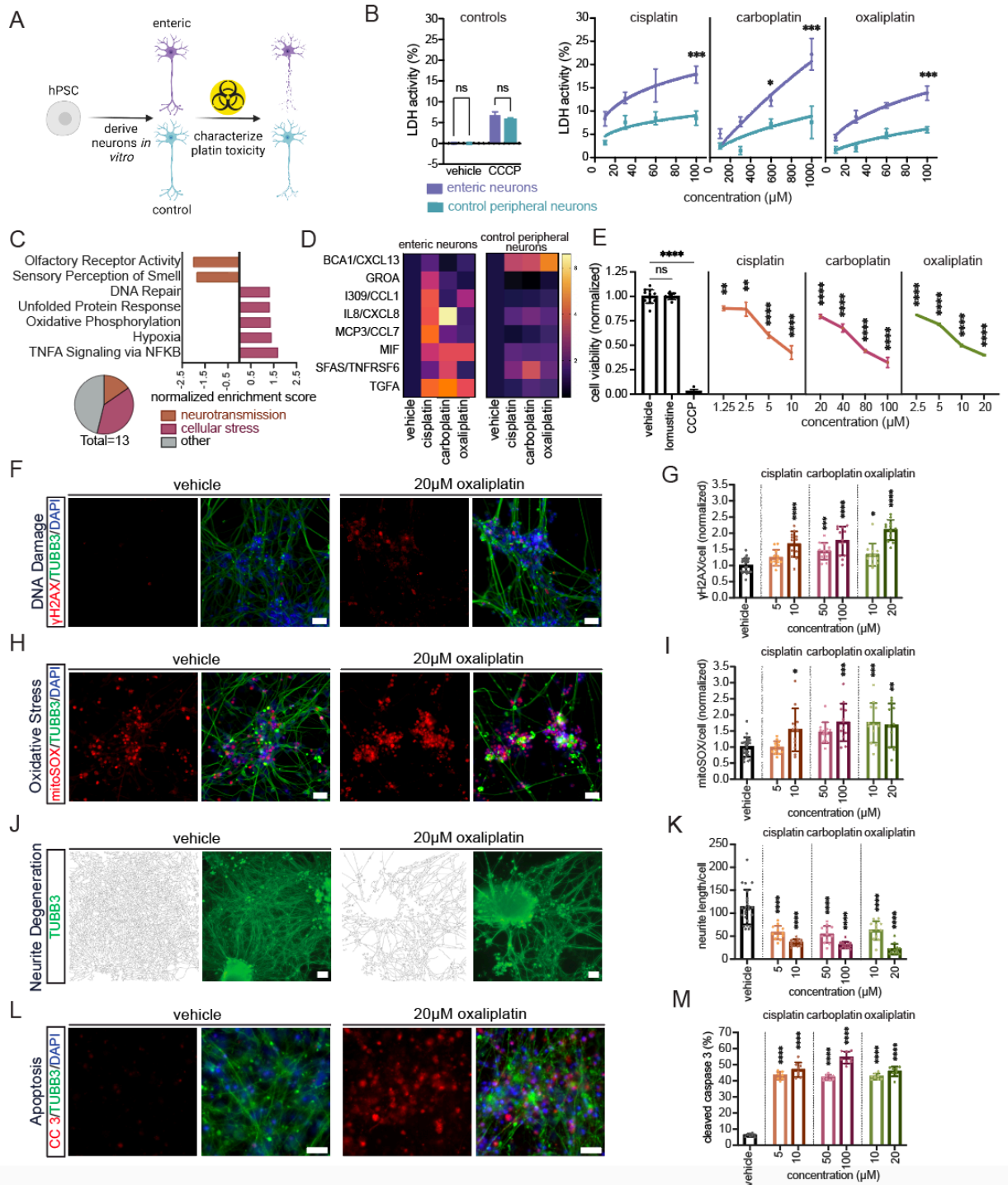


Figure 2.2 Enteric neurons are selectively vulnerable to platin chemotherapies

A) Schematic illustration of *in vitro* characterization of platin toxicity in enteric and control peripheral neurons.

B) Lactate dehydrogenase cytotoxicity analysis comparing the response of hPSC-derived enteric neurons to hPSC-derived control peripheral neurons treated with vehicle (medium containing 10%

water), 100 μ M CCCP, and increasing platin concentrations. All values are normalized by subtracting the vehicle condition from each sample. Data are represented as mean \pm SEM.

C) Summary of gene sets significantly enriched in the \log_2 fold-change gene expression list comparing 50 μ M oxaliplatin-treated enteric neurons to 50 μ M oxaliplatin-treated control peripheral neurons. The bar graph highlights neurotransmission and cellular stress related pathways and the pie chart shows the proportion of significantly enriched gene sets relating to neurotransmission or cellular stress.

D) Heatmap of the cytokines significantly increased in the cell culture supernatant of enteric and control peripheral neurons treated with 20 μ M cisplatin, 200 μ M carboplatin, 40 μ M oxaliplatin, or medium containing 4% water (vehicle). Each cytokine is normalized to its vehicle cytokine levels.

E) Cell viability analysis of hPSC-derived enteric neurons exposed to vehicle (medium containing 2% water), 20 μ M lomustine, 10 μ M CCCP, and increasing platin concentrations. All values are normalized to vehicle. Data are represented as mean \pm SEM.

F, G) γ H2AX staining and quantification in platin-treated hPSC-derived enteric neurons. All values are normalized to vehicle (medium containing 2% water). Scale bar: 50 μ m. Data are represented as mean \pm SD.

H, I) mitoSOX staining and quantification in platin-treated hPSC-derived enteric neurons. All values are normalized to vehicle (medium containing 2% water). Scale bar: 50 μ m. Data are represented as mean \pm SD.

J, K) TUBB3 staining, TUBB3 neurite traces, and quantification in platin-treated hPSC-derived enteric neurons. Vehicle condition contains water diluted to 2% in medium. Scale bar: 50 μ m. Data are represented as mean \pm SD.

L, M) Cleaved caspase 3 staining and quantification in platin-treated hPSC-derived enteric neurons. Vehicle condition contains water diluted to 2% in medium. Scale bar: 50 μ m. Data are represented as mean \pm SD.

* p value < 0.05, ** p value < 0.01, *** p value < 0.001, **** p value < 0.0001, ns: not significant.

To further characterize this cell-type specific response to platins, we performed bulk transcriptomic profiling of the enteric neuron and the control peripheral neuron populations. Read counts of oxaliplatin treated enteric neurons were compared to the oxaliplatin treated control peripheral neurons to calculate the \log_2 fold-change in gene expression. Then pre-ranked gene set enrichment analysis (GSEA) was performed to identify gene sets significantly changed between the two populations based on a p-value cutoff of < 0.05 and a false discovery rate of < 0.25. Multiple gene sets related to cellular stress were positively enriched in the enteric neurons relative to the control peripheral neurons, further suggesting enteric neurons have an increased susceptibility to platin toxicity (Figure 2.2C). These cellular stress gene sets included oxidative phosphorylation, which may reflect the phenotype of increased oxaliplatin-induced mitochondrial oxidative

stress observed *in vivo*^{8,9}. The DNA repair pathway likely reflects the cellular response to oxaliplatin's mechanism of action, DNA damage²⁶. Other cellular stress pathways such as unfolded protein response, hypoxia, and TNF signaling via NF- κ B have never been characterized in the context of platin-induced enteric neuropathy and may reflect other neurotoxic pathways activated during drug exposure. Additionally, two neurotransmission related pathways were negatively enriched in the enteric neurons relative to the control peripheral neurons: olfactory receptor activity and sensory perception of smell. This suggests that platins may impact neuronal signaling in enteric neurons more than other peripheral neurons and this may be another contributing factor to platin-induced enteric neuropathy.

To identify biological pathways transcriptionally dysregulated by platins in hPSC-derived enteric neurons, we performed pre-ranked GSEA on the \log_2 fold-change in gene expression between oxaliplatin treated enteric neurons and vehicle treated enteric neurons. Many gene sets related to neuronal signaling pathways were significantly negatively enriched, indicating that aberrant neurotransmission may be a key pathway underlying platin-induced enteric neuropathy (Figure 2.1D). Furthermore, many cellular stress gene sets reflecting neuroinflammatory, oxidative stress, and DNA damage pathways were again revealed in this analysis (Figure 2.1D). As a control, we also performed this analysis on the \log_2 fold-change in gene expression between oxaliplatin treated control peripheral neurons and vehicle treated control peripheral neurons. None of the significantly enriched gene sets reflect neurotransmission or cellular stress related pathways, again suggesting that they are less susceptible to platin toxicity (Figure 2.1E).

The significant enrichment of TNF signaling via NF- κ B in enteric neurons relative to other peripheral neurons indicates that neuroinflammation may have a role in potentiating platin-induced enteric neuropathy. NF- κ B is a master regulator of neuroinflammation that ultimately can lead to the release of cytokines and chemokines from the cell to activate the appropriate immune cells to clear the inflammation and tissue damage⁴⁴. To experimentally test if platin-induced neuroinflammation is increased in enteric neurons relative to other peripheral neurons, we performed a cytokine array detecting the levels of 76 neuroinflammatory cytokines in each cell population's culture supernatant after three days exposure to the platins (Table 2.4). The median fluorescence intensities for each cytokine were averaged and normalized to each population's vehicle treatment condition. Enteric neurons significantly increased the release of seven inflammatory cytokines in response to at least one platin, including C-X-C motif chemokine ligand 1 (GROA), chemokine C-C motif ligand 1 (I309/CCL1), interleukin-8 (IL8/CXCL8), chemokine C-C motif ligand 7 (MCP3/CCL7), macrophage migration inhibitory factor (MIF), tumor necrosis factor receptor superfamily member 6 (SFAS/TNFRSF6), and transforming growth factor alpha (TGFA), whereas the control peripheral neuron population, on the other hand, only had two cytokines that were significantly increased: chemokine C-X-C motif ligand 13 (BCA1/CXCL13) and SFAS/TNFRSF6 (Figure 2.2D). These results confirm the transcriptomic-based prediction of enteric neurons experiencing an increased neuroinflammatory response to platins relative to other peripheral neurons (Figure 2.2C). Furthermore, SFAS/TNFRSF6 is the only cytokine significantly increased in both populations (Figure 2.2D). This indicates that the enteric

neuron inflammatory response to platins is largely non-overlapping with other peripheral neurons and reflects a cell-type specific drug response. This highlights the importance of using a model system that best reflects the distinct molecular state of the relevant cell type.

The evidence that enteric neurons are significantly more sensitive to platin chemotherapies as compared to other divisions of the PNS prompted us to systematically evaluate the neurotoxic phenotypes platin chemotherapies directly induce in hPSC-derived enteric neurons. To better characterize the effect of platins on enteric neuron viability, we treated enteric neurons with a range of platin chemotherapy concentrations for three days. We observed dose-dependent decreases in cell viability, measured via ATP levels, with LC₅₀ values of 4.7 μ M, 69.3 μ M, and 7.1 μ M and for cisplatin, carboplatin, and oxaliplatin, respectively (Figure 2.2E). To determine if this reduction in enteric neuron viability is a platin-specific mechanism or not, we also exposed enteric neurons to lomustine, a chemotherapy drug with a similar mechanism of action to platins, but with low incidence of GI toxicity reported clinically⁴⁵. We observed no significant effects on enteric neuron viability when hPSC-derived enteric neurons were treated with lomustine for three days (Figure 2.2E). This data suggests that the enteric neurons are directly sensitive to platin chemotherapies via a platin chemotherapy-specific toxicity mechanism.

To validate that these *in vitro* treatment conditions reflect exposures a patient might experience clinically, we calculated patient exposure by dividing the recommended patient dose by each platin's clearance. Performing this calculation for each indication the

platin is approved for, we generated a range of expected patient exposures for each platin chemotherapy (Figure 2.1F). *In vitro* exposures were calculated by multiplying the concentrations used *in vitro* by the duration of the experiment – 72 hours. These *in vitro* exposures overlap with the patient exposures, further indicating that the *in vitro* experiments reflect biologically and clinically relevant conditions (Figure 2.1F).

To experimentally validate the oxaliplatin-induced cellular stress response predicted from our transcriptomic profiling, we performed relevant phenotypic assays in our hPSC-derived enteric neuron cultures. Significant positive enrichment of the DNA repair and p53 pathway gene sets suggests platins directly induce DNA damage in enteric neurons (Figure 2.2C and 2.1D). To measure levels of DNA damage, we performed immunostaining to detect γ H2AX, a histone post-translational modification that occurs when a DNA double strand break is detected⁴⁶. All three platins significantly increased γ H2AX levels in hPSC-derived enteric neurons, confirming that platins indeed cause DNA damage in enteric neurons (Figure 2.2F-G). Positive enrichment of the oxidative phosphorylation and mitochondrial large ribosomal subunit gene sets suggests platins may directly induce mitochondrial oxidative stress in enteric neurons (Figure 2.2C and 2.1D). Increased mitochondrial reactive oxygen species and mitochondrial membrane permeability has been observed in mouse models of oxaliplatin-induced enteric neuropathy^{8,9}. However, in these studies it remained unclear if this phenotype was due to direct or indirect effects of platins on enteric neurons or changes in the vascular tissue that supply oxygen to the ENS tissue. Our transcriptomic profiling on hPSC-derived enteric neurons *in vitro* suggests that this toxicity hallmark is conserved in human cells

and is due to a direct effect of platins on enteric neurons. To test this hypothesis, we utilized the mitochondrial superoxide indicator, mitoSOX, to detect oxidative stress in platin-treated enteric neurons. Indeed, mitochondrial superoxide levels were significantly increased following platin exposure in hPSC-derived enteric neurons, confirming the results of our transcriptomic profiling and supporting the role of increased reactive oxygen species in potentiating platin-induced enteric neuropathy (Figure 2.2H-I). Given that neurodegeneration is a common hallmark of neuropathy and has been observed in other forms of chemotherapy-induced neurotoxicity²²⁻²⁴, we aimed to identify if platins induce neurodegeneration in enteric neurons. We characterized platin-induced neurodegeneration by quantifying the total neurite length per cell, measured by tubulin beta 3 class III (TUBB3) immunostaining and DAPI staining, respectively. Through this method, we observed that each platin indeed reduces the neurite networks in hPSC-derived enteric neurons, indicating that platins cause enteric neurons to degenerate (Figure 2.2J-K). Lastly, the positive enrichment of the apoptosis and p53 pathway gene sets suggests platins induce enteric neuron cell death via apoptosis (Figure 2.1D). To measure apoptosis induction, we detected levels of cleaved caspase 3, a post-translational modification that occurs to initiate apoptosis⁴⁷. At each concentration tested, all three platins significantly increased the percentage of neurons positive for cleaved caspase 3, indicating the initiation of apoptosis (Figure 2.2L-M). Thus, platins directly induce DNA damage and oxidative stress in hPSC-derived enteric neurons, leading to neurite degeneration and programmed cell death.

Altogether, these data indicate that enteric neurons are directly sensitive to platin chemotherapies and suggests that platin-induced enteric neuropathy may be largely explained by the direct interaction between platins and enteric neurons, as all phenotypes were induced *in vitro*, in the absence of the *in vivo* tissue micro and macro environments. Therefore, methods that block the direct effect of platins on enteric neurons may be highly effective at preserving this vulnerable cell type.

2.3.2 Phenotypic screen identifies platin-induced excitotoxicity mechanism

Leveraging our scalable model of platin-induced enteric neuropathy, we carried out a high throughput phenotypic drug screen followed by drug target enrichment analysis to uncover the molecular mechanism underlying platin-induced enteric neuropathy (Figure 2.3A). Searching for modulators of oxaliplatin-induced cell death, we screened the Selleckchem small molecule library of 1,443 FDA-approved drugs in both induced pluripotent stem cell (iPSC) and embryonic stem cell (ESC)-derived enteric neurons (Figure 2.3B). Cell viability was quantified by detecting dead cells via DAPI staining prior to fixation and all cells via propidium iodide staining post fixation. From the screen, we confirmed the effect of three compounds with high positive cell viability z-scores (mefloquine, mitotane, and oxybutynin). All were able to significantly reduce oxaliplatin-induced cell death, measured via ATP levels as an orthogonal cell viability detection method, suggesting they can block the toxicity mechanism and increase cell viability when dosed in combination with oxaliplatin (Figure 2.3C).

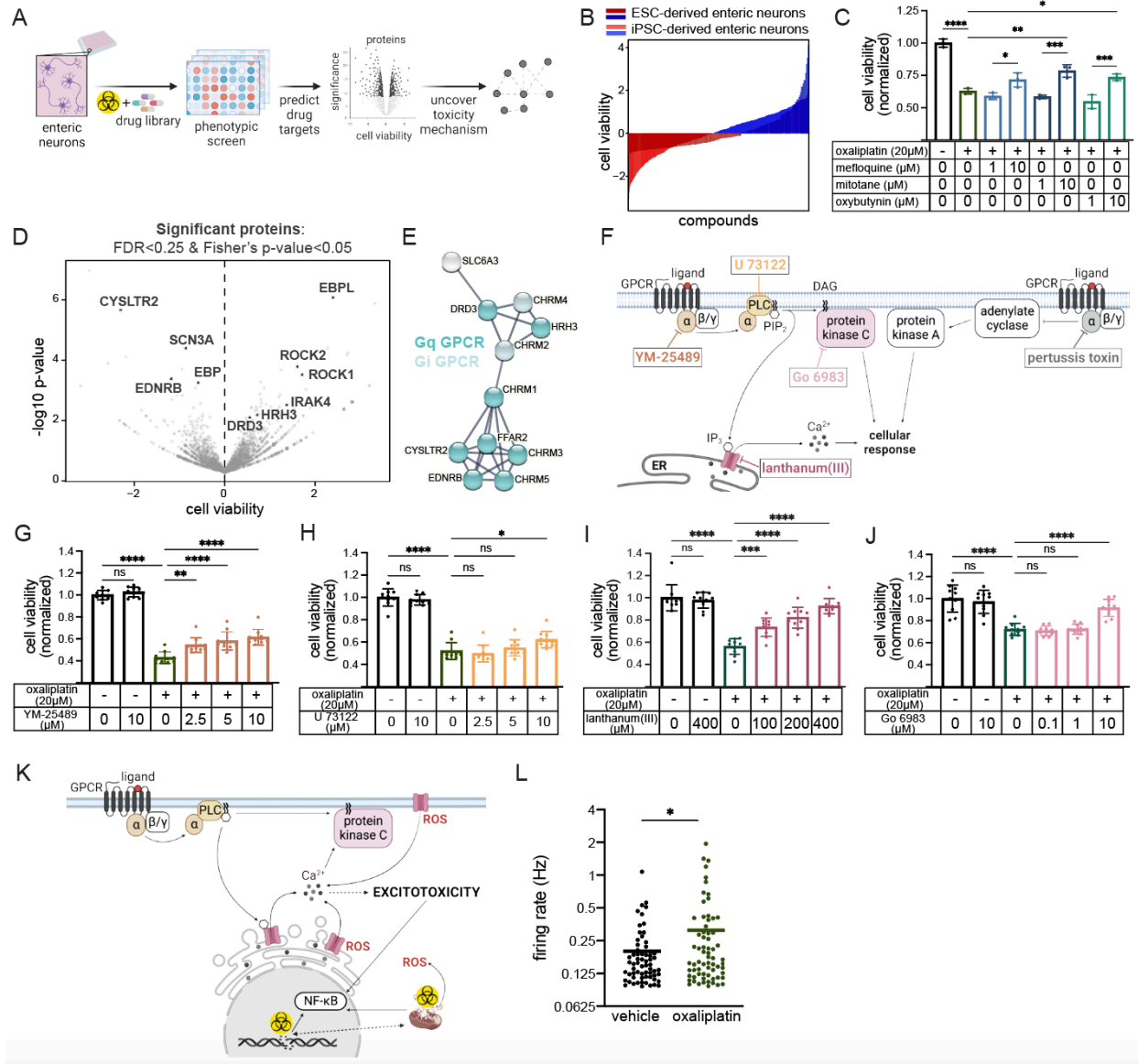


Figure 2.3 High throughput screen uncovers mechanism of platin-induced excitotoxicity in enteric neurons

A) Schematic illustration of our drug and drug target discovery pipeline. High throughput screening followed by SEA-STRING analysis identifies drugs and drug targets that affect hPSC-derived enteric neuron viability during oxaliplatin treatment.

B) High throughput screening of Selleckchem FDA approved drug library identifies drugs that increase and decrease hPSC-derived enteric neuron viability during oxaliplatin treatment.

C) Dose response of the hit compounds on hPSC-derived enteric neuron viability when dosed in combination with oxaliplatin. All values are normalized to vehicle (medium containing 2% water). Data are represented as mean \pm SD.

D) Volcano plot showing the average cell viability z-score versus the $-\log_{10}$ p-value of the genes targeted in the screen. The genes that pass our statistical thresholds are marked in black (combined z-score FDR < 0.25 and Fisher's p-value < 0.05).

E) STRING protein-protein interaction network formed from our gene list of predicted drug targets. Network is primarily composed of GPCRs with proteins of the G_q class shown in dark cyan and

proteins of the G_i class shown in light cyan. The minimum required interaction score was set to 0.7, reflecting high confidence interactions.

F) Schematic illustration of our strategy to use tool compounds to interrogate the role of the G_q-mediated inositol phospholipid signaling pathway and the G_i-mediated cyclic adenosine monophosphate dependent pathway in potentiating platin-induced enteric neuropathy.

G-J) Dose response of the tool compounds on hPSC-derived enteric neuron viability when dosed in combination with oxaliplatin. All values are normalized to vehicle (medium containing 2% water). (**G**) YM-25489 a G_q inhibitor, (**H**) U 73122, a phospholipase C inhibitor, (**I**) lanthanum (III), a calcium channel blocker potent at IP3 receptors, (**J**) Go 6983, a protein kinase C inhibitor. Data are represented as mean ± SD.

K) Schematic illustration of our platin-induced excitotoxicity mechanism.

L) Quantification of microelectrode array analysis of 10 μM oxaliplatin and vehicle (medium containing 1% water)-treated hPSC-derived enteric neurons. Data are represented as mean.

* p value < 0.05, ** p value < 0.01, *** p value < 0.001, **** p value < 0.0001, ns: not significant.

To evaluate the clinical relevance of these compounds as therapies to protect enteric neurons during chemotherapy treatment, we evaluated them in two colorectal cancer cell lines (SW480 and WiDr), assessing whether any of them alter the antineoplastic efficacy of platin chemotherapies. In both colorectal cancer lines, mefloquine increased cell death when dosed in combination with the platins (Figure 2.4A, 2.4B, 2.4C). This result either suggests that mefloquine has antineoplastic activity itself or that it is generally toxic at the concentrations tested. Mitotane, on the other hand, consistently decreased cancer cell death when dosed in combination with the platins, suggesting that it likely protects enteric neurons by blocking the antineoplastic mechanism of the platins and therefore is an undesirable therapeutic candidate to counteract enteric neurotoxicity in cancer patients (Figure 2.4A, 2.4B, 2.4C). Oxybutynin exhibited no effect on the antineoplastic efficacy of any of the platins in either of the colorectal cancer cell lines, except for one exception. Oxybutynin did significantly decrease cell death when dosed at 4 μM in the WiDr line in combination with oxaliplatin, but this result was not replicated at the 1, 7 or 10 μM concentrations, so was likely driven by outliers (Figure 2.4C). Given that oxybutynin protects enteric neurons from platin-induced cell death without affecting cancer killing, its

protective mechanism is likely DNA damage independent and reflects a parallel mechanism capable of preserving enteric neurons. Thus, oxybutynin is the compound from the drug screen that is most likely to be compatible with clinical dosing in cancer patients for preventing platin-induced GI neurotoxicity.

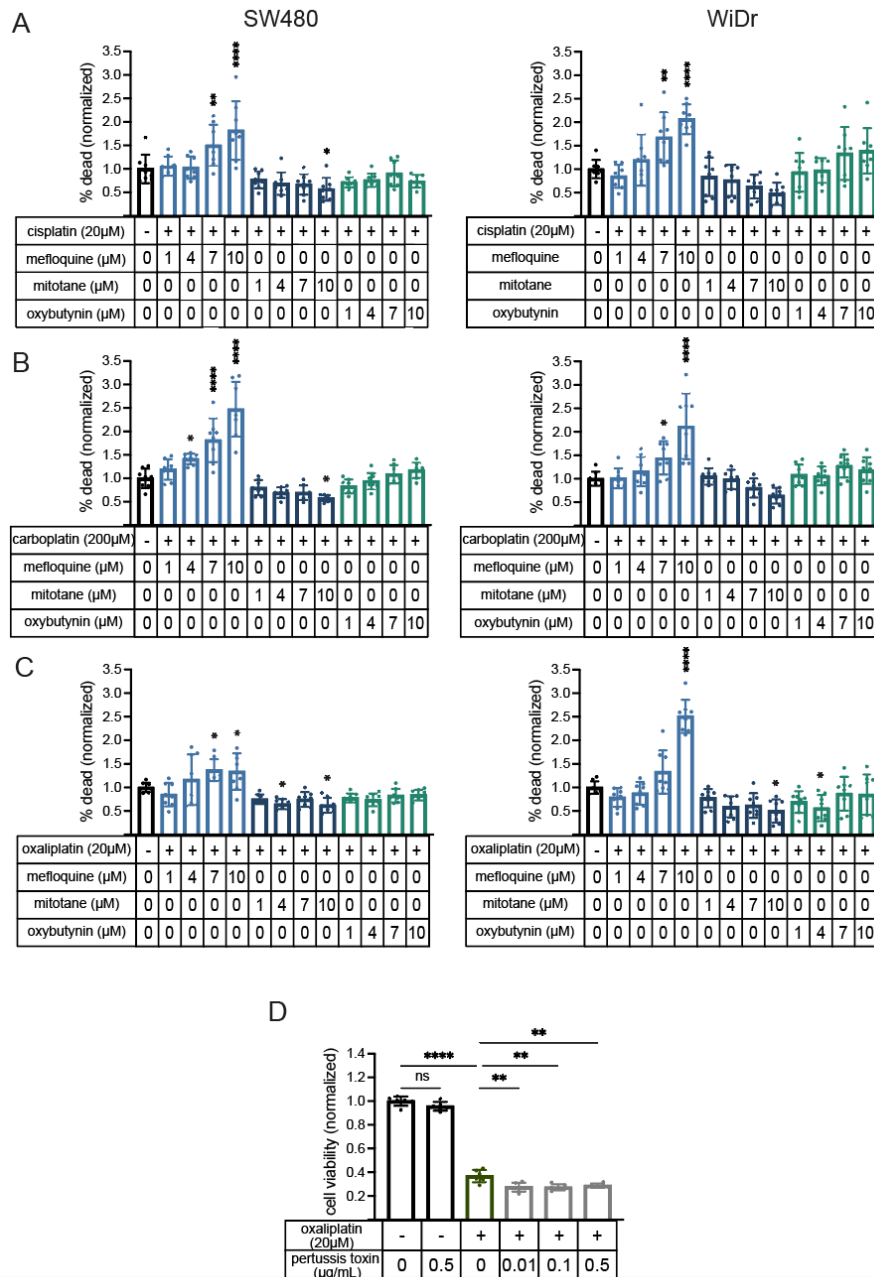


Figure 2.4 Effect of drug screen hits on platin antineoplastic efficacy and G_i protein inhibitor on platin-induced enteric neuropathy

A-C) Dose response of the hit compounds on SW480 (left) and WiDr (right) colorectal cancer cell viability when dosed in combination with platins. All values are normalized to the platin being tested. **(A)** 20 μM cisplatin, **(B)** 200 μM carboplatin, **(C)** 20 μM oxaliplatin. Data are represented as mean ± SD.

D) Dose response of pertussis toxin, a G_i inhibitor, on hPSC-derived enteric neuron viability when dosed in combination with oxaliplatin. All values are normalized to vehicle (medium containing 2% water). Data are represented as mean ± SD.

* p value < 0.05, ** p value < 0.01, *** p value < 0.001, **** p value < 0.0001, ns: not significant.

To identify the proteins that modulate oxaliplatin-induced enteric neuron viability, we utilized our previously published drug-protein interaction analysis pipeline to predict drug targets enriched in the compounds that either increase or decrease oxaliplatin-treated enteric neuron viability in both of our drug screen datasets⁶. Via this method, we identified 10 likely target proteins that met the significance criteria of a false discovery rate < 0.25 based on the combined z-score analysis and a Fisher's p-value < 0.05 (Figure 2.3D and Table 2.5). In addition to this unbiased approach, we also predicted the drug-protein interactions of our three validated drugs (mefloquine, mitotane, and oxybutynin), by inputting their simplified molecular-input line-entry system (SMILES) into the similarity ensemble approach (SEA) computational tool⁴⁸. We filtered out the significant drug-protein interactions by selecting human proteins and predicted interaction p-values < 0.05 , yielding 11 proteins predicted to be targeted by the validated hits (Table 2.6). Through these unbiased and biased prediction methods, we identified a total of 21 potential targets.

To explore if the drug target proteins are part of shared pathway, we conducted a protein-protein interaction network analysis using the STRING physical interaction database⁴⁹ to uncover a network of proteins with a high confidence interaction score. This approach revealed a core network of G protein-coupled receptors (GPCRs) of the G_q class shown in dark cyan and GPCRs of the G_i class shown in light cyan in Figure 2.3E, suggesting that GPCR signaling may potentiate platin toxicity in enteric neurons.

The convergence of the GPCR protein-protein interaction network with the neurotransmission pre-ranked GSEA results, led us to hypothesize that platin-induced enteric neuropathy may be reduced by antagonizing neurotransmitter-mediated GPCR signaling. To test this hypothesis, we employed five chemical tools that either inhibit or antagonize proteins along the G_q -mediated inositol phospholipid signaling pathway and the G_i -mediated cyclic adenosine monophosphate dependent pathway and evaluated their effects on oxaliplatin-induced cell viability (Figure 2.3F). To interrogate the role of the G_q protein alpha subunit, we utilized YM-25489, a G_q inhibitor, which when dosed in combination with oxaliplatin at 2.5, 5, and 10 μM was able to significantly increase cell viability, implicating the G_q -mediated inositol phospholipid signaling pathway in platin toxicity in enteric neurons (Figure 2.3G). To interrogate the role of the G_i protein alpha subunit, we utilized pertussis toxin, a G_i inhibitor, which when dosed up to 0.5 $\mu\text{g/mL}$ in combination with oxaliplatin was unable to significantly increase cell viability, suggesting the G_i -mediated cyclic adenosine monophosphate dependent pathway is not a key driver of the platin toxicity mechanism (Figure 2.4D). Thus, we hypothesized that G_q -mediated inositol phospholipid signaling is the primary contributor to the platin-induced enteric neuropathy mechanism and tested this hypothesis by inhibiting or antagonizing downstream effectors of the G_q protein. U 73122, a phospholipase C (PLC) inhibitor, was able to significantly increase enteric neuron viability when dosed at 10 μM in combination with oxaliplatin, indicating that PLC activated by G_q proteins is involved in the toxicity mechanism (Figure 2.3H). Active PLCs cleave phosphatidylinositol bisphosphate (PIP₂), increasing inositol triphosphate (IP₃) concentrations in the cytosol, which can bind and open IP₃ calcium channels in the endoplasmic reticulum⁵⁰. To explore the role of IP₃

receptors in platin-induced enteric neuropathy, we utilized lanthanum (III), a calcium channel blocker potent at IP3 receptors, which also was able to significantly increase cell viability when dosed at 100, 200 and 400 μM in oxaliplatin-treated enteric neurons, suggesting that calcium is an important second messenger in the toxicity mechanism (Figure 2.3I). Lastly, when cleaving PIP2, PLCs also increase membrane-bound diacylglycerol (DAG) levels, which can activate protein kinase C (PKC) signaling⁵⁰. To evaluate the role of PKC signaling in the platin-induced enteric neuropathy mechanism, we utilized Go 6983, a PKC inhibitor, which also protected enteric neuron cell viability when dosed in combination with oxaliplatin at 10 μM (Figure 2.3J). Together, these data suggest that platin-induced enteric neuropathy is potentiated by aberrant G_q -mediated signaling.

Combining our identified hallmarks of platin-induced enteric neuropathy with the components of the inositol phospholipid signaling pathway, we formulated a potential mechanism of enteric neuron excitotoxicity triggered by platin-induced cellular stress (Figure 2.3K). The mechanism begins with platin-induced DNA damage and increased reactive oxygen species, which we observed *in vitro* and others have observed *in vivo* (Figure 2.2G-J)^{8,9}. Reactive oxygen species can interact with calcium channels of the endoplasmic reticulum and extracellular membrane, permitting the depolarization of the cell, which, in neurons, leads to action potentials⁵¹. For enteric neurons with GPCRs of the G_q class, the G_q -mediated inositol phospholipid signaling pathway leads to further depolarization of the cell, causing these neurons to enter an excitotoxicity positive

feedback loop, which can lead to aberrant PKC activity and increased NF- κ B-mediated neuroinflammatory activity.

To evaluate this hypothesis, we determined if platins increase the electrical activity of enteric neurons by performing a microelectrode array experiment measuring the mean firing rate in oxaliplatin-treated cultures. After a three hour incubation, oxaliplatin significantly increased the firing rate in treated neurons, as compared to vehicle-treated controls, suggesting enteric neurons indeed become hyperexcitable following oxaliplatin exposure (Figure 2.3L). Altogether, these data support our hypothesis that platin-induced enteric neuropathy is driven by calcium-mediated excitotoxicity.

2.3.3 Muscarinic cholinergic signaling promotes platin-induced enteric neurotoxicity

Oxybutynin, one of the protective and most clinically relevant compounds from our drug screen (Figure 2.3C, 2.4A-C) is a potent muscarinic cholinergic receptor antagonist commonly prescribed for overactive bladder⁵². Acetylcholine is a key neurotransmitter in the ENS, mediating the activity of intrinsic circuits important for proper GI motility³⁰. Notably, oxybutynin can decrease GI motility in humans, suggesting that its anticholinergic activity affects the ENS⁵². Three out of the five muscarinic cholinergic receptors are GPCRs of the G_q class, muscarinic cholinergic receptor 1 (CHRM1), muscarinic cholinergic receptor 3 (CHRM3), and muscarinic cholinergic receptor 5 (CHRM5), which led us to hypothesize that oxybutynin prevents platin-induced

excitotoxicity by antagonizing G_q muscarinic cholinergic receptors. To test this hypothesis, we used both pharmacologic and genetic tools to determine oxybutynin's therapeutic target and characterize its ability to prevent platin-induced excitotoxicity (Figure 2.5A).

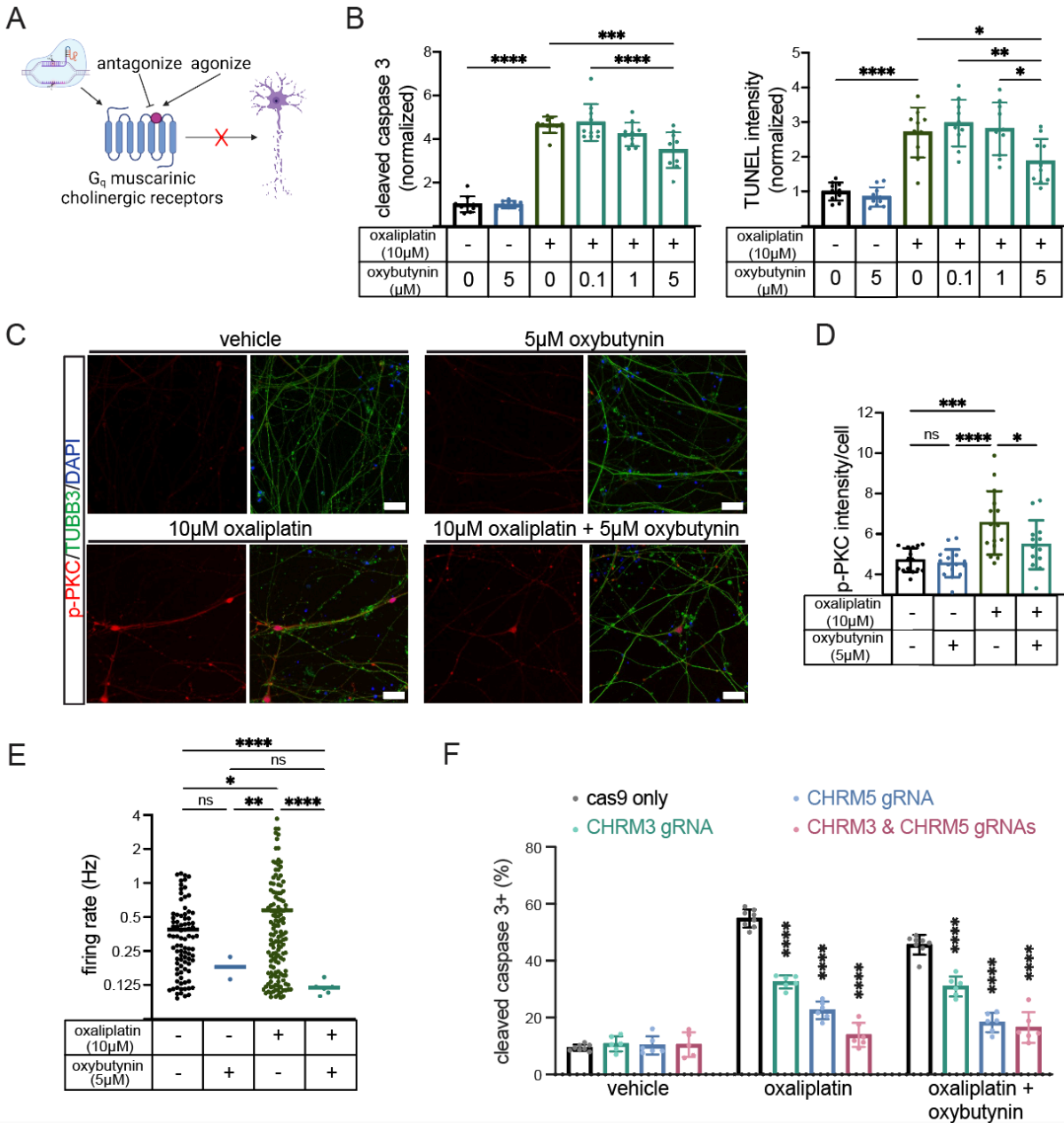


Figure 2.5 Reducing muscarinic cholinergic receptor signaling prevents platin-induced excitotoxicity in enteric neurons

A) Schematic illustration of our strategy to use tool compounds and CRISPR-cas9 technology to interrogate the role of muscarinic cholinergic receptor signaling in platin-induced enteric neuropathy.

B) Quantification of image based analysis detecting the dose response of the oxybutynin on hPSC-derived enteric neuron cleaved caspase 3 (left) and TUNEL (right) levels when dosed in combination with oxaliplatin. All values are normalized to vehicle (medium containing 1% water).

C, D) Phosphorylated protein kinase C (p-PKC) staining and quantification in oxybutynin and oxaliplatin-treated hPSC-derived enteric neurons. Vehicle condition contains water diluted to 1% in medium.

E) Quantification of microelectrode array analysis of oxybutynin and oxaliplatin-treated hPSC-derived enteric neurons. Vehicle condition contains water diluted to 1% in medium.

F) Quantification of flow cytometry analysis detecting cleaved caspase 3 levels during oxybutynin and oxaliplatin treatment in *CHRM3* and *CHRM5* CRISPR-cas9 RNP targeted hPSC-derived enteric neurons. Vehicle condition contains water diluted to 1% in medium.

* p value < 0.05, ** p value < 0.01, *** p value < 0.001, **** p value < 0.0001, ns: not significant.

To further evaluate the ability of oxybutynin to protect against platin-induced enteric neuropathy, we measured its effect on oxaliplatin-induced apoptosis. Treatment with oxaliplatin significantly increased the percentage of cells positive for cleaved caspase 3, and oxybutynin was able to significantly reduce this effect in a dose-dependent manner (Figure 2.5B). We also measured the level of DNA fragmentation, a hallmark of late stage apoptosis, by terminal deoxynucleotidyl transferase dUTP nick end labeling (TUNEL) assay, and detected a significant increase upon oxaliplatin treatment. Again, oxybutynin co-treatment was able to significantly reduce this effect in a dose-dependent manner (Figure 2.5B). Thus, oxybutynin is highly effective at preventing oxaliplatin-induced apoptosis in enteric neurons.

To determine if oxybutynin can prevent overactivity of the inositol phospholipid signaling pathway, we detected phosphorylated protein kinase C (p-PKC) levels as a hallmark of pathway activity. As expected, oxaliplatin significantly increased levels of p-PKC per cell, validating increased PKC activity as a hallmark of platin-induced excitotoxicity (Figure 2.5C-D, 2.6A). When the cells were co-treated with oxybutynin and oxaliplatin, however, p-PKC levels were significantly reduced (Figure 2.5C-D, 2.6A). This suggests that antagonizing cholinergic signaling in enteric neurons is sufficient to reduce G_q-mediated inositol phospholipid signaling pathway activity.

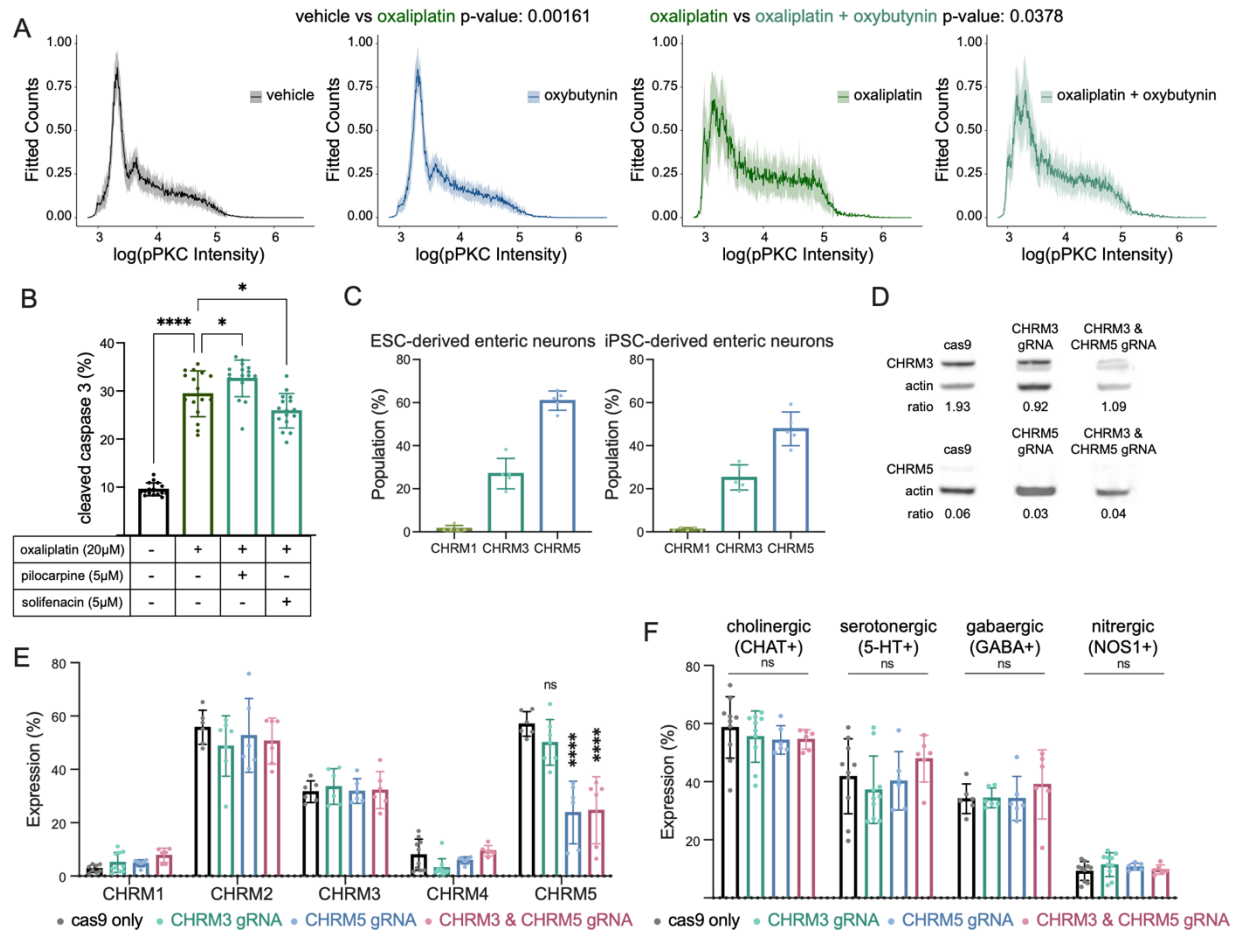


Figure 2.6 Effect of muscarinic antagonism on platin toxicity hallmarks and CHRM3 and CHRM5 CRISPR-cas9 targeted hPSC-derived enteric neuron characterization

A) Distribution of neuronal phosphorylated protein kinase C (pPKC) intensity per cell in 5 μ M oxybutynin and 10 μ M oxaliplatin-treated hPSC-derived enteric neurons. Vehicle contains water diluted to 1% in medium. Data are represented as mean \pm SD.

B) Quantification of flow cytometry analysis detecting cleaved caspase 3 levels in oxaliplatin-treated hPSC-derived enteric neurons co-treated with pilocarpine (muscarinic agonist) or solifenacin (muscarinic antagonist). Vehicle contains water diluted to 2% in medium. Data are represented as mean \pm SD.

C) Quantification of flow cytometry analysis detecting the expression of G_q muscarinic cholinergic receptors *CHRM1*, *CHRM3*, and *CHRM5* in ESC-derived and iPSC-derived enteric neurons. Data are represented as mean \pm SD.

D) Western blots and quantification of CHRM3 and CHRM5 protein levels in *CHRM3* and *CHRM5* CRISPR-cas9 RNP targeted hPSC-derived enteric neurons as compared to cas9 only targeted hPSC-derived enteric neurons.

E) Quantification of flow cytometry analysis detecting the expression of muscarinic cholinergic receptors *CHRM1*, *CHRM2*, *CHRM3*, *CHRM4*, and *CHRM5* in *CHRM3* and *CHRM5* CRISPR-cas9 RNP targeted hPSC-derived enteric neurons as compared to cas9 only targeted hPSC-derived enteric neurons. Data are represented as mean \pm SD.

F) Quantification of flow cytometry analysis detecting the levels of neurotransmitter markers CHAT, GABA, NOS1, and serotonin in *CHRM3* and *CHRM5* CRISPR-cas9 RNP targeted hPSC-

derived enteric neurons as compared to cas9 only targeted hPSC-derived enteric neurons. Data are represented as mean \pm SD.

* p value < 0.05, **** p value < 0.0001, ns: not significant.

To determine if oxybutynin can prevent platin-induced excitotoxicity, we performed a microelectrode array experiment measuring the mean firing rate of hPSC-derived enteric neurons treated with oxaliplatin with and without oxybutynin. After three hours of incubation, oxaliplatin significantly increased the electrical firing of enteric neurons as compared to vehicle-treated enteric neurons (Figure 2.5E). Oxybutynin co-treatment, however, completely blocked this oxaliplatin-induced hyperexcitability, suggesting platin-induced excitotoxicity can be prevented by oxybutynin.

To determine if oxybutynin's efficacy is mediated through muscarinic cholinergic antagonism and validate the role of muscarinic cholinergic signaling in platin-induced enteric neuropathy, we employed two structurally distinct compounds: pilocarpine, a muscarinic cholinergic receptor agonist, and solifenacin, a muscarinic cholinergic receptor antagonist. Dosing these compounds in combination with oxaliplatin produced opposite effects on oxaliplatin-induced apoptosis. Pilocarpine exacerbated toxicity, increasing the percentage of enteric neurons positive for cleaved caspase 3 by 3.2%, and solifenacin dampened toxicity, reducing the percentage of neurons positive for cleaved caspase 3 by 3.5% (Figure 2.6B). These results suggest that muscarinic cholinergic signaling potentiates platin-induced enteric neurotoxicity and oxybutynin's protective effect is mediated by antagonizing this pathway.

Oxybutynin is most potent at antagonizing CHRM3 but at physiologically relevant concentrations can block all five muscarinic receptors. CHRM1, CHRM3, and CHRM5 are GPCRs of the G_q class, thus all could be mediating the activation of the inositol phospholipid signaling pathway involved in the platin-induced excitotoxicity mechanism. To determine which of the three receptors are expressed in enteric neurons, we measured the percentage of cells positive for CHRM1, CHRM3, and CHRM5, and found that CHRM3 and CHRM5 are the most abundant, whereas CHRM1 is expressed at negligible levels in both ESC and iPSC-derived enteric neurons (Figure 2.6C).

To understand which of the two expressed receptors are driving oxybutynin's rescue effect, we targeted ESCs with *CHRM3* and *CHRM5* CRISPR-cas9 ribonucleoproteins (RNPs). Gene editing was effective at reducing targeted protein levels in differentiated enteric neurons (Figure 2.6D). We did not observe any compensation affecting cholinergic receptor levels in the targeted cells (Figure 2.6E). Furthermore, the targeted lines recapitulate the representation of key enteric neuron subtype markers, indicating that gene editing did not affect differentiation quality or lineage trajectories (Figure 2.6F). Treatment with *CHRM3* and *CHRM5* RNPs significantly reduced the percentage of cells positive for cleaved caspase 3 in response to oxaliplatin exposure (Figure 2.5F). Oxybutynin co-treatment in the *CHRM3* and *CHRM5* targeted lines did not significantly reduce apoptosis levels further, indicating that both proteins are downstream of oxybutynin (Figure 2.5F).

Altogether, our results indicate that platin-induced hyperexcitability and enteric neurotoxicity is mediated through CHRM3 and CHRM5 signaling, and oxybutynin can counteract these toxic effects by antagonizing these receptors.

2.3.4 Enteric nitrenergic neurons are selectively vulnerable to platin-induced excitotoxicity

Enteric neurons are heterogeneous, composed of a diverse array of molecularly, structurally, and functionally distinct neuronal subtypes^{29,30}. Furthermore, many enteric neuropathies, also known as disorders of gut-brain interaction, are caused by the loss or dysfunction of a specific enteric neuron subtype^{53,54}. Therefore, we sought to determine how our platin-induced excitotoxicity pathway may be represented in different enteric neurons and how muscarinic cholinergic receptor antagonism may help protect them (Figure 2.7A). Thus, we performed a single nuclei RNA sequencing (snRNA-seq) experiment on our hPSC-derived enteric neurons treated with oxaliplatin, with and without oxybutynin to capture the cell-type specific transcriptional effects of these drugs. Dimensionality reduction and unbiased clustering revealed 10 transcriptionally distinct cell type clusters present in our cultures that do not cluster based on treatment condition (Figure 2.8A). Based on the expression of respective lineage markers, clusters 1, 2, 3, 5, 7, and 8 were annotated as progenitor populations, cluster 4 as enteric neurons, cluster 6 as enteric glia, cluster 8 as enteric neural crest cells, and cluster 9 as smooth muscle cells, as defined based on the expression of their respective lineage markers (Figure 2.8B).

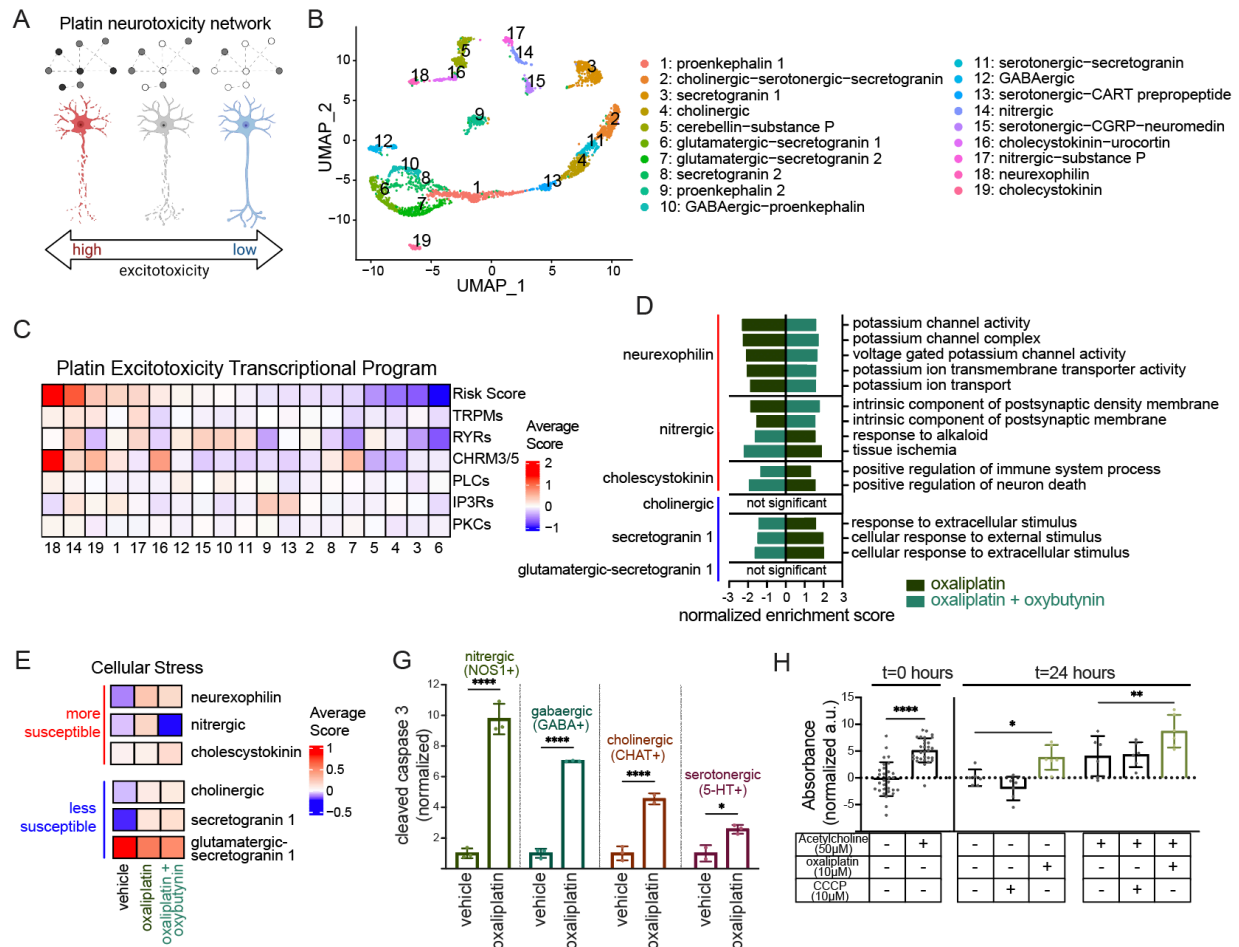


Figure 2.7 Single nuclei transcriptomic profiling identifies subtypes susceptible to platinum-induced excitotoxicity

A) Schematic illustration of our hypothesis that enteric neuron subtypes are differentially susceptible to platin toxicity based on their expression of platin-induced excitotoxicity pathway genes.

B) sn-RNAseq UMAP of enteric neuron subtypes present in our stage 1 2D enteric neuron cultures.

C) Heatmap of the average module scores of the platin excitotoxicity transcriptional program gene categories in the stage 1 2D enteric neuron subtypes.

D) Bar plot of the Ontology neurotransmission and cellular stress related gene sets rescued by oxybutynin co-treatment in the stage 1 2D enteric neuron subtypes predicted to be most susceptible (neurexophilin, nitrgenic, and cholecystokinin) and least susceptible (cholinergic, secretogranin 1, and glutamatergic-secretogranin 1) to platin-induced excitotoxicity.

E) Heatmaps of the average module scores of the combined list of all genes in the Hallmark gene sets (combined cellular stress score) in the stage 1 2D enteric neuron subtypes predicted to be most susceptible (neurexophilin, nitrgenic, and cholecystokinin) and least susceptible (cholinergic, secretogranin 1, and glutamatergic-secretogranin 1) to platin-induced excitotoxicity.

F) Quantification of flow cytometry analysis detecting cleaved caspase 3 levels during 20 µM oxaliplatin treatment in four enteric neurotransmitter identities: nitrgenic (NOS1+), GABAergic (GABA+), cholinergic (CHAT+), and serotonergic (5-HT+) stage 1 2D enteric neurons. Vehicle contains water diluted to 2% in medium. Data are represented as mean ± SD.

G) Quantification of calorimetry-based method for detecting nitric oxide levels with and without acetylcholine stimulation in the stage 1 2D enteric neuron cell culture supernatants prior to drug treatment (t=0 hours) and after 24 hours exposure to oxaliplatin and CCCP. Data is normalized by subtracting the vehicle (medium containing 1% water) pre-treatment (t=0 hours) condition from each sample. Data are represented as mean \pm SD.

* p value < 0.05, ** p value < 0.01, **** p value < 0.0001, ns: not significant.

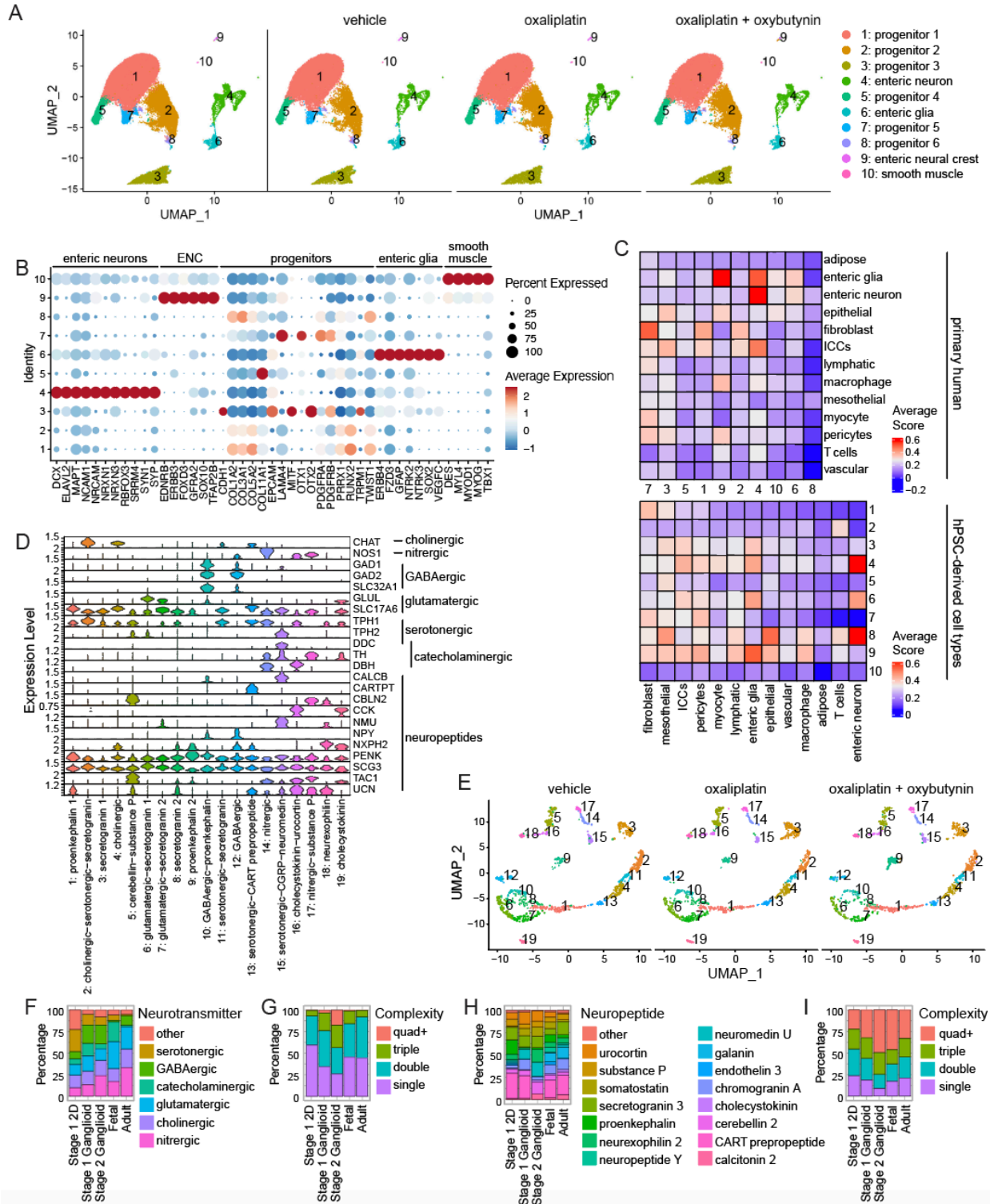


Figure 2.8 hPSC-derived 2D enteric neurons recapitulate human enteric neuron neurochemical diversity

A) sn-RNAseq UMAPs of cell types present in the hPSC-derived enteric neuron culture showing all cells (left) and the cells from each treatment condition: vehicle (medium containing 1% water), 10 μ M oxaliplatin, and 10 μ M oxaliplatin + 5 μ M oxybutynin (right).

B) Dot plot showing the expression of canonical enteric neuron, enteric neural crest (ENC), progenitor, enteric glia, and smooth muscle markers in the vehicle-treated stage 1 2D culture cell types.

C) Heatmaps of the average module scores of adult human colon cell type transcriptional signatures in hPSC-derived cell types (top) and the average module scores of hPSC-derived cell type transcriptional signatures in adult human colon cell types (bottom).

D) Dot plot showing the expression of enteric neuron neurochemical identity markers in the hPSC-derived enteric neuron subtypes.

E) sn-RNAseq UMAPs of neuronal subtypes present in our hPSC-derived enteric neurons from each treatment condition: vehicle (medium containing 1% water), 10 μ M oxaliplatin, and 10 μ M oxaliplatin + 5 μ M oxybutynin (right).

F-G) Bar plots of the overall representation of neurotransmitter synthesizing neurons (left) and mono- and multi-neurotransmitter synthesizing neurons (right) in stage 1 2D enteric neurons compared to stage 1 and 2 enteric ganglioids and human primary fetal and adult enteric neurons.

H-I) Bar plots of the overall representation of neuropeptide expressing neurons (left) and mono- and multi-neuropeptide expressing neurons (right) in stage 1 2D enteric neurons compared to stage 1 and 2 enteric ganglioids and human primary fetal and adult enteric neurons.

To validate that our hPSC-derived enteric neurons recapitulate the identity of human enteric neurons *in vivo*, we compared them to a snRNA-seq dataset of the primary human colon previously published by Regev and colleagues². Module scoring of the transcriptional signatures of the primary cell types on our hPSC-derived cell types demonstrated that the enteric neuron populations are highly similar, with our enteric neuron cluster 4 showing the highest average expression of primary human enteric neuron genes (Figure 2.8C). The reverse analysis, scoring the expression of our stage 1 2D enteric neuron genes in the primary human dataset, validated these findings, resulting in the primary enteric neurons having the highest average expression of our hPSC-derived enteric neuron genes (Figure 2.8C). Thus, our *in vitro* hPSC-derived enteric neurons share the same transcriptional identity as their *in vivo* counterparts.

To identify the neuronal subtypes represented in our hPSC-derived enteric neurons, we sub-clustered the neuronal population. Sub-clustering revealed 19 transcriptionally distinct enteric neuron clusters which were annotated by neurochemical identity based on their expression of neurotransmitter processing genes and neuropeptides (Figure 2.7B and 2.8D). Cells from the drug treatment conditions appear to cluster by neuronal subtype identity, as all 19 subtypes are represented in each of the three treatment conditions (Figure 2.8E).

Next, we set out to determine if our hPSC-derived enteric neurons (henceforth referred to as “stage 1 2D enteric neurons” based on their differentiation stage and format) contain the same neuronal diversity as other published enteric neuron datasets. We compared the neurochemical composition of our dataset to hPSC-derived stage 1 and stage 2 ganglioid (3D) enteric neurons published by our group³³, primary fetal human enteric neurons published by Teichmann and colleagues⁵⁵, as well as primary adult human colonic enteric neurons published by Regev and colleagues². For neurotransmitters, we utilized a two-step neurochemical identity-defining approach, that our group has reported previously, to identify all the cells that belong to six neurotransmitter identities: serotonergic, GABAergic, catecholaminergic, glutamatergic, cholinergic, and nitrergic³³. We found that all six neurochemical identities are represented in our cultures, recapitulating the neurotransmitter diversity of other datasets (Figure 2.8F). Furthermore, enteric neurons that produce multiple neurotransmitters have recently been characterized in some detail³³. To determine if our stage 1 2D enteric neurons recapitulate the same neurotransmitter complexity as other enteric neuron tissues, we quantified the number of

cells predicted to synthesize only one, two, three, or more neurotransmitters across all five datasets. Here neurotransmitter complexity was also reproduced, with our stage 1 2D enteric neurons containing cells with all four levels of complexity (Figure 2.8G). Next, we characterized the representation and complexity of neuropeptides and identified 15 identities based on the expression of neuropeptide genes including calcitonin 2, CART prepropeptide, cerebellin 2, cholecystokinin, chromogranin A, endothelin 3, galanin, neuromedin U, neuropeptide Y, neuroexophilin 2, proenkephalin, secretogranin 3, somatostatin, substance P, and urocortin. All five datasets have representation from all 15 neuropeptide identities with the exception of the stage 2 ganglioid enteric neurons, which only have 14, lacking CAPT prepropeptide expressing cells likely due to a sampling issue (Figure 2.8H). Detecting neuropeptide complexity in each dataset based on the number of cells expressing one, two, three, or more neuropeptides again revealed that different levels of neuropeptide complexity are represented across all five datasets (Figure 2.8I). Thus, our stage 1 2D enteric neurons recapitulate the neurochemical representation and complexity of other enteric neuron datasets, including hPSC-derived enteric ganglioids and primary human enteric neurons.

To predict which enteric neuron subtypes are more susceptible to the platin-induced excitotoxicity mechanism, we performed module scoring on our vehicle-treated enteric neuron subtypes for their expression of genes contributing to various steps in the platin-induced excitotoxicity pathway, which we term the platin excitotoxicity transcriptional program. Transcripts in this program include transient receptor potential channels, ryanodine receptors, CHRM3 and CHRM5, PLC enzymes, IP3 receptors, and PKC

enzymes (Table 2.7 and Figure 2.7C). We also module scored the neurons using a combined transcript list to generate an overall risk score for each of the enteric neuron subtypes (Figure 2.7C). The neurexophilin, nitrenergic, and cholecystokinin populations were predicted to be the most susceptible enteric neuron subtypes. The neurexophilin population's high-risk score is primarily driven by high relative expression of *CHRM3* and *CHRM5*, whereas nitrenergic neurons have high relative expression of all six gene categories (Figure 2.7C). Although neurexophilin and cholecystokinin enteric neurons have been identified in the ENS and appear to have a transcriptional profile associated with intrinsic primary afferent neurons, their functional role in the ENS and association with enteric neuropathies has been understudied^{56–58}. Nitrenergic neurons, on the other hand, are better characterized, releasing nitric oxide to relax smooth muscle cells in the GI tract, thereby promoting GI motility³⁹. Enteric neuropathies associated with nitrenergic neurons include achalasia, hypertrophic pyloric stenosis, and gastroparesis³⁹. Furthermore, in a mouse model of oxaliplatin-induced enteric neuropathy, nitrenergic neuron-mediated electrophysiological activities and motility functions are disrupted, which aligns with our data, predicting them to be more susceptible to oxaliplatin-induced excitotoxicity⁹. The cholinergic, secretogranin 1, and glutamatergic-secretogranin 1 populations, on the other hand, were predicted to be the least susceptible enteric neuron subtypes with low expression of virtually every gene category involved in the platin-induced excitotoxicity pathway (Figure 2.7C).

Next, we assessed if our predictions are reflected in the transcriptional changes induced by the drug treatments in each of the subtypes. To do this, we performed pre-ranked

GSEA on the genes differentially expressed between vehicle and oxaliplatin-treated neurons and oxaliplatin and oxaliplatin-oxybutynin co-treated neurons for the neurexophilin, nitrenergic, cholecystokinin, cholinergic, secretogranin 1, and glutamatergic-secretogranin 1 populations. We filtered the significant gene sets using a p-value cutoff of < 0.05 , then identified the gene sets with opposite normalized enrichment scores for each of the comparisons per population, indicating gene sets rescued by oxybutynin co-treatment. Focusing on the gene sets relating to neurotransmission and cellular stress pathways, we identified five that were rescued for neurexophilin neurons, four for nitrenergic neurons, two for cholecystokinin neurons, three for secretogranin 1 neurons, and none for cholinergic neurons or glutamatergic-secretogranin 1 neurons (Figure 2.7D). Many of the reversed gene sets were related to neuronal activity, synaptic function, or cellular stress (Figure 2.7D).

To validate these findings, we module scored the neurexophilin, nitrenergic, cholecystokinin, cholinergic, secretogranin 1, and glutamatergic-secretogranin 1 populations for their expression of the rescued neurotransmission and cellular stress related gene sets. Comparing the average relative expression of each module across each population's treatment conditions, we observed that the neurexophilin, nitrenergic, and cholecystokinin subtypes exhibit expression patterns that are partially or fully reversed (Figure 2.9A). This pattern is not observed in the cholinergic, secretogranin 1, and glutamatergic-secretogranin 1 subtypes where only one or two of the gene sets are modulated by oxaliplatin and rescued by oxybutynin (Figure 2.9A). All together, these analyses indicate that neurotransmission and cellular stress related pathways in cholinergic, secretogranin

1, and glutamatergic-secretogranin 1 enteric neurons are less affected by oxaliplatin chemotherapy than they are in the neurexophilin, nitroergic, and cholecystokinin enteric neuron subtypes. Furthermore, oxybutynin can largely reverse these oxaliplatin-induced neurotransmission and cellular stress related transcriptional changes, particularly in the subtypes predicted to be more susceptible to platin-induced excitotoxicity.

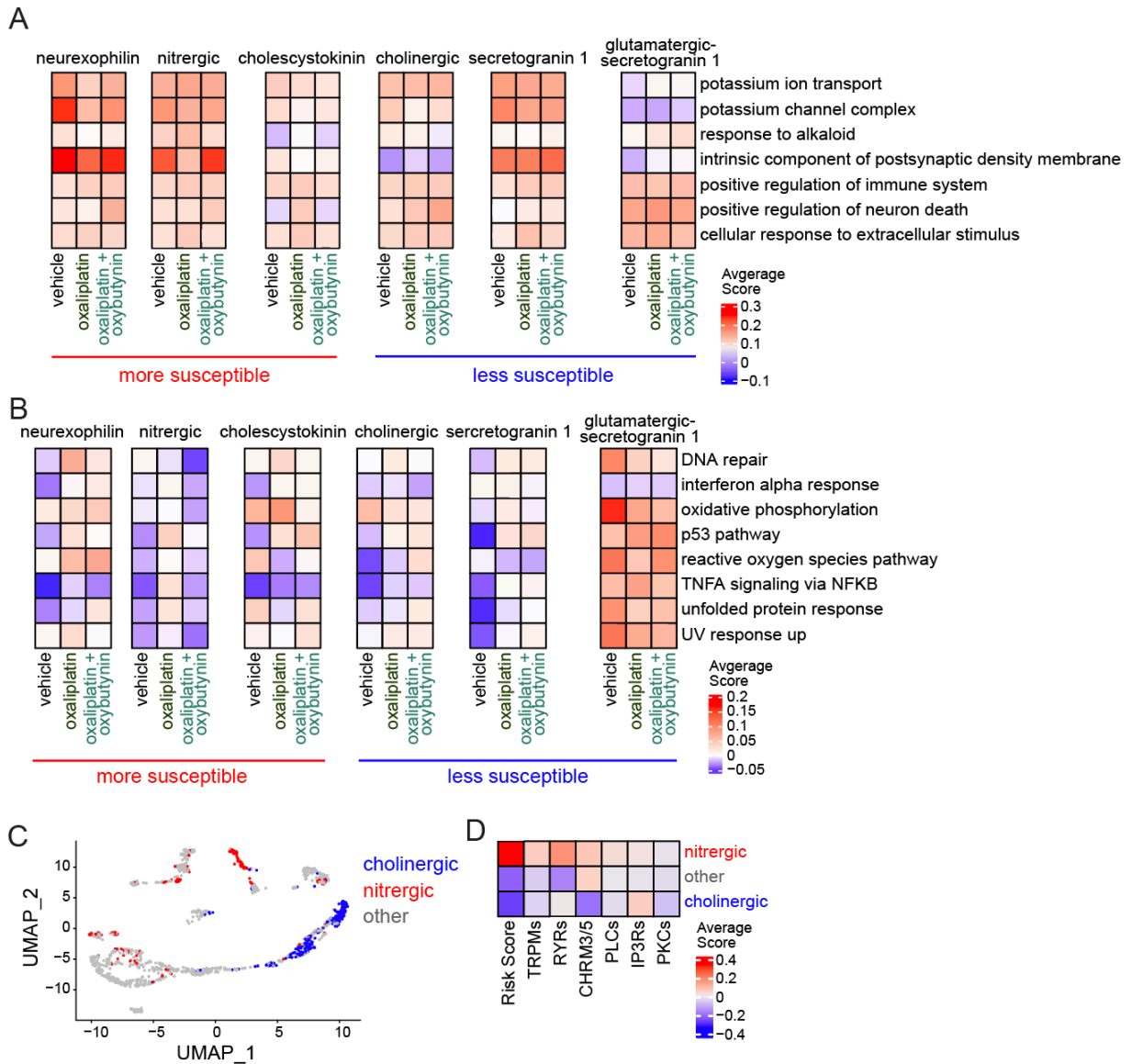


Figure 2.9 Cell type specific transcriptional profiling of platin-induced excitotoxicity susceptibility

A) Heatmaps of the average module scores of select Ontology neurotransmission and cellular stress related gene sets in the hPSC-derived enteric neuron subtypes predicted to be most susceptible (neurexophilin, nitrenergic, and cholecystokinin) and least susceptible (cholinergic, secretogranin 1, and glutamatergic-secretogranin 1) to platin-induced excitotoxicity.

B) Heatmaps of the average module scores of select Hallmark cellular stress related gene sets in the stage 1 2D enteric neuron subtypes predicted to be most susceptible (neurexophilin, nitrenergic, and cholecystokinin) and least susceptible (cholinergic, secretogranin 1, and glutamatergic-secretogranin 1) to platin-induced excitotoxicity.

C) sn-RNAseq UMAP of hPSC-derived enteric neurons predicted to be cholinergic (CHAT producing), nitrenergic (NOS1 producing), or other (neither CHAT nor NOS1 producing).

D) Heatmap comparing the average module scores of the platin excitotoxicity transcriptional program gene categories in the hPSC-derived enteric neurons predicted to be cholinergic (CHAT producing), nitrenergic (NOS1 producing), or other (neither CHAT nor NOS1 producing).

To more robustly characterize the cellular stress related transcriptional changes induced by the drug treatments in the subtypes predicted to be more susceptible and less susceptible to platin-induced excitotoxicity, we module scored the neurexophilin, nitrenergic, cholecystokinin, cholinergic, secretogranin 1, and glutamatergic-secretogranin 1 populations for their expression of all the Hallmark cellular stress related gene sets. These gene lists were combined, and all the neurons were module scored for the combined gene list to generate an overall cellular stress score for each of the populations. The average relative expression of the cellular stress transcriptional signature was increased by oxaliplatin and decreased by oxybutynin co-treatment for both the neurexophilin and nitrenergic subtypes (Figure 2.7E). This pattern was not reflected in the cholinergic, secretogranin 1, and glutamatergic-secretogranin 1 subtypes, where the average relative expression of the cellular stress module increased slightly for the cholinergic and secretogranin 1 neurons and decreased slightly for the glutamatergic-secretogranin 1 neurons (Figure 2.7E). This cellular stress expression pattern of rescue for the two subtypes predicted to be the most susceptible to our platin-induced excitotoxicity mechanism is largely explained by eight of the cellular stress related Hallmark gene sets, including transcriptional changes related to DNA damage, oxidative stress, apoptosis,

and inflammation (Figure 2.9B). These pathways overlap with the cellular stress hallmarks we identified through bulk RNA sequencing and follow-up experimental validations (Figure 2.2, Figure 2.1D), suggesting that the transcriptional and phenotypic changes we observed may be largely explained by the subtypes we predicted to be more susceptible to platin-induced excitotoxicity.

We were intrigued by the prediction that nitrergic neurons (clusters 14 and 17) are more susceptible to platin-induced excitotoxicity and cholinergic neurons (clusters 2 and 4) are less susceptible (Figure 2.7C), since proper GI motility is maintained through a balance of cholinergic (excitatory) and nitrergic (inhibitory) motor neuron signaling^{29,30}. Cholinergic neurons release acetylcholine to promote the contraction of smooth muscle cells that drive GI motility and nitrergic neurons are responsible for inducing muscle relaxation through the release of nitric oxide^{29,30}. So, a selective loss of nitrergic neurons following platin chemotherapy treatment could lead to excessive contraction of the smooth muscle tissue contributing to the dysfunctional GI symptoms experienced by patients (Figure 2.1B, Table 2.3). To continue interrogating this hypothesis, we further characterized the vehicle-treated enteric neurons, detecting the expression of the plain excitotoxicity transcriptional program genes in nitrergic and cholinergic neurons relative to all the other enteric neurons in our dataset. We defined the nitrergic neuron clusters based on the high percentage of cells expressing the nitric oxide rate limiting enzyme *NOS1* (Figure 2.8D). However, some *NOS1* expressing cells can be found in other clusters (Figure 2.8D). Similarly, cholinergic neurons, expressing the acetylcholine rate limiting enzyme *CHAT*, exist outside of the cholinergic neuron clusters (Figure 2.9C). To take a more holistic look

at these two these populations, we identified all nitroergic neurons and cholinergic neurons using our two-step neurochemical identity-defining approach³³, thereby binning all enteric neurons in our dataset into nitroergic, cholinergic, or other categories (Figure 2.9C). We then module scored the nitroergic, cholinergic, and other neurons based on their expression of the genes in the platin excitotoxicity transcriptional program (Table 2.7). Nitroergic neurons have a higher relative expression of the platin-induced excitotoxicity related genes relative to other enteric neurons, whereas cholinergic neurons have a lower relative expression of these same genes relative to other enteric neurons (Figure 2.9D). These data further support our prediction that nitroergic neurons are more susceptible and cholinergic neurons are less susceptible to platin-induced excitotoxicity.

To experimentally validate if nitroergic neurons are indeed more susceptible to platins than other enteric neuron subtypes, we detected levels of oxaliplatin-induced cleaved caspase 3 across four enteric neurotransmitter identities: CHAT+ cholinergic neurons, GABA+ gabaergic neurons, NOS1+ nitroergic neurons, and 5-HT+ serotonergic neurons. Apoptosis was induced to different degrees across these populations, with the nitroergic population showing the strongest response, with apoptosis levels increasing nearly 10-fold relative to vehicle-treated nitroergic neurons (Figure 2.7F). Apoptotic cholinergic neurons, on the other hand, only increased 4.5-fold relative to vehicle levels (Figure 2.7F). These results confirm that nitroergic neurons are more susceptible to oxaliplatin relative to other enteric neuron populations.

To validate that the increased susceptibility of nitrergic neurons to oxaliplatin is a consequence of oxaliplatin-induced hyperexcitability, we measured the levels of nitric oxide released by the nitrergic neurons as a result of their electrical activity. Stimulation with acetylcholine leads to an increase in nitric oxide release by the nitrergic neurons (Figure 2.7G). This result functionally validates that nitrergic neurons are responsive to acetylcholine, as predicted based on their expression of *CHRM3* and *CHRM5* (Figure 2.7C and Figure 2.9D). We then exposed our enteric neuron cultures to oxaliplatin for 24 hours and measured the levels of nitric oxide released into the medium in the presence and absence of acetylcholine stimulation. In both conditions, we observed that oxaliplatin-treated nitrergic neurons released significantly more nitric oxide than their vehicle-treated counterparts. This effect was not observed when the cells were treated with the mitochondrial toxin CCCP, indicating that the effect is specific to oxaliplatin toxicity and not due to a general susceptibility of nitrergic neurons to cellular stress (Figure 2.7G).

Altogether, our results indicate that enteric neuron subtypes are differentially susceptible to platin chemotherapies. We demonstrated that nitrergic neurons show a stronger apoptotic response relative to other neurons. Furthermore, this increased level of cell death is preceded by hyperexcitability of nitrergic neurons and increased release of nitric oxide. These data suggest that preserving the susceptible neuronal subtypes by inhibiting cholinergic signaling, might be a promising therapeutic approach to prevent the clinical symptoms of platin-induced GI neurotoxicity.

2.3.5 Oxybutynin prevents oxaliplatin-induced enteric neuropathy in mice

Our results suggest that cholinergic signaling, mediated through CHRM3 and CHRM5, increases the sensitivity of enteric neurons to platins via an excitotoxicity mechanism, which occurs in a subtype-specific manner, based on the expression of the platin excitotoxicity transcriptional program. To determine if hallmarks of platin-induced excitotoxicity are represented in platin chemotherapy patient tissue, we acquired archived histologically normal gastric tissue from prior gastrectomies for gastric cancer, that either did not receive chemotherapy prior to tumor resection or did undergo platin chemotherapy prior to tumor resection (Figure 2.10A). We first evaluated if platin chemotherapy treatment increases activity of the inositol phospholipid signaling pathway, a key component of the platin excitotoxicity mechanism, by detecting p-PKC levels by immunostaining. Similar to what we observed *in vitro*, patients that had received platin chemotherapy prior to their surgery had elevated p-PKC levels in their enteric neurons relative to the patients that had not undergone chemotherapy (Figure 2.5C-D, Figure 2.6A, Figure 2.10B-C). These data support our findings that platins increase inositol phospholipid signaling and PKC activity in human enteric neurons. To evaluate if platin chemotherapy treatment alters the representation of the enteric neuron subtypes we identified as more or less susceptible to platin-induced excitotoxicity, we detected nitrergic neurons and cholinergic neurons based on the colocalization of the pan-neuronal marker HuC/D with NOS1 and CHAT, respectively, by immunostaining (Figure 2.10D). We quantified the proportion of NOS1+ CHAT-, CHAT+ NOS1-, and CHAT+ NOS1+ enteric neurons in each patient group (Figure 2.10E). The proportion of NOS1+ CHAT- enteric

neurons was significantly reduced, while the proportion of CHAT+ NOS1- enteric neurons was significantly increased in patients that received platin chemotherapy prior to surgery relative to those that did not undergo chemotherapy (Figure 2.10E). These data support our *in vitro* observations that nitrergic enteric neurons are selectively vulnerable to platin chemotherapies as compared to the more resistant cholinergic subtype.

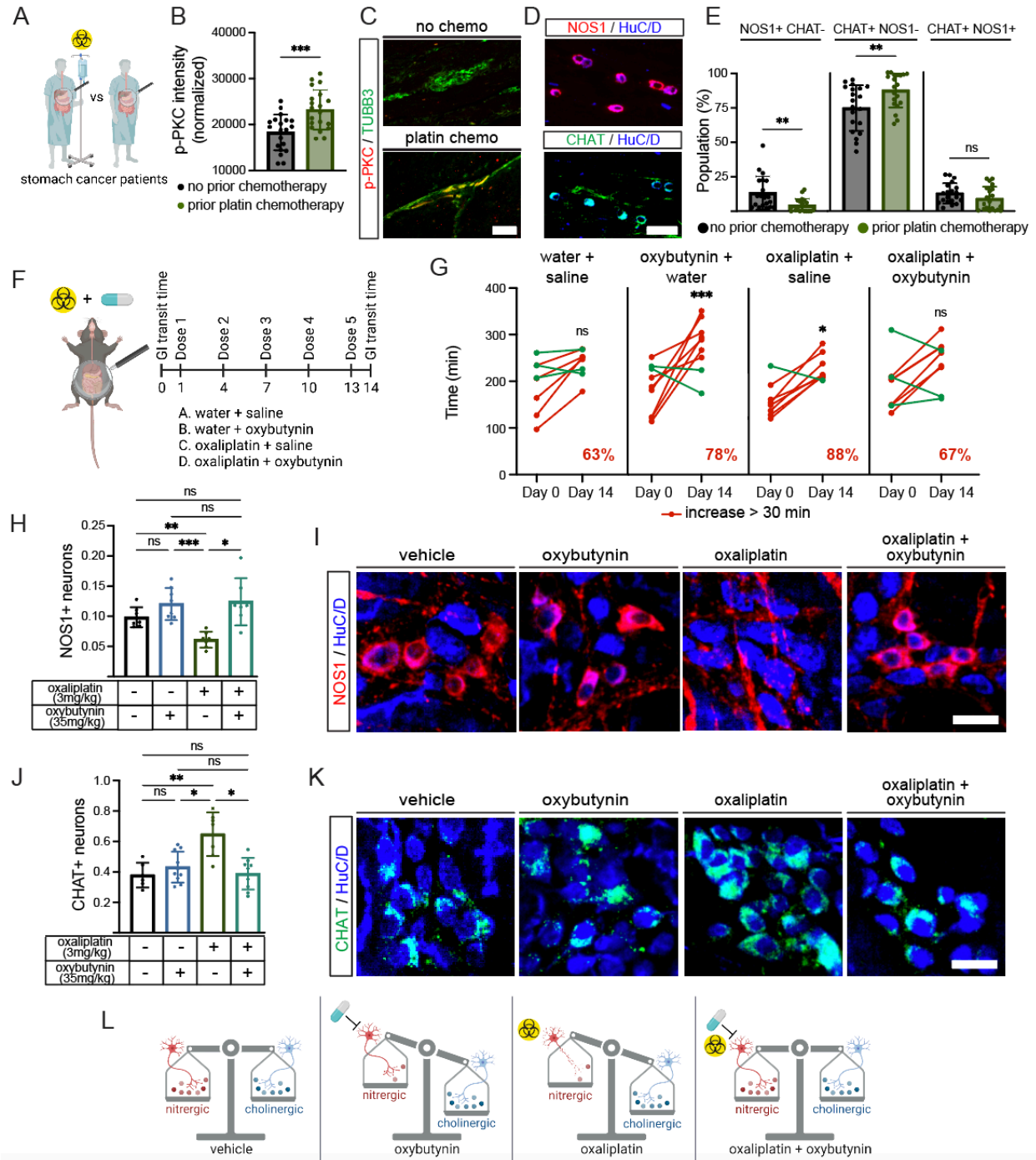


Figure 2.10 Selective loss of nitroergic enteric neurons during platin treatment can be prevented by oxybutynin

A) Schematic illustration of our strategy to stratify gastric cancer patients to compare by immunostaining the enteric neurons of patients that received platin chemotherapy to patients that received no chemotherapy prior to their tumor resection surgeries. All staining was done in non-cancerous healthy tissue margins from the surgical samples.

B, C) Immunofluorescence staining and quantification of primary human stomach sections for protein kinase C activity marker phosphorylated protein kinase C (p-PKC) and neuronal marker TUBB3 comparing patients that received platin chemotherapy to patients that received no chemotherapy prior to their tumor resection surgeries. Data are represented as mean \pm SD. Scale bar: 50 μ m.

D) Immunofluorescence staining of primary human stomach sections for nitrenergic neuron marker NOS1 and cholinergic neuron marker CHAT. Scale bar: 25 μ m.

E) Bar plot showing the proportion of NOS1+ CHAT- nitrenergic neurons, CHAT+ NOS1- cholinergic neurons, and CHAT+ NOS1+ dual identity enteric neurons in primary human stomach sections of patients that received platin chemotherapy to patients that received no chemotherapy prior to their tumor resection surgeries. Data are represented as mean \pm SD.

F) Schematic illustrating the design of our mouse study where mice were dosed with oxaliplatin (3 mg/kg per dose), oxybutynin (35 mg/kg per dose), oxaliplatin's vehicle (3 mg/kg water per dose), and oxybutynin's vehicle (35 mg/kg 5% DMSO and 2% tween80 in saline). GI transit time was measured before and after the dosing regimen. Enteric neurons were then compared between the different treatment conditions by immunostaining.

G) Paired analysis of GI transit times for each animal by treatment condition comparing GI transit times of the animals before and after the dosing regimen. Red lines represent mice that experienced a > 30 minute increase in their GI transit. Green lines represent mice that experienced < 30 minute increase in their GI transit. Percentages reflect the percentage of mice per condition that experienced a > 30 minute increase in their GI transit.

H, I) Nitrenergic neuron marker NOS1 and neuronal nuclei marker (HuC/D) staining and quantification in vehicle (3 mg/kg water + 35 mg/kg 5% DMSO and 2% tween80 in saline), oxybutynin (35 mg/kg oxybutynin + 3 mg/kg water), oxaliplatin (3 mg/kg oxaliplatin + 35 mg/kg 5% DMSO and 2% tween80 in saline), and oxaliplatin + oxybutynin (3 mg/kg oxaliplatin + 35 mg/kg oxybutynin)-treated mice. Data are represented as mean \pm SD. Scale bar: 25 μ m.

J, K) Cholinergic neuron marker CHAT and neuronal nuclei marker (HuC/D) staining and quantification in vehicle (3 mg/kg water + 35 mg/kg 5% DMSO and 2% tween80 in saline), oxybutynin (35 mg/kg oxybutynin + 3 mg/kg water), oxaliplatin (3 mg/kg oxaliplatin + 35 mg/kg 5% DMSO and 2% tween80 in saline), and oxaliplatin + oxybutynin (3 mg/kg oxaliplatin + 35 mg/kg oxybutynin)-treated mice. Data are represented as mean \pm SD. Scale bar: 25 μ m.

L) Schematic illustrating conclusions from the mouse study.

* p value < 0.05, ** p value < 0.01, *** p value < 0.001, ns: not significant.

To determine if muscarinic cholinergic receptor antagonism, via oxybutynin, can prevent the cellular and physiological hallmarks of platin-induced GI neurotoxicity *in vivo*, we designed a mouse experiment including four treatment conditions: vehicle-treated mice injected with water and saline, oxybutynin-treated mice injected with water and oxybutynin, oxaliplatin-treated mice injected with oxaliplatin and saline, and oxaliplatin and oxybutynin co-treatment mice injected with both oxaliplatin and oxybutynin (Figure 2.10F). All mice were injected following an established dosing regimen previously shown

to induce hallmarks of oxaliplatin-induced enteric neuropathy^{8,9}. The total GI transit time of each mouse was measured on days zero and 14 to assess if the treatments significantly change the time it takes for food to pass through the GI tract (Figure 2.10F). Consistent with previous reports^{8,9}, oxaliplatin treatment led to significantly longer GI transit times, with 88% of the mice showing an increase of more than 30 minutes (Figure 2.10G). Oxybutynin treatment alone also significantly increased GI transit time, with 78% of the mice showing a more than 30 minute increase (Figure 2.10G). This result likely reflects oxybutynin' antagonizing effect on muscarinic receptors in the ENS. Mice co-treated with oxaliplatin and oxybutynin, however, did not exhibit significant increases in GI transit time (Figure 2.10G). These results highlight the therapeutic potential of oxybutynin to prevent physiological hallmarks of platin-induced GI neuropathy.

Our data suggests that antagonizing muscarinic cholinergic receptors during platin treatment can prevent clinical features of platin-induced GI neurotoxicity. We next sought to determine if the functional outcome of oxaliplatin-induced constipation in our study reflects a change in representation of neuronal subtypes in the ENS and evaluate whether oxybutynin can rescue these cellular features. We quantified the number of nitrergic and cholinergic neurons in the distal colon of the treated mice using immunostaining of the pan neuronal marker HuC/D with NOS1 and CHAT, respectively. The proportion of nitrergic neurons in the mice treated with oxaliplatin was significantly reduced, nearly in half, relative to vehicle levels (Figure 2.10H-I). Oxybutynin co-treatment was able to prevent the oxaliplatin-induced reduction of the nitrergic neuron population, suggesting that oxybutynin can protect this susceptible subtype from platin toxicity *in vivo* (Figure

2.10H-I). Conversely, the proportion of cholinergic neurons in mice treated with oxaliplatin was significantly increased relative to vehicle levels, suggesting this population is resistant to platins and becomes overrepresented in the tissue (Figure 2.10J-K). Oxybutynin co-treatment was able to prevent this overrepresentation, likely through its preservation of more vulnerable enteric neuron subtypes, such as the nitrergic neurons (Figure 2.10J-K). Mice treated only with oxybutynin did not exhibit significant changes in their neuronal proportions relative to vehicle-treated mice, suggesting that the prolonged GI transit time exhibited by these animals reflects a reduction in nitrergic neuron activity, via muscarinic cholinergic receptor antagonism, rather than a loss of the neuronal population due to toxicity (Figure 2.10H-K).

Altogether, the results suggest that platin treatment disrupts the balance between nitrergic and cholinergic neuron levels and activity required for proper GI function under normal conditions (Figure 2.10L). Selective vulnerability of nitrergic neurons to platins creates an imbalance in the ENS characterized by an overrepresentation of excitatory cholinergic neurons and an underrepresentation of inhibitory nitrergic neurons, thereby causing GI dysmotility (Figure 2.10L). When treated alone, oxybutynin antagonizes muscarinic cholinergic receptors on inhibitory nitrergic neurons, dampens their activity and leads to slow GI transit (Figure 2.10L). However, in combination with oxaliplatin treatment, oxybutynin prevents platin-induced excitotoxicity, thereby preserving the vulnerable nitrergic neurons and preventing platin-induced GI dysmotility (Figure 2.10L). In summary, these data support muscarinic cholinergic receptor antagonism as a viable therapeutic strategy to prevent platin-induced GI neuropathy.

2.6 Tables

Table 2.1 Characteristics of individuals with colorectal cancer extracted from UCSF Research Data Browser

Characteristic	Oxaliplatin (n = 46)	No oxaliplatin (n = 169)
Age, mean (SD)	54 (14)	58 (10)
Female (%)	28 (61%)	122 (72%)
Male (%)	18 (39%)	47 (28%)
Race/ethnicity		
American Indian or Alaska Native (%)	1 (2%)	1 (0.6%)
Asian (%)	7 (15%)	10 (6%)
Black or African American (%)	1 (2%)	1 (0.6%)
White (%)	32 (70%)	153 (91%)
Other (%)	5 (11%)	4 (2%)

Table 2.2 Characteristics of individuals with ovarian cancer extracted from UCSF Research Data Browser

Characteristic	Carboplatin (n = 438)	No carboplatin (n = 3649)
Age, mean (SD)	59 (12)	58 (11)
Female (%)	437 (100%)	3648 (100%)
Male (%)	1 (0.2%)	1 (0.03%)
Race/ethnicity		
American Indian or Alaska Native (%)	3 (0.7%)	3 (0.08%)
Asian (%)	65 (15%)	195 (5%)
Black or African American (%)	11 (3%)	29 (0.8%)
Native Hawaiian or Other Pacific Islander (%)	4 (0.9%)	12 (0.3%)
White (%)	272 (62%)	2824 (77%)
Other (%)	87 (20%)	598 (16%)

Table 2.3 Prevalence of constipation in patients that received platin chemotherapy and untreated patients

Platin	Matched Patients				Odds Ratio	Chi-Squared <i>P</i> value
	On drug without constipation diagnosis (N)	On drug with constipation diagnosis (N)	Off drug without constipation diagnosis (N)	Off drug with constipation diagnosis (N)		
oxaliplatin	19	27	119	50	3.36	0.0005062
carboplatin	224	214	3267	382	8.17	2.2 × 10 ⁻¹⁶

Table 2.4 Cytokine array results showing average MFI (n=3) normalized to vehicle

	enteric neurons			other peripheral neurons		
	cisplatin	carboplatin	oxaliplatin	cisplatin	carboplatin	oxaliplatin
6CKINE / CCL21 / EXODUS2	0.98	0.99	0.98	1.01	0.99	1.06
BCA1 / CXCL13	1.64	0.74	1.26	3.36	3.55	4.68
CTACK / CCL27	1.04	0.99	1.15	1.04	1.08	1.06
EGF	1.08	1.04	1.03	0.91	0.90	0.93
ENA78 / CXCL5	1.09	1.00	0.95	0.93	0.87	0.92
EOTAXIN / CCL11	1.66	1.06	1.14	0.92	1.17	1.22
EOTAXIN2 / CCL24 / MPIF2	0.97	0.93	0.97	1.03	1.09	1.09
EOTAXIN3 / CCL26	1.01	0.94	0.94	1.02	1.02	1.07
FASL	1.12	1.06	1.05	1.28	1.17	1.10
FGF2 / FGFB	1.20	1.18	1.23	1.14	1.20	1.40
FLT3L	1.03	1.03	0.87	0.98	1.14	1.43
FRACTALKINE / CX3CL1	0.78	1.13	0.46	0.88	1.05	1.19
GCSF	1.11	1.20	1.12	1.06	1.02	0.98
GMCSF	1.57	1.56	1.23	0.93	0.96	1.01
GROA	3.16	1.37	1.02	0.56	0.45	0.90
HGF	1.34	0.97	1.26	1.06	0.57	0.74
I309 / CCL1	4.00	1.21	2.74	1.03	1.07	1.23
IFNA2	1.04	0.94	1.07	1.04	1.34	1.44
IFNG	1.28	1.09	1.16	1.09	1.17	1.57
IL10	0.89	0.73	0.72	0.92	1.13	1.25
IL12P40	1.07	0.95	1.05	0.92	1.11	1.13
IL12P70	0.94	0.89	0.98	0.93	1.13	1.39

	enteric neurons			other peripheral neurons		
	cisplatin	carboplatin	oxaliplatin	cisplatin	carboplatin	oxaliplatin
IL13	1.38	1.31	1.29	0.81	1.01	1.18
IL15	0.91	0.92	0.95	0.90	1.13	1.21
IL16	1.14	1.07	1.09	0.95	0.99	1.02
IL17A / CTLA8	1.04	1.00	1.13	0.92	1.04	1.17
IL18	1.23	1.01	1.06	0.94	1.14	1.21
IL1A	1.34	1.35	1.14	0.94	0.93	0.91
IL1B	0.97	0.87	0.94	0.88	1.09	1.25
IL1RA	1.21	1.09	1.00	0.80	1.10	1.12
IL2	1.15	1.09	1.17	0.91	1.11	1.28
IL20	1.05	1.03	0.99	0.93	1.00	0.96
IL21	1.06	1.09	1.10	1.03	0.98	1.00
IL22	1.11	1.09	1.08	0.83	0.94	0.95
IL23	1.01	1.00	1.04	1.04	1.06	0.88
IL28A / IFNL2	1.00	0.97	1.02	0.93	0.93	0.91
IL3	1.11	1.15	1.00	0.86	1.16	1.25
IL33 / NFHEV (MATURE)	1.12	1.07	1.03	0.94	1.07	1.01
IL4	0.99	0.98	1.09	0.80	1.19	1.17
IL5	1.02	1.07	1.08	0.88	1.17	1.24
IL6	2.26	2.05	1.09	0.87	0.95	1.03
IL7	1.20	1.18	1.22	0.72	1.07	1.06
IL8 / CXCL8	3.94	6.61	1.35	1.71	2.08	1.70
IL9	1.17	1.10	1.07	0.99	0.99	1.07
IP10 / CXCL10	1.59	0.54	0.66	0.86	0.96	1.03
LEPTIN	1.01	1.05	0.95	1.41	1.18	1.17
LIF	1.17	1.24	1.14	1.06	1.12	0.98
MCP1 / CCL2	1.44	1.20	1.17	1.02	1.02	1.01
MCP2 / CCL8	1.09	1.00	1.06	0.95	0.96	1.09
MCP3 / CCL7	4.40	1.84	1.45	0.85	1.07	1.35
MCP4 / CCL13	1.05	1.07	1.06	1.00	1.07	1.07
MDC / CCL22	0.99	0.81	0.97	0.91	1.27	1.36
MIF	3.25	3.76	3.77	1.75	1.58	1.73
MIG / CXCL9	0.97	0.98	1.07	1.09	1.10	1.10
MIP1A / CCL3	2.03	1.64	1.24	0.88	1.05	1.18
MIP1B / CCL4	1.10	1.09	1.04	0.97	1.11	1.19
MIP1D / MIP5 / CCL15	0.88	0.90	0.82	0.92	0.93	0.95
PAI1 / SERPINE	1.21	1.56	0.65	1.13	1.37	1.13

	enteric neurons			other peripheral neurons		
	cisplatin	carboplatin	oxaliplatin	cisplatin	carboplatin	oxaliplatin
PDGFAA	0.91	1.16	0.61	0.95	0.82	0.62
PDGFAB / BB	1.02	1.03	1.07	0.98	1.20	1.27
RANTES / CCL5	1.06	0.85	0.85	0.97	1.35	1.56
RESISTIN	1.01	0.97	0.91	1.18	1.12	1.08
SCD40L	1.02	0.89	0.98	0.86	1.30	1.37
SCF	0.88	1.01	0.86	1.09	1.26	1.19
SDF1A+B / CXCL12	0.46	0.41	0.52	1.22	1.17	1.20
SFAS / TNFRSF6	1.84	3.59	1.22	2.29	3.66	1.93
SICAM1	1.35	1.46	1.10	1.21	1.14	1.07
SVCAM1	0.81	0.42	0.55	0.86	0.84	1.01
TARC / CCL17	1.15	1.06	1.11	0.93	0.81	0.98
TGFA	4.29	4.68	3.81	1.15	1.58	1.43
TNFA	0.80	0.94	0.70	0.85	1.13	1.17
TNFB / LYMPHOTOXIN A (LTA)	1.12	1.00	1.21	0.83	1.30	1.51
TPO	1.04	1.12	1.06	1.12	1.09	1.15
TRAIL / TNFSF10	1.05	1.04	1.08	1.08	1.07	1.07
TSLP	1.06	0.99	1.03	1.04	0.95	0.93
VEGF	0.66	0.83	0.62	1.05	1.16	1.23

Table 2.5 List of predicted drug targets using compound-protein interaction analysis

Target	Enrichment	Fisher p-value	False Discovery Rate
EBPL	4.79	0.036	0.001
ROCK2	3.59	0.016	0.046
ROCK1	3.43	0.036	0.064
IRAK4	2.75	0.036	0.132
HRH3	2.48	0.039	0.184
DRD3	2.41	0.036	0.210
EBP	-3.26	0.004	0.143
EDNRB	-3.34	0.026	0.121
SCN3A	-3.94	0.049	0.027
CYSLTR2	-4.60	0.040	0.002

Table 2.6 List of predicted targets for experimentally validated hit compounds

Target	Compound
GLRA1	mefloquine HCl
SLC6A2	mefloquine HCl
SLC6A3	mefloquine HCl
FFAR2	mitotane
SCN4A	mitotane
ABHD11	oxybutynin
CHRM1	oxybutynin
CHRM2	oxybutynin
CHRM3	oxybutynin
CHRM4	oxybutynin
CHRM5	oxybutynin

Table 2.7 List of transcripts and functional categories in excitotoxicity transcriptional program

TRPMs	RYRs	CHRM3/5	PLCs	IP3Rs	PKCs
TRPM1	RYR1	CHRM3	PLCB1	ITPR1	PRKCA
TRPM3	RYR2	CHRM5	PLCB2	ITPR2	PRKCB
TRPM6	RYR3		PLCB3	ITPR3	PRKCG
TRPM7			PLCB4		PRKCD
TRPM2			PLCG1		PRKCE
TRPM4			PLCG2		PRKCH
TRPM5			PLCD1		PRKCQ
TRPM8			PLCD3		PRKCI
			PLCD4		PRKCZ
			PLCE1		PRKD1
			PLCH1		PRKD2
			PLCH2		PRKD3
			PLCZ1		PKN1
			PLCL1		PKN2
			PLCL2		PKN3

Table 2.8 List of quality control metric cutoffs for the snRNAseq dataset

Dataset	nFeatures Greater Than	nFeatures Less Than	nCounts Less Than	Percent Mitochondrial Reads Less Than
Vehicle_1	1700	7400	N/A	5
Vehicle_2	1750	7400	N/A	5
OXL_1	1650	7700	N/A	5
OXL_2	1750	7600	N/A	5
OXL_OXY_1	1500	7400	N/A	5
OXL_OXY_2	2500	7100	N/A	5
Enteric Neuron Subset	N/A	4600	15000	N/A

Table 2.9 Principal components used for SNN and UMAP calculation and the resolution used for clustering of each dataset

Dataset	Principal Components	Clustering Resolution
Vehicle_1	21	0.1
Vehicle_2	21	0.1
OXL_1	20	0.1
OXL_2	21	0.1
OXL_OXY_1	20	0.1
OXL_OXY_2	22	0.1
Vehicle-Treated Cells	20	0.1
OXL-Treated Cells	20	0.1
OXL_OXY-Treated Cells	19	0.1
All Cells	30	0.1
Vehicle_1 Enteric Neurons	20	0.5
Vehicle_2 Enteric Neurons	23	0.5
OXL_1 Enteric Neurons	20	0.5
OXL_2 Enteric Neurons	24	0.5
OXL_OXY_1 Enteric Neurons	22	0.5
OXL_OXY_2 Enteric Neurons	20	0.5
Vehicle-Treated Enteric Neurons	27	0.5
OXL-Treated Enteric Neurons	26	0.5
OXL_OXY-Treated Enteric Neurons	27	0.5
All Enteric Neurons	30	0.6

Table 2.10 List of transcripts used to define neurochemical identities

Neurochemical Identity	Transcripts
Cholinergic	CHAT, SLC18A3, SLC5A7
Nitroergic	NOS1
GABAergic	GAD1, GAD2, SLC32A1
Glutamatergic	GLUL, SLC17A6, SLC17A8
Serotonergic	TPH1, TPH2, DDC, SLC18A2
Catecholaminergic	TH, DBH, DDC, SLC18A2
Calcitonin 2 (CGRP)	CALCB
CART Prepropeptide	CARTPT
Cerebellin 2	CBLN2
Cholecystokinin	CCK
Chromogranin A	CHGA
Endothelin 3	EDN3
Galanin	GAL
Neuromedin U	NMU
Neuropeptide Y	NPY
Neurexophilin 2	NXPH2
Proenkephalin	PENK
Secretogranin	SCG3
Somatostatin	SST
Substance P	TAC1
Urocortin	UCN

Table 2.11 List of antibodies

Antibody Name	Purpose	Vendor	Part Number	Dilution
γH2AX	immunofluorescence staining	Sigma-Aldrich	05-636	1:500
TUBB3	immunofluorescence staining (rabbit)	BioLegend	802001	1:2000
cleaved caspase 3	immunofluorescence staining and flow cytometry	Cell Signaling	9661	1:800
NOS1	flow cytometry	Santa Cruz Biotechnology	sc-5302	1:100
GABA	flow cytometry	Sigma-Aldrich	A0310	1:25
CHAT	flow cytometry	Sigma-Aldrich	AB144P	1:100
serotonin (5-HT)	flow cytometry	ImmunoStar	20079	1:1250
TUBB3	immunofluorescence staining	Sigma-Aldrich	AB9354	1:400
TUBB3	primary human staining and flow cytometry	Sigma-Aldrich	AB9354	1:200
p-PKC	immunofluorescence staining	Sigma-Aldrich	SAB4504099	1:500
CHRM3	Western blot	Novus Biologicals	NBP2-19444	1:500
CHRM5	Western blot	abbexa	abx004108	1:1000
beta actin	Western blot	GenScript	A00702	1:5000
TUBB3	primary human staining	Sigma-Aldrich	AB9354	1:400
p-PKC	primary human staining	Sigma-Aldrich	SAB4504099	1:400
NOS1	primary human staining	Santa Cruz Biotechnology	sc-5302	1:50
NOS1	primary human and mouse staining	Thermo Fisher	61-70000	1:200
CHAT	primary human and mouse staining	Sigma-Aldrich	AB144P	1:400
HuC/D	primary human and mouse staining	Invitrogen	A-21271	1:100

2.7 Methods

Experimental Models Details

Human pluripotent stem cell lines. Human embryonic stem cell line H9 (WAe009-A, and derivatives *CHRM3* gRNA, *CHRM5* gRNA, cas9) and induced pluripotent stem cell line WTC-11 (UCSFi001-A) were plated on geltrex-coated plates and maintained in chemically-defined medium (E8) as described previously³². The maintenance cultures were tested for mycoplasma every 30 days.

Cancer cell lines. Colorectal cancer cell lines SW480 and WiDr were plated on geltrex-coated plates and maintained in chemically-defined mediums. SW480 was cultured in McCoy's 5A medium (Corning, 10-050-CV) supplemented with 10% FBS, 0.5 mg/mL normocin (InvivoGen, ant-nr-2), and 1mM sodium pyruvate (Corning, 25-000-CI). WiDr was cultured in EMEM (VWR, 12-611F) supplemented with 0.5 mg/mL normocin (InvivoGen, ant-nr-2). Cultures were tested for mycoplasma every 30 days.

Mouse line. – Male wild type C57BL/6J mice ages 8-12 weeks old (n = 40) were purchased from Jackson Laboratory. <https://www.jax.org/strain/000664>

UCSF Research Data Browser Analysis

The UCSF Research Data Browser was utilized to identify and extract patients diagnosed with colorectal cancer (ICD-10-CM-C78.5) for the oxaliplatin analysis or ovarian cancer (ICD-10-CM-C56) for the carboplatin analysis. Patients diagnosed with constipation prior to their cancer diagnosis were excluded from both analyses, based on the ICD10 name “constipation”, to limit confounding factors. In each analysis, patients in the platin

chemotherapy treated groups were then matched to their corresponding untreated groups by age, sex, and race/ethnicity. Patients were then further subset into four groups based on whether they were prescribed the relevant platin chemotherapy (based on the drug name (oxaliplatin or carboplatin)) and whether they were diagnosed with constipation (based on the ICD10 name “constipation”). Data represents the odds ratio (OR) and 95% confidence intervals for each drug calculated by Fisher’s exact statistical testing. p-values were calculated by Chi-squared statistical testing.

Differentiation and Characterization of Enteric Neurons

Enteric neural crest induction. Once the hPSCs reached 70-80% confluency, the 12-day enteric neural crest induction protocol was initiated according to our group’s established induction protocol³². Briefly, on day 0, the maintenance medium (E8) was aspirated and replaced with neural crest induction medium A [BMP4 (1 ng/mL), SB431542 (10 μ M), and CHIR 99021 (600 nM) in Essential 6 medium]. Subsequently, on enteric neural crest induction days 2 and 4, the cells were fed with neural crest induction medium B [SB431542 (10 μ M) and CHIR 99021 (1.5 μ M) in Essential 6 medium] and on days 6, 8, and 10 the cells were fed with neural crest induction medium C [medium B with retinoic acid (1 μ M)]. Next, enteric neural crestospheres were formed during days 12-15 in NC-C medium [FGF2 (10 ng/mL), CHIR 99021 (3 μ M), N2 supplement (10 μ L/mL), B27 supplement (20 μ L/mL), glutagro (10 μ L/mL), and MEM NEAAs (10 μ L/mL) in neurobasal medium] following dissociation with Accutase. NC-C medium was refreshed on day 14 prior to enteric neuron induction phase on day 15.

Enteric neuron induction from enteric neural crest. On day 15 of the protocol, enteric neuron induction was initiated according to our group's established induction protocol^{32,33}. From day 15 onward, cells were cultured in ENC medium [GDNF (10 ng/mL), ascorbic acid (100 μ M), N2 supplement (10 μ L/mL), B27 supplement (20 μ L/mL), glutagro (10 μ L/mL), and MEM NEAAs (10 μ L/mL) in neurobasal medium] to promote the enteric neuron identity, with feeding occurring every two to three days. Enteric neuron progenitors (days 15-28) were dissociated with Accustase for 30 minutes at 37°C, 5% CO₂ and plated on poly-L-ornithine/laminin/fibronectin plates at 300,000 viable cells/cm² in ENC medium and continued to be fed every two to three days until D30, after which, feeding frequency could be reduced to once or twice per week with larger volumes of feeding medium. All experiments were performed on stage 1 enteric neurons (days 35-50)³⁰.

Differentiation and Characterization of Control Peripheral Neurons

Cranial neural crest induction. Once the hPSCs reached 70-80% confluency, a previously established 12-day cranial neural crest induction protocol was initiated according to our group's established induction protocol⁵⁹. Briefly, on day 0, the maintenance medium (E8) was aspirated and replaced with neural crest induction medium A [BMP4 (1 ng/mL), SB431542 (10 μ M), and CHIR 99021 (600 nM) in Essential 6 medium]. Subsequently, cells were fed with neural crest induction medium B [SB431542 (10 μ M) and CHIR 99021 (1.5 μ M) in Essential 6 medium] on days 2, 4, 6, 8, and 10. Next, cranial neural crest crestospheres were formed during days 12-15 in NC-C medium [FGF2 (10 ng/mL), CHIR 99021 (3 μ M), N2 supplement (10 μ L/mL), B27 supplement (20 μ L/mL), glutagro (10 μ L/mL), and MEM NEAAs (10 μ L/mL) in neurobasal medium] following dissociation with

Accutase (Stemcell Technologies, 07922). NC-C medium was refreshed on day 14 prior to the induction of cranial neural crest derived peripheral neurons on day 15.

Induction of cranial neural crest-derived peripheral neurons. On day 15, cranial neural crest-derived peripheral neuron induction was initiated according to our group's established induction protocol^{43,59}. From day 15 onward, cells were cultured in ENC medium [GDNF (10 ng/mL), ascorbic acid (100 μ M), N2 supplement (10 μ L/mL), B27 supplement (20 μ L/mL), glutagro (10 μ L/mL), and MEM NEAAs (10 μ L/mL) in neurobasal medium] to promote the cranial neuron identities, with feeding occurring every two to three days. Cranial neural crest-derived neuron progenitors (days 15-28) were dissociated with Accutase (Stemcell Technologies, 07922) for 30 minutes 37°C, 5% CO₂ and plated on poly-L-ornithine/laminin/fibronectin plates at 300,000 viable cells/cm² in ENC medium and continued to be fed every two to three days until D30, after which, feeding frequency could be reduced to once or twice per week with larger volumes of feeding medium. All experiments were performed on cranial neural crest-derived neurons between D35 and D50.

Immunofluorescence Staining of hPSC-derived Neurons

Cells were fixed in 4% paraformaldehyde (Santa Cruz, sc-281692) in PBS for 30 minutes at room temperature, and then blocked and permeabilized in eBioscience Foxp3/Transcription Factor Staining Buffer Set permeabilization buffer (Invitrogen, 00-5523) for another 30 minutes at room temperature. After fixation and permeabilization, cells were incubated in primary antibody solution diluted in permeabilization buffer overnight at 4°C, and then washed three times with permeabilization buffer before their

incubation with fluorophore-conjugated secondary antibodies diluted in permeabilization buffer for one hour at room temperature. Before imaging, stained cells were incubated with DAPI fluorescent nuclear stain diluted in PBS and washed an additional two times with PBS. The list of antibodies and working dilutions is provided in Table 2.11. Unless otherwise specified, cells were imaged on a digital inverted fluorescence microscope with a 20x objective and images were processed using Adobe Photoshop software.

Preparation of Platins for *In Vitro* Experiments

Platins were prepared fresh for each experiment. Briefly, a stock solution of each platin was prepared by dissolving each compound in sterile water by vortexing vigorously. Stock solutions were 1 mM for cisplatin (Sigma-Aldrich, C2210000) and oxaliplatin (Sigma-Aldrich, Y0000271) and 10 mM for carboplatin (Sigma-Aldrich, C2538). Once in solution, each drug stock was diluted in cell culture medium to the designated concentration needed per experiment. The stock solutions were disposed of within 24 hours of preparation.

Lactate Dehydrogenase Activity Assay

To compare the cytotoxic response of the enteric neurons and control peripheral neurons to the platins, cells were assayed for lactate dehydrogenase activity using CytoTox 96 cytotoxicity assay kit (Promega, G1780). Briefly, the cells are plated in 96 well plates. The supernatant and the cell lysate are harvested three days later and assayed for lactate dehydrogenase activity using a plate reader (490 nm absorbance). Cytotoxicity is calculated by dividing the lactate dehydrogenase signal of the supernatant by the total

lactate dehydrogenase signal (from lysate plus supernatant). Data were collected from nine independent differentiations. Statistical analysis was performed by two-way ANOVA with Šidák correction for multiple comparisons.

Bulk RNA Sequencing Analysis

Sample preparation and sequencing. hPSC-derived enteric neurons and control peripheral neurons were treated with 50 μ M oxaliplatin or vehicle (medium containing 5% water) for three days. Samples were prepared in duplicate, from two independent differentiations, per condition according to the QuantSeq 3' mRNA-Seq Library Prep Kit FWD for Illumina (Lexogen). Libraries were sequenced on HiSeq 4000 at the UCSF Center for Advanced Technology.

Pre-ranked gene set enrichment analysis. Reads were aligned to the human genome (build hg38) using STAR (v2.7.1a). FeatureCounts (v1.6.2) were then used to count reads assigned to gene features, as annotated in Illumina's iGenome hg38 GTF (2015). Gene level counts were then assessed for differential expression analysis with DESeq2 (v1.20) in the R (v3.5.1) environment. Briefly, the DESeq function was used with default options for each comparison: oxaliplatin-treated control peripheral neurons vs vehicle-treated control peripheral neurons, oxaliplatin-treated enteric neurons vs vehicle-treated enteric neurons, and oxaliplatin-treated enteric neurons vs oxaliplatin-treated control peripheral neurons. The differentially expressed genes were sorted in descending order by the \log_2 fold-change in gene expression for each comparison. Then pre-ranked GSEA was performed using GSEA version 4.3.2 and the MSigDB Hallmark and Ontology gene sets version 2022.1 to identify gene sets significantly changed between

the two populations based on a p-value cutoff of < 0.05 and a false discovery rate of < 0.25 .

Cytokine ELISA

Sample preparation. hPSC-derived enteric neurons and hPSC-derived control peripheral neurons cultured in 24-well plates were treated with 20 μM cisplatin, 200 μM carboplatin, 40 μM oxaliplatin, or vehicle (medium containing 4% water) for three days. Three biological replicates per treatment condition were included, for a total of 24 samples. Cell culture supernatants were transferred to 1.5 mL tubes and centrifuged at 4°C and 10,000g for 10 minutes. Each supernatant was transferred to fresh 1.5 mL tubes, frozen at -80°C, and shipped overnight on dry ice to the Human Immune Monitoring Center at Stanford University.

Luminex assay. This assay was performed by the Human Immune Monitoring Center at Stanford University-Immunoassay Team. Kits were purchased from EMD Millipore Corporation, Burlington, MA., and run according to the manufacturer's recommendations with modifications described as follows. H76 kits include 3 panels: Panel 1 is Milliplex HCYTMAG-60K-PX41 with addition of IL-18 and IL-22. Panel 2 is Milliplex HCP2MAG-62K-PX23 with addition of MIG. Panel 3 includes the Milliplex HSP1MAG-63K-06 and HADCYMAG-61K-03 (Resistin, Leptin and HGF) to generate a 9 plex. Samples were diluted 3-fold (Panels 1 and 2) and 10-fold for Panel 3. An aliquot (25 μL) of the diluted sample was mixed with antibody-linked magnetic beads in a 96-well plate and incubated overnight at 4°C with shaking. Cold and room temperature incubation steps were performed on an orbital shaker at 500-600 rpm. Plates were washed twice with wash

buffer in a BioTek ELx405 washer (BioTek Instruments). Following one-hour incubation at room temperature with biotinylated detection antibody, streptavidin-PE was added for 30 minutes with shaking. Plates were washed as described above and PBS added to wells for reading in the Luminex FlexMap3D Instrument with a lower bound of 50 beads per sample per cytokine. Each sample was measured in duplicate. Custom Assay Chex control beads were purchased and added to all wells (Radix BioSolutions). Wells with a bead count <50 were flagged, and data with a bead count <20 were excluded.

Report and data analysis. The output CSV file was used to extract the median fluorescence intensities for each cytokine. The median fluorescence intensities per sample were averaged. Then the average median fluorescence intensities for each biological replicate were normalized to the average of each population's vehicle treatment condition. The average of the three biological replicates for each cytokine are represented in the heatmaps. Statistical analysis was performed by two-way ANOVA with Dunnett correction for multiple comparisons.

Viability Assay

To compare the cell viability of the enteric neurons treated with the platins with and without a variety of chemical modulators, cells were assayed for ATP levels using CellTiter-Glo Luminescent Cell Viability assay kit (Promega, G7571). Briefly, cells were plated in 96 well plates and treated with the experiment treatment conditions, specified below, for three days and then assayed for ATP levels using a plate reader, detecting luminescence with a 500 ns integration time. The ATP levels per well were then normalized to the average value of the vehicle wells to determine the normalized cell viability.

Platin cell viability experiment. Cells were treated with cisplatin at 1.25, 2.5, 5, and 10 μM concentrations, carboplatin at 20, 40, 80, and 100 μM , and oxaliplatin at 2.5, 5, 10 and 20 μM concentrations. Controls included 20 μM lomustine, 10 μM CCCP, and vehicle containing medium with 2% water. Data represents the mean \pm SEM from six individually treated wells per condition. Statistical analysis was performed by two-way ANOVA with Dunnett correction for multiple comparisons.

High-throughput phenotypic screen compound validation experiment. Oxaliplatin was dosed at 40 μM . Each compound (mefloquine, mitotane, and oxybutynin) was dosed at 1 and 10 μM concentrations. Vehicle contained medium with 4% water. Each dot represents an individually treated well. Statistical analysis was performed by one-way ANOVA with Tukey correction for multiple comparisons.

G_q protein experiment. Oxaliplatin was dosed at 20 μM . YM-24489 was dosed at 2.5, 5, and 10 μM concentrations. Vehicle contained medium with 2% water. Each dot represents an individually treated well. Statistical analysis was performed by one-way ANOVA with Tukey correction for multiple comparisons.

G_i protein experiment. Oxaliplatin was dosed at 20 μM . Pertussis toxin was dosed at 0.01, 0.1, and 0.5 $\mu\text{g/mL}$ concentrations. Vehicle contained medium with 2% water. Each dot represents an individually treated well. Statistical analysis was performed by one-way ANOVA with Tukey correction for multiple comparisons.

Phospholipase C experiment. Oxaliplatin was dosed at 20 μM . U 73122 was dosed at 2.5, 5, and 10 μM concentrations. Vehicle contained medium 2% water. Each dot represents an individually treated well. Statistical analysis was performed by one-way ANOVA with Tukey correction for multiple comparisons.

IP3 receptor experiment. Oxaliplatin was dosed at 20 μM . Lanthanum(III) was dosed at 100, 200, and 400 μM concentrations. Vehicle contained medium with 2% water. Each dot represents an individually treated well. Statistical analysis was performed by one-way ANOVA with Tukey correction for multiple comparisons.

Protein kinase C experiment. Oxaliplatin was dosed at 20 μM . Go 6983 was dosed at 0.1, 1, and 10 μM concentrations. Vehicle contained medium with 2% water. Each dot represents an individually treated well. Statistical analysis was performed by one-way ANOVA with Tukey correction for multiple comparisons.

γH2AX Imaging and Analysis

Cells were plated in 24 well plates and treated with 5 and 10 μM cisplatin, 50 and 100 μM carboplatin, 10 and 20 μM oxaliplatin, or vehicle containing medium with 2% water for three days. Cells were fixed and stained with γH2AX and TUBB3 antibodies and DAPI, as described previously. High-throughput imaging was carried out using the In Cell Analyzer 2000 with a 20X objective (GE Healthcare). Neuronal γH2AX signal was detected based on the overlap of γH2AX with TUBB3. The total number of neuronal γH2AX pixels were normalized by the total cell number within each well as measured by DAPI staining with the GE Developer Toolbox v1.9.1. The quantification per well was then normalized to the average value of the vehicle wells. Each dot represents an individually treated well. Statistical analysis was performed by one-way ANOVA with Dunnett correction for multiple comparisons. Representative images were taken on the EVOS™ FL digital inverted fluorescence microscope (Invitrogen).

mitoSOX Imaging and Analysis

Cells were plated in 24 well plates and treated with 5 and 10 μM cisplatin, 50 and 100 μM carboplatin, 10 and 20 μM oxaliplatin, or vehicle containing medium with 2% water for three days. Cells were incubated in 5 μM mitoSOX reagent (Invitrogen, M36008) for 10 minutes at 37°C, then fixed and stained with TUBB3 and DAPI, as described previously. High-throughput imaging was carried out using the In Cell Analyzer 2000 with a 20X objective (GE Healthcare). Neuronal mitoSOX signal was detected based on the overlap of mitoSOX with TUBB3. The total number of neuronal mitoSOX pixels were normalized by the total cell number within each well as measured by DAPI staining with the GE Developer Toolbox v1.9.1. The quantification per well was then normalized to the average value of the vehicle wells. Each dot represents an individually treated well. Statistical analysis was performed by one-way ANOVA with Dunnett correction for multiple comparisons. Representative images were taken on the EVOS™ FL digital inverted fluorescence microscope (Invitrogen).

Neurite Length Imaging and Analysis

Cells were plated in 24 well plates and treated with 5 and 10 μM cisplatin, 50 and 100 μM carboplatin, 10 and 20 μM oxaliplatin, or vehicle containing medium with 2% water for three days. Cells were stained with TUBB3 and DAPI, as described previously. High-throughput imaging was carried out using the In Cell Analyzer 2000 with a 20x objective (GE Healthcare). Images were batch processed through an imaging processing software, MIPAR Image Analysis, with a custom-built algorithm to analyze measurements for chemotherapy-induced neurite degeneration, which has been published previously^{23,24}.

Briefly, the algorithm generates optimized grayscale images by reducing overall noise and minimizing the amount of nonspecific staining to identify and quantify the neurite networks within each field-of-view image. A subsequent segmentation algorithm was performed to identify and quantify nuclei within each field-of-view image. After processing, each image yielded measurements of total neurite length and cell number. The total length of neurites per well were normalized by the total cell number per well. Each dot represents an individually treated well. Statistical analysis was performed by one-way ANOVA with Dunnett correction for multiple comparisons. The quantification per well was then normalized to the average value of the vehicle wells.

Flow cytometry

Cells were dissociated into single cell suspensions by Accutase treatment (Stemcell Technologies, 07922) for 30-60 min, 37°C, 5% CO₂ and then fixed and permeabilized using the eBioscience Fcγ3/Transcription Factor Staining Buffer Set (Invitrogen, 00-5523). Cells were stained with primary and secondary antibodies as described previously for immunofluorescence. Flow cytometry was conducted using a flow cytometer and data was analyzed using FlowJo™ (FlowJo™ Software Version 8.7). The list of antibodies and working dilutions is provided in Table 2.11.

Cleaved Caspase 3 Detection and Analysis

Flow cytometry. Cells were plated in either 96 well or 24 well plates and treated with the experiment treatment conditions, specified below, for three days. Cells were stained with cleaved caspase 3 and TUBB3 antibodies and flow cytometry was performed, as

described above. In Flowjo™, neurons were detected by gating on the TUBB3+ cells. Then, within the TUBB3+ population, the percentage of neurons positive for cleaved caspase 3 was detected and reported.

Platin apoptosis experiment. Cisplatin was dosed at 5 and 10 μM . Carboplatin was dosed at 50 and 100 μM . Oxaliplatin was dosed at 10 and 20 μM . The vehicle condition contained medium with 2% water. Each dot represents an individually treated well. Statistical analysis was performed by one-way ANOVA with Dunnett correction for multiple comparisons.

Muscarinic cholinergic receptor agonist/antagonist experiment. Oxaliplatin was dosed at 20 μM . Pilocarpine and solifenacin were dosed at 5 μM . The vehicle condition contained medium with 2% water. Each dot represents an individually treated well. Statistical analysis was performed by one-way ANOVA with Dunnett correction for multiple comparisons.

CHRM3 and CHRM5 CRISPR RNP experiment. Oxaliplatin was dosed at 10 μM . Oxybutynin was dosed at 5 μM . The vehicle condition contained medium with 1% water. All targeted cell lines were treated, fixed, and stained for flow cytometry on the same days. Each dot represents an individually treated well. Statistical analysis was performed by two-way ANOVA with Tukey correction for multiple comparisons.

Four enteric neurotransmitter identities experiment. Oxaliplatin was dosed at 20 μM and the vehicle condition contained medium with 2% water. Each cleaved caspase 3 and TUBB3 antibody panel included one of four enteric neurotransmitter markers: NOS1, GABA, CHAT, and 5-HT. The list of antibodies and working dilutions is provided in Table

2.11. Each dot represents an individually treated well. Statistical analysis was performed by two-way ANOVA with Šidák correction for multiple comparisons.

Imaging. Cells were plated in 96 well plates and treated with 10 μM oxaliplatin with or without oxybutynin dosed at 0.1, 1 and 5 μM , or vehicle containing medium with 1% water for two days. Cells were stained with cleaved caspase 3 and TUBB3 antibodies and stained with DAPI, as described previously. High-throughput imaging was carried out using the ImageXpress Confocal HT.ai (Molecular Devices). MetaXpress High-Content Image Acquisition and Analysis Software. Representative images were taken on the Revolve digital fluorescence microscope (ECHO). Each dot represents an individually treated well. Statistical analysis was performed by one-way ANOVA with Tukey correction for multiple comparisons.

High-Throughput Phenotypic Drug Screen

Cells were plated in 384 well plates and treated with 40 μM oxaliplatin and compounds from an FDA-approved chemical library (Selleckchem, USA) at 1 μM . Three days after treatment, cells were stained with DAPI prior to fixation. Cells were then promptly fixed, as described previously, and stained with propidium iodide. High-throughput imaging was carried out using the In Cell Analyzer 2000 (GE Healthcare). Cell viability was quantified by using the propidium iodide signal to count the total number of cells per well and using the DAPI signal to count the total number of dead cells per well in the GE Developer Toolbox v1.9.1. Cell viability z-scores were calculated for each drug by subtracting the mean of the library from the drug and dividing that by the standard deviation of the library. This experiment was performed in two biological replicates, in ESC-derived enteric

neurons and iPSC-derived enteric neurons. The top 30 drugs with the highest cell viability z-scores from each biological replicate were defined as hits from the screen.

Colorectal Cancer Viability Imaging and Analysis

One day after passaging, cancer cells were treated with 20 μM cisplatin, 200 μM carboplatin, and 20 μM oxaliplatin and mefloquine, mitotane, and oxybutynin at 1, 4, 7, and 10 μM concentrations. Three days after treatment, cells were stained with DAPI prior to fixation. Cells were then promptly fixed, as described previously, and stained with propidium iodide. High-throughput imaging was carried out using the In Cell Analyzer 2000 (GE Healthcare). Cell viability was quantified by using the propidium iodide signal to count the total number of cells per well and using the DAPI signal to count the total number of dead cells per well in the GE Developer Toolbox v1.9.1. Each dot represents an individually treated well. Statistical analysis was performed by one-way ANOVA with Dunnett correction for multiple comparisons.

Drug-Protein Interaction Pipeline

For this analysis, we used our previously published drug-protein interaction analysis pipeline to predict drug targets enriched in the compounds that either increase or decrease oxaliplatin-treated enteric neuron viability⁶. Briefly, isomeric SMILES for each drug in the library were acquired from Selleckchem and used to run a SEA library search. The SEA predicted targets were filtered, selecting human targets and predicted interaction p -values < 0.05 , which yielded 2150 predicted proteins targeted by the drug library. Weighted combined z-scores were then calculated for each gene by combining z-

scores across all treatments. The p -values were then calculated based on the combined z-scores and adjusted using $p.adjust$ (method = FDR). As an orthogonal approach for each gene, we recorded the number of treatments with negative or positive z-scores as well as the total number of compounds predicted to target that gene. Using the sum of counts for all other genes and drugs, we performed a Fisher's exact test to evaluate the degree to which z-scores were enriched among the treatments that either increase or decrease oxaliplatin-treated enteric neuron viability. A false discovery rate < 0.25 and Fisher's p -value < 0.05 was used to identify the proteins significantly associated with a high or low viability z-score.

Protein-Protein Interaction Network Analysis

Protein-protein interaction network analysis was performed using the Search Tool for the Retrieval of Interacting Genes (STRING) database version 11.0. The minimum required interaction score was set to 0.7, corresponding to high confidence with data support from the following active interaction sources: textmining, experiments, databases, co-expression, neighborhood, gene fusion, and co-occurrence.

Microelectrode Array Analysis

Data acquisition. Cells were plated on Cytoview MEA 6-well plates and treated with 10 μ M oxaliplatin or vehicle containing medium with 1% water. For the experiment including oxybutynin, enteric neurons were treated with 10 μ M oxaliplatin, 5 μ M oxybutynin, 10 μ M oxaliplatin and 5 μ M oxybutynin co-treatment, or vehicle containing medium with 1%

water. After three hours, enteric neuron activity was recorded with the Axion Maestro Edge for 1 hour.

Data processing. Raw data were first spike sorted with a modified version of SpikeInterface (<https://github.com/SpikeInterface>) using MountainSort to identify high quality units by manually scoring based on amplitude, waveform shape, firing rate, and inter-spike interval contamination. Units with firing rates greater than 0.1 Hz were included in the analysis. Each dot represents an individual unit identified from spike sorting that passed scoring. Statistical analysis was performed by Welch's t test for the experiment comparing oxaliplatin to vehicle and Brown-Forsythe and Welch ANOVA with Dunnett correction for multiple comparisons for the experiment including oxybutynin.

TUNEL Imaging and Analysis

TUNEL staining was performed using the In Situ Cell Death Detection Kit, TMR Red kit (Roche, 12156792910). Briefly, cells were plated in 96 well plates and treated with 10 μ M oxaliplatin with or without oxybutynin dosed at 0.1, 1 and 5 μ M, or vehicle containing medium with 1% water for three days. Cells were stained with TUBB3, as described previously, then stained with TUNEL enzyme solution diluted 10-fold in label solution by incubating each well in 50 μ L of the diluted enzyme solution for sixty minutes at 37°C. Cells were washed twice with PBS then stained with DAPI as described previously. High-throughput imaging was carried out using the ImageXpress Confocal HT.ai (Molecular Devices). Neuronal TUNEL signal was detected based on the overlap of TUNEL with TUBB3. Neuronal TUNEL intensity was normalized by the total cell number within each well as measured by DAPI staining with the MetaXpress High-Content Image Acquisition

and Analysis Software. Each dot represents an individually treated well. Statistical analysis was performed by one-way ANOVA with Tukey correction for multiple comparisons.

Phosphorylated Protein Kinase C (p-PKC) Imaging and Analysis

Cells were plated in 96 well plates and treated with 10 μ M oxaliplatin with or without oxybutynin dosed at 5 μ M, or vehicle containing medium with 1% water for three days. Cells were stained with p-PKC and TUBB3 antibodies then stained with DAPI as described previously. High-throughput imaging was carried out using the ImageXpress Confocal HT.ai (Molecular Devices). Neuronal p-PKC signal was detected based on the overlap of p-PKC with TUBB3. Neuronal p-PKC intensity was normalized by the total cell number within each well as measured by DAPI staining with the MetaXpress High-Content Image Acquisition and Analysis Software. Each dot represents an individually treated well. Statistical analysis was performed by one-way ANOVA with Holm-Šidák correction for multiple comparisons. The distribution of neuronal p-PKC intensity per cell was also visualized by binning \log_{10} transformed intensity values across 512 equally sized bins between the minimum and maximum intensity value among all treatment condition wells. Distributions were scaled per well. Distribution plots were generated using ggplot2 (v3.4). The solid line represents the average distribution of all wells from the same treatment condition with the standard deviation shown by the transparent ribbon. Statistical analysis was performed by nested t-tests comparing the following conditions: vehicle vs oxaliplatin and oxaliplatin vs oxaliplatin + oxybutynin. Representative images

were taken on the Revolve digital fluorescence microscope (ECHO) and processed using Fiji (ImageJ) software.

***CHRM3* and *CHRM5* CRISPR Ribonucleoprotein (RNP) Targeting**

Targeting. *CHRM3* and *CHRM5* ribonucleoprotein (RNP) complexes were assembled by mixing 16 pmol of multi-guide sgRNA (Synthego) and 12 pmol of Cas9 2NLS (Synthego) in lipofectamine CRISPRMAX Cas9 transfection reagent (Invitrogen, CMAX00001) per reaction. H9 ESCs were lipofected with the RNP-transfection solutions then replated after two days in 10 cm dishes at 1500 cells/cm². After a few days, individual colonies were picked and plated into individual wells of a 24 well plate. After a few more days, the clones were frozen at -80°C in STEM-CELLBANKER DMSO FREE (Amsbio LCC, 13926) and stored long-term in liquid nitrogen.

Protein extraction. hPSC-derived enteric neurons were lysed in RIPA lysis buffer (Millipore, 20-188) with protease/phosphatase inhibitor (Roche, 4693159001) at 4°C for 30 minutes while rocking. Lysate was centrifuged at 13,800 g for 20 minutes at 4°C. Supernatants were transferred to fresh tubes and stored long-term at -80°C.

Protein quantification. Bovine serum albumin (BSA, Sigma-Aldrich, A4503) was diluted to 1, 0.8, 0.6, 0.4, 0.2, 0.1, and 0.05 mg/mL with water. Lysates were diluted 1:1, 1:10, and 1:100 in water. Lysates and BSA samples were added to Bio-Rad Protein Assay Dye Reagent Concentrate (Bio-Rad Laboratories, 5000006) and incubated for 10 minutes before absorbance was measured at 595 nm on a plate reader. BSA concentrations versus the BSA absorbances were used to generate a standard curve and calculate the lysate protein concentrations.

Western blot. Denaturing protein gel electrophoresis was performed according to Invitrogen NuPAGE Bis-Tris Mini Gels user guide. Briefly, protein samples were denatured in LDS Buffer (Invitrogen, NP0007) and Reducing Agent (Invitrogen, NP0009) for 10 minutes at 70°C. Each sample (15 µg) was loaded and run in a NuPAGE 4-12% Bis-Tris gel (Invitrogen, NP0322BOX) on the Mini Gel Tank (Invitrogen) for 45 minutes at 150 volts. Western blotting was then performed according to the Invitrogen General Procedure for Chemiluminescent Western Blotting. Briefly, samples were transferred using the Power Blotter Station (Invitrogen) for seven minutes at 25 volts and 2.5 amps. After transfer, the membrane was blocked in 2% milk and 2% BSA in tris buffered saline with 0.05% tween 20 for one hour with gentle rocking. The membrane was then incubated in CHR3, CHR5, and actin antibodies diluted in 2% milk and 2% BSA in tris buffered saline with 0.05% tween 20 at the designated concentrations overnight at 4°C with gentle rocking. The list of antibodies and working dilutions is provided in Table 2.11. The membrane was then washed three times in tris buffered saline with 0.05% tween 20 for 10 minutes each wash with gentle rocking. The membrane was then incubated in HRP conjugated secondary antibodies diluted in 2% milk and 2% BSA in tris buffered saline with 0.05% tween 20 for two hours with gentle rocking. The membrane was washed again as described above, developed in chemiluminescent substrate, and then immediately imaged on the Odyssey Fc (LI-COR). Protein bands were quantified in Fiji (ImageJ).

Single Nuclei RNA Sequencing

Sample preparation and data collection. Cells were plated in 24 well plates and treated with 10 µM oxaliplatin, 10 µM oxaliplatin with 5 µM oxybutynin, and vehicle containing

medium with 1% water for 24 hours. Cells were dissociated into single cell suspensions by Accutase treatment (Stemcell Technologies, 07920) for 30 minutes at 37 °C, 5% CO₂. Single nuclei suspensions were prepared in duplicate per condition according to 10x Genomics Isolation of Nuclei for Single Cell Sequencing Demonstrated Protocol. Briefly, dissociated cells were lysed on ice in lysis buffer for two minutes and washed with nuclei wash and resuspension buffer and resuspended to 1000 nuclei/μL in nuclei wash and resuspension buffer. Cells were strained to remove cell debris and large clumps then immediately submitted to the UCSF Genomics CoLab for GEM generation & barcoding, post GEM-RT cleanup & cDNA amplification, 3' gene expression library construction, and sequencing on Illumina NovaSeq sequencer according to the 10x Genomics Chromium Next GEM Single Cell 3' Reagent Kits v3.1 User Guide. Gene count matrices were generated using CellRange (v6.0) with alignment to the human reference hg38 transcriptome.

Quality control and cell filtration. Datasets were analyzed in R version 4.2.1 with Seurat version 4.3.0⁶⁰. The number of reads mapping to mitochondrial and ribosomal gene transcripts per cell were calculated using the “PercentageFeatureSet” function. Cells were identified as poor quality and subsequently removed independently for each dataset based on the number of unique features captured per cell, the number of UMI captured per cell and the percentage of reads mapping to mitochondrial transcripts per cell. Dataset specific quality control metric cutoffs can be found in Table 2.8.

Dimensionality reduction, clustering, and annotation. For each biological replicate, quality control metrics were visualized to identify and remove low quality cells (Table 2.8). Counts matrices were log normalized with a scaling factor of 10,000 and 2,000 variable features

were identified using the “vst” method. Count matrices were integrated using Seurat integration functions with default parameters. The variable feature sets were scaled and centered. Principal Components Analysis (PCA) was run using default settings and Uniform Manifold Approximation and Projection (UMAP) dimensionality reduction was performed using the PCA reduction. The shared nearest neighbors (SNN) graph was computed using default settings and cell clustering was performed using the default Louvain algorithm. The number of principal components used for UMAP reduction and SNN calculation was determined by principal component standard deviation and varied for each dataset and can be found in Table 2.9. The above pipeline was performed again for sub-clustering enteric neurons from each biological replicate. Biological replicates per treatment condition were merged using the base R “merge” function and the above pipeline was repeated for each treatment condition. Gene dropout values were imputed using adaptively-thresholded low rank approximation for each treatment condition⁶¹. The rank-k approximation was automatically chosen for each dataset and all other parameters were set as the default values. The imputed gene expression was used to identify cluster-specific expression of cell type marker genes and neurochemical identity genes for the all cells dataset and sub-clustered enteric neuron dataset, respectively.

Curation of published datasets. Curation of the snRNA-seq datasets of primary adult human colon and hPSC-derived stage 1 and stage 2 ganglioid cultures was conducted as previously described by our group³³. For the primary fetal human enteric neuron single cell RNA sequencing dataset, previously published by Teichmann and colleagues, the normalized .H5AD file was downloaded from <https://www.gutcellatlas.org/> and converted into a Seurat object.

Cell type transcriptional signature scoring. To find transcriptionally similar cell populations between our dataset and the primary human adult GI tissue dataset, the differentially expressed genes of the reference dataset were first calculated from the non-imputed gene counts with the “FindAllMarkers” function using the Wilcoxon Rank Sum test and only genes with a positive fold change were returned. Since it was unclear how the drug treatments might affect the genes that are differentially expressed, this analysis was completed with the vehicle-treated cells from our dataset. The query dataset was then scored for the transcriptional signature of each reference dataset cell cluster using the “AddModuleScore” function based on the query dataset’s imputed gene counts.

Neurochemical identification of neurons. The neurochemical identification of neurons was performed independently for each neurotransmitter and neuropeptide to accommodate multi-neurochemical identities. Since it was unclear how the drug treatments might affect the expression of neurochemical identity genes, this analysis was completed with the vehicle-treated neurons from our dataset. For each neurotransmitter, a core set of genes were selected consisting of the rate-limiting synthesis enzyme(s), metabolism enzymes and transport proteins (Table 2.10). Cells were first scored for each neurotransmission associated gene set using the “AddModuleScore” function. A cell was then annotated as “x-ergic” if the cell’s expression of a rate limiting enzyme was greater than 0 and the cell’s module score for the corresponding gene set was greater than 0. A cell was annotated as “other” if both criteria were not met. For each neuropeptide, cells were scored for the gene corresponding with each neuropeptide using the “AddModuleScore” function (Table 2.10). A cell was then annotated as the neuropeptide if the cell’s expression of a gene was greater than 0 or “other” if less than 0. Multi-neurochemical identities were

determined by concatenating the individually determined single neurochemical identities of each cell. The overall prevalence of each neurochemical identity per dataset was calculated by summing the total number of cells annotated for each single identity and calculating the percentage of each identity from this sum total.

Excitotoxicity transcriptional program scoring. To identify the expression level of the excitotoxicity transcriptional program genes in the enteric neuron populations, cells were scored for their expression of each platin excitotoxicity transcriptional program gene category as well as a combined list of all genes in the platin excitotoxicity transcriptional program using the “AddModuleScore” function (Table 2.7).

Pre-ranked gene set enrichment analysis. Genes differentially expressed between the vehicle and oxaliplatin treatment conditions and the oxaliplatin treatment and oxaliplatin-oxybutynin co-treatment conditions for the neurexophilin, nitrenergic, cholecystokinin, cholinergic, secretogranin 1 and glutamatergic-secretogranin 1 populations were identified using the “FindAllMarkers” function using the Wilcoxon Rank Sum test. Pre-ranked GSEA for the MSigDB Hallmark and Ontology gene sets was performed on each subtypes sorted by decreasing \log_2 fold-change using fgsea v1.16. Normalized enrichment scores were calculated for gene sets containing a minimum of 15 or maximum of 500 genes in the differentially expressed gene list. Gene sets significantly changed between the two treatment conditions were identified based on a p-value cutoff of < 0.05 . Gene sets rescued by oxybutynin treatment were identified based on the gene set’s normalized enrichment score being reversed (positive to negative or negative to positive) when comparing the vehicle versus oxaliplatin pre-ranked GSEA results to the oxaliplatin versus oxaliplatin-oxybutynin pre-ranked GSEA results.

MSigDB gene set scoring. Separate gene lists were created containing all genes belonging to each MSigDB Hallmark or Ontology gene set of interest. Cells were scored for their expression of each gene list using the “AddModuleScore” function. For the MSigDB Hallmark gene sets, a combined list of all genes in the Hallmark gene sets was used to generate a combined cellular stress score.

Nitric Oxide Release Assay

Cells were plated in 96 well plates. Pre-treatment supernatants were collected by washing the cells with Tyrode’s solution [NaCl (129 mM), KCl (5 mM), CaCl₂ (2 mM), MgCl₂ (1 mM), glucose (30 mM) and HEPES (25 mM) at pH 7.4]. Cells were then incubated with Tyrode’s solution or 50 μM acetylcholine diluted in Tyrode’s solution for 1 hour at 37°C, 5% CO₂. Supernatants were then removed, centrifuged at 2313g for 10 minutes at 4°C, and frozen at -80°C. Cells were then treated with 10 μM oxaliplatin, vehicle containing medium with 1% water, or 10 μM CCCP for 24 hours. Cells were washed with Tyrode’s solution and incubated with Tyrode’s solution or 50 μM acetylcholine diluted in Tyrode’s solution for 1 hour at 37°C, 5% CO₂. Supernatants were removed, centrifuged at 2313g for 10 minutes at 4°C, and frozen at -80°C. Nitric oxide levels in the supernatants were determined using a nitric oxide assay kit (Invitrogen, EMSNO). Briefly, the kit uses the enzyme nitrate reductase to convert nitrate to nitrite which is then detected as a colored azo dye absorbing light at 540 nm. Nitric oxide release for each well was normalized to the average absorbance of the pre-treatment no acetylcholine stimulation wells. Each dot represents an individually treated well. Statistical analysis for the t=0 hour time point was

performed by Welch's t test. Statistical analysis for the t=24 hour time point was performed by two-way ANOVA with Dunnett correction for multiple comparisons.

Preparation of Paraffin-Embedded Human Stomach Sections

Tissue acquisition. Surplus, tumor-adjacent, archived formalin-fixed paraffin-embedded human stomach tissue sections from prior gastrectomies for gastric cancer were acquired from UCSF pathology under IRB 19-27391. Waiver of consent was authorized by the UCSF IRB. Uninvolved, tumor-adjacent gastric tissue at the margin of the resection were selected, and biospecimens were stratified as having received chemotherapy (platin) treatment prior to gastrectomy or not. Patients with *CDH1* mutations were excluded. Tissue sections were not exhausted, and slides were de-identified prior to processing.

De-paraffin embed tissue. Slides were washed three times in xylene substitute (Sigma-Aldrich, A5597) for five minutes each wash step. Slides were incubated in 100% ethanol for five minutes, 95% ethanol for five minutes, 70% ethanol for five minutes, and finally deionized water for five minutes.

Antigen retrieval. Slides were placed in Antigen Unmasking Solution, Citrate-Based (Vector Laboratories, H-3300-250) in a glass coplin jar. The glass coplin jar was placed in a beaker filled with water and microwaved until the buffer began boiling. The tissue was microwaved for another minute with power set at 50%. The tissue was allowed to cool for a minimum of 30 minutes at room temperature until proceeding with staining.

Staining. Tissue was blocked in 1% triton X and 1% BSA for one hour. Tissue was incubated in primary antibody solution diluted in 1% triton X and 1% BSA overnight at 4°C. Tissue was washed three times with 1% triton X and 1% BSA for 30 minutes each

wash step. Tissue was incubated in secondary antibody solution diluted in 1% triton X and 1% BSA for 1 hour at room temperature. Tissue was washed three times with 1% triton X and 1% BSA for 30 minutes each wash step. Tissue was mounted in Vectashield HardSet Antifade Mounting Medium (Vector Laboratories, H-1400).

Imaging and analysis of p-PKC. High-throughput imaging was carried out using the ImageXpress Confocal HT.ai (Molecular Devices). Neuronal p-PKC levels were detected based on the overlap of p-PKC and TUBB3 signals with the MetaXpress High-Content Image Acquisition and Analysis Software. Representative images were taken with the ImageXpress Confocal HT.ai (Molecular Devices) and processed using Adobe Photoshop software. Neuronal p-PKC integrated intensities were normalized by TUBB3 total area. Each dot represents a region of interest. Data were collected from five regions of interest from eight patients. Statistical analysis was performed by Welch's t test.

Imaging and analysis of nitroergic and cholinergic neurons. High-throughput imaging was carried out using the ImageXpress Confocal HT.ai (Molecular Devices). Nitroergic neurons were detected based on the overlap of NOS1 and HuC/D signals, cholinergic neurons were detected based on the overlap of CHAT and HuC/D signals, and CHAT+ NOS1+ neurons were detected based on the overlap of nitroergic neurons with cholinergic neurons with the MetaXpress High-Content Image Acquisition and Analysis Software. Representative images were taken with the ImageXpress Confocal HT.ai (Molecular Devices) and processed using Adobe Photoshop software. NOS1+ CHAT- neurons were calculated by subtracting the nitroergic neuron total number by the CHAT+ NOS1+ neuron total number. CHAT+ NOS1- neurons were calculated by subtracting the cholinergic neuron total number by the CHAT+ NOS1+ neuron total number. Each of the three

populations (NOS1+ CHAT- neurons, CHAT+ NOS1- neurons, and CHAT+ NOS1+ neurons) were normalized by their combined total number to calculate each population's percent representation. Each dot represents a region of interest. Data were collected from five regions of interest from eight patients. Statistical analysis was performed by Welch's t test.

Mouse Treatment Protocols

Preparation of solutions for injection. All solutions were prepared fresh for each injection day. A 1 mM stock solution of oxaliplatin (Sigma-Aldrich, Y0000271) was prepared by dissolving it in sterile water by vortexing vigorously and then was sterilized by filtration with a 0.22 μm filter prior to injection. Oxaliplatin's vehicle was prepared by filtering sterile water with a 0.22 μm filter prior to injection. A 71.1 mg/mL stock solution of oxybutynin (SelleckChem, S1754) was prepared in DMSO, then diluted to 3.6 mg/mL (5%) in 2% tween80 in sterile saline and was sterilized by filtration with a 0.22 μm filter prior to injection. Oxybutynin's vehicle was prepared by diluting DMSO (5%) in 2% tween80 in sterile saline and was sterilized by filtration with a 0.22 μm filter prior to injection.

Intraperitoneal injections. Mice received intraperitoneal injections every three days for five total injection days. Vehicle-treated mice received injections of oxaliplatin's vehicle (3 mg/kg per dose) and oxybutynin's vehicle (35 mg/kg per dose). Oxybutynin-treated mice received injections of oxaliplatin's vehicle (3 mg/kg per dose) and oxybutynin (35 mg/kg per dose). Oxaliplatin-treated mice received injections of oxaliplatin (3 mg/kg per dose) and oxybutynin's vehicle (35 mg/kg per dose). Oxaliplatin-oxybutynin co-treated mice received injections of oxaliplatin (3 mg/kg per dose) and oxybutynin (35 mg/kg per dose).

GI transit time. Mice were gavaged with 0.2 ml of dye solution containing 6% carmine, 0.5% methylcellulose, and 0.9% NaCl, using a #24 round-tip feeding needle. The needle was held inside the mouse esophagus for a few seconds after gavage to prevent regurgitation. One hour later, the stool color was monitored for gavaged mice every 10 minutes. For each mouse, total GI transit time is between the time of gavage and the time when red stool is observed. Each dot-line pairing represents an individual mouse. Statistical analysis was performed by two-way ANOVA with Šidák correction for multiple comparisons.

Preparation of Whole Mount Mouse Colon Tissue

Following the excision, the entire colon was pinned in a Sylgard (Dow) lined petri dish and opened along the mesenteric border. The tissue was fixed in 4% paraformaldehyde (Santa Cruz, sc-281692) in PBS for approximately 45 minutes at room temperature. The proximal half of the colon was separated from the distal half, and both were stored in PBS at 4°C.

Whole Mount Imaging and Analysis

Staining. Tissue was blocked in 1% triton X and 1% BSA for one hour with rocking and incubated in primary antibody solution diluted in 1% triton X and 1% BSA overnight at 4°C. Tissue was washed three times with 1% triton X and 1% BSA for 30 minutes each wash step with rocking. Tissue was incubated in secondary antibody solution diluted in 1% triton X and 1% BSA for one hour at room temperature. Tissue was washed three

times with 1% triton X and 1% BSA for 30 minutes each wash step with rocking. Tissue was stored in PBS at 4°C.

Imaging. High-throughput imaging was carried out using the ImageXpress Confocal HT.ai (Molecular Devices). Nitroergic neurons were detected based on the overlap of NOS1 staining with HuC/D staining, cholinergic neurons were detected based on the overlap of CHAT staining and HuC/D staining, and the total number of neurons was measured by HuC/D staining with the MetaXpress High-Content Image Acquisition and Analysis Software. The proportion of nitroergic neurons was calculated by normalizing the total number of nitroergic neurons by the total number of neurons. The proportion of cholinergic neurons was calculated by normalizing the total number of cholinergic neurons by the total number of neurons. Each dot represents an individual mouse. Statistical analysis was performed by Brown-Forsythe and Welch one-way ANOVA with Dunnett T3 correction for multiple comparisons. Representative images were taken with the ImageXpress Confocal HT.ai (Molecular Devices) and processed using Adobe Photoshop software.

Generating Figure Schematics

Schematics for the figures were generated using BioRender. <https://biorender.com/>

Chapter 3 Concluding Remarks

3.1 Overview of our findings

Enteric neurons innervate and control the GI tract^{62,63}. Environmental factors, such as chemotherapy treatment, can damage enteric neurons, causing a variety of GI functional defects, like chemotherapy-induced constipation^{8–11,28,42}. Platin chemotherapies contribute heavily to the burden of chemotherapy-induced GI neurotoxicity, causing symptoms that can be dose-limiting and irreversible, significantly impacting quality of life⁶⁴. However, despite being on the market for decades, the cell type-specific mechanisms underlying platin-induced GI neurotoxicity have remained largely unknown.

Here, we leveraged hPSC-derived enteric neurons as a novel model system to study platin-induced enteric neuropathy. Our study identifies that cholinergic signaling mediates an excitotoxicity cascade that potentiates neuropathy in enteric neurons. Notably, increased expression of the excitotoxicity transcriptional program genes sensitizes certain enteric neuron subtypes, such as nitrenergic enteric neurons, to the excitotoxicity cascade, thus making them selectively vulnerable to platins. These observations provide strong evidence for the role of muscarinic cholinergic receptor antagonism as a therapeutic mechanism to preserve susceptible enteric neuron subtypes from toxicity, thereby preserving gut functions during and after platin chemotherapy treatment.

Our comprehensive phenotypic and transcriptomic profiling revealed that the enteric nerves are more sensitive to platins relative to the other peripheral nerve populations. For example, enteric neurons showed a higher cytotoxic response and neuroinflammatory signature. We demonstrated that platins induce DNA damage, oxidative stress, neurite degeneration, and apoptosis in enteric neurons. Given that all experiments were performed in *in vitro* cultures of enteric neurons, without confounding interactions with other tissues in the GI microenvironment, these data suggest that platin-induced enteric neuropathy occurs as a result of the direct effect of platins on enteric neurons. Thus, identifying and blocking the mechanism that makes enteric neurons highly sensitive to platins would be an effective therapeutic strategy to protect this vulnerable tissue.

Taking advantage of the scalability of our hPSC-derived platin-induced enteric neuropathy model system, we performed high-throughput screening to identify drugs that regulate platin-induced enteric neuron cell death. A common characteristic of the drugs from our screen was the ability to target GPCRs. Analysis of the two GPCR classes represented in the dataset revealed that antagonizing the G_q-mediated inositol phospholipid signaling pathway can preserve enteric neuron viability during oxaliplatin treatment, suggesting platin-induced enteric neuropathy is potentiated via a G_q GPCR-mediated excitotoxicity mechanism. Indeed, we found that oxaliplatin causes enteric neurons to become hyperexcitable within a few hours of treatment, triggering the excitotoxicity cascade. Furthermore, treatment with our drug candidate oxybutynin, which is a potent muscarinic cholinergic receptor antagonist, blocks the G_q GPCR-mediated excitotoxicity cascade through CHRM3 and CHRM5. Notably, in colorectal cancer cell

lines, dosing oxybutynin in combination with platins does not affect the efficacy of platins in killing cancer cells, making oxybutynin an ideal candidate for combination therapy in the clinic.

The ability of the enteric neurons to control diverse GI function relies on the diversity of enteric neuron subtypes represented in the ENS across different regions of the gut^{53,65,66}. Thus, to understand how platins affect different enteric neuron subtypes, we performed snRNA-seq of our hPSC-derived enteric neurons treated with vehicle, oxaliplatin, and oxaliplatin-oxybutynin co-treatment. By transcriptomic profiling and further phenotypic validation, we demonstrated that nitrergic neurons are selectively vulnerable to platins. Furthermore, oxybutynin co-treatment was sufficient to reverse toxicity related transcriptional signatures specifically in the subtypes predicted to be most vulnerable. This analysis highlights the importance of using relevant cellular models to study disease mechanisms or drug toxicity. Although we discovered antagonizing CHRM3 and CHRM5 can prevent toxicity in enteric neurons, the representation of these receptors as well as other effectors within the platin excitotoxicity transcriptional program serves as a platin sensitivity dial that either turns up or down platin-induced toxicity in specific enteric neuron subtypes. Thus, identifying the protein network responsible for toxicity within a specific cellular context can help uncover the mechanisms underlying the cell type specificity of the disease.

Platin-induced enteric neuropathy has been detected in nearly every region of the GI, indicating that toxicity is not region specific and that clinical manifestations of platin-

induced enteric neuropathy could vary widely, from chemotherapy-induced achalasia, gastroparesis, or constipation^{8–11,28,42}. Indeed, we observed that patients that received platin chemotherapy treatment prior to their tumor resection surgery showed altered representation of enteric neuron subtypes in their stomach. The nitrergic neuron population, which we identified as selectively vulnerable to platins, was significantly reduced, whereas the cholinergic neuron population, which we identified as more resistant to platins, was significantly elevated. This overrepresentation of cholinergic neurons is likely a consequence of nitrergic neurons getting selectively eliminated by platins. This observation was consistent with the results of our mouse study where oxaliplatin significantly reduced nitrergic neuron levels and significantly increased cholinergic neuron levels; oxybutynin co-treatment was able to prevent this disruption in neuronal ratio. Furthermore, we found that co-administration of oxybutynin with oxaliplatin was able to prevent oxaliplatin-induced constipation in these animals, highlighting its therapeutic potential to prevent cellular and physiological hallmarks of platin-induced GI neuropathy.

In conclusion, our hPSC-derived model of platin-induced enteric neuropathy enabled the discovery of the mechanism underlying the selective vulnerability of enteric neurons and enteric neuron subtypes to platin chemotherapies. The work implicates an excitotoxicity cascade in the pathogenesis of platin-induced enteric neuropathy and presents muscarinic cholinergic receptor antagonism as an effective therapeutic strategy to prevent excitotoxicity and enteric neuropathy both *in vitro* and *in vivo*. Lastly, this work exemplifies how hPSC technology can enable disease modeling and drug discovery for

peripheral neuropathies, serving as a roadmap for uncovering the cell type-specific responses to cellular stress underlying these historically intractable disorders.

3.2 Perspectives and future directions

Chemotherapy drugs have been an approved and established part of cancer treatment regimens for decades and yet their common and dose-limiting side effect of peripheral neurotoxicity has remained unchecked and uncontrolled. This is largely due to a lack of mechanistic insights underlying these drug-induced neuropathies. I posit in Chapter 1 that this is due to the technical challenges and translational limitations of studying the PNS solely in animal models, which is how most chemotherapy-induced peripheral neuropathy research has been conducted to date. Instead, I suggest adopting an interdisciplinary approach leveraging stem cell-based models to uncover drug toxicity mechanisms and mouse models to validate therapeutic findings, including a successful example of this framework in Chapter 2.

However, chemotherapy-induced peripheral neuropathy and cancer neuroscience research are ever evolving fields, and much is unresolved. With stem cell-based models of sensory neurons²⁵, motor neurons⁶⁷⁻⁶⁹, enteric neurons^{5,32,33}, and most recently Schwann cells⁷⁰, we may begin incorporating new unbiased tools, such as high throughput genetic or pharmacologic phenotypic screens, to further understand how different chemotherapies affect different cell types in the PNS, enabling the identification of proteins involved in PNS cell type specific susceptibility to chemotherapies.

Furthermore, with robust cellular biomarkers of chemotherapy-induced peripheral neuropathy, we may begin to explore how these proteins relate to various neuropathy hallmarks, such as aberrant electrophysiology, neurite degeneration, and cell death. Moreover, these findings may be leveraged to prevent PNS toxicity. For example, early biomarkers detected in stem cell-based models may be leveraged clinically to detect neuropathy onset, preventing the most deleterious symptoms. Otherwise, a robust understanding of potential therapeutic mechanisms would enable the employment of cancer models to validate the clinical relevance of potential neuroprotective therapies. Drug candidates capable of preventing neuropathy may be evaluated in the clinic to prevent symptoms, reducing the number of patients that must taper or discontinue treatment. These efforts will not only aid our understanding of chemotherapy-induced peripheral neuropathy but will help make available therapies safer and more effective.

PNS stem cell biology is currently advancing and evolving as well, and some gaps remain to be filled. For example, differentiation protocols to derive some PNS lineages remain to be developed and optimized. Some tissues, such as enteric glia, remain difficult to access because no efficient differentiation protocols have been invented yet. Additionally, unlike the central nervous system where distinct populations, such as cortical neurons or midbrain dopaminergic neurons, may be derived with high efficiency, ENS differentiation protocols are heterogenous, reflecting the cellular diversity found *in vivo*. Thus, to better uncover how various transcriptionally and functionally distinct cell types contribute to ENS function in health and disease, protocols capable of efficiently deriving distinct enteric neuron subtypes are needed and are beginning to emerge³³. Furthermore, when new

differentiation protocols are developed, it is essential that the derived cell types are confirmed to be transcriptionally, morphologically, and functionally similar to primary tissue samples, validating their status as a bona fide PNS subtype of interest and a reliable stem cell model.

Lastly, in recent years, cancer drug discovery efforts have shifted toward the development of targeted therapies. These include small molecule inhibitors that inhibit oncogenic signaling pathways, or biologics that recruit immune cells to cancer cells overexpressing an epitope. Given their design to interact with specific proteins present in or on cancer cells, it was presumed that targeted therapies would be safer than their chemotherapy counterparts. However, many of these newer drugs have replicated similar adverse effects in the clinic, including neurotoxicity⁷¹⁻⁷³. Due to the combinatorial nature of cancer treatment, targeted cancer drugs are not replacing chemotherapy but are often given in addition to chemotherapy. Therefore, it is becoming more likely that a patient will experience some form of drug-induced peripheral neuropathy. Thus, research efforts must be implemented to understand the mechanisms of peripheral nerve toxicity induced by all cancer therapies.

In conclusion, as more scientists begin leveraging the strengths of human stem cell-based models in tandem with traditional mouse models, the mechanisms underlying cancer therapy-induced peripheral neuropathy will be better characterized, novel clinically relevant drug candidates will be uncovered, thus enabling the development of safer and more effective cancer treatment regimens.

References

1. Saito-Diaz, K. & Zeltner, N. Induced pluripotent stem cells for disease modeling, cell therapy and drug discovery in genetic autonomic disorders: a review. *Clin. Auton. Res. Off. J. Clin. Auton. Res. Soc.* **29**, 367–384 (2019).
2. Drokhlyansky, E. *et al.* The Human and Mouse Enteric Nervous System at Single-Cell Resolution. *Cell* **182**, 1606-1622.e23 (2020).
3. Cappella, M., Pradat, P.-F., Querin, G. & Biferi, M. G. Beyond the Traditional Clinical Trials for Amyotrophic Lateral Sclerosis and The Future Impact of Gene Therapy. *J. Neuromuscul. Dis.* **8**, 25–38 (2021).
4. Lee, G. *et al.* Large-scale screening using familial dysautonomia induced pluripotent stem cells identifies compounds that rescue IKBKAP expression. *Nat. Biotechnol.* **30**, 1244–1248 (2012).
5. Fattahi, F. *et al.* Deriving human ENS lineages for cell therapy and drug discovery in Hirschsprung disease. *Nature* **531**, 105–109 (2016).
6. Samuel, R. M. *et al.* Androgen Signaling Regulates SARS-CoV-2 Receptor Levels and Is Associated with Severe COVID-19 Symptoms in Men. *Cell Stem Cell* **27**, 876-889.e12 (2020).
7. Furness, J. B. *The enteric nervous system.* (Blackwell Pub, 2006).
8. McQuade, R. M. *et al.* Oxaliplatin-induced enteric neuronal loss and intestinal dysfunction is prevented by co-treatment with BGP-15. *Br. J. Pharmacol.* **175**, 656–677 (2018).

9. McQuade, R. M. *et al.* Role of oxidative stress in oxaliplatin-induced enteric neuropathy and colonic dysmotility in mice. *Br. J. Pharmacol.* **173**, 3502–3521 (2016).
10. Wafai, L. *et al.* Effects of oxaliplatin on mouse myenteric neurons and colonic motility. *Front. Neurosci.* **7**, 30 (2013).
11. Vera, G. *et al.* Enteric neuropathy evoked by repeated cisplatin in the rat. *Neurogastroenterol. Motil. Off. J. Eur. Gastrointest. Motil. Soc.* **23**, 370–378, e162-163 (2011).
12. Burgess, J. *et al.* Chemotherapy-Induced Peripheral Neuropathy: Epidemiology, Pathomechanisms and Treatment. *Oncol. Ther.* **9**, 385–450 (2021).
13. Burridge, P. W. *et al.* Human induced pluripotent stem cell-derived cardiomyocytes recapitulate the predilection of breast cancer patients to doxorubicin-induced cardiotoxicity. *Nat. Med.* **22**, 547–556 (2016).
14. Cheung, Y.-F. *et al.* Circulating high-sensitivity troponin T and microRNAs as markers of myocardial damage during childhood leukaemia treatment. *Pediatr. Res.* **89**, 1245–1252 (2021).
15. Weaver, B. A. How Taxol/paclitaxel kills cancer cells. *Mol. Biol. Cell* **25**, 2677–2681 (2014).
16. Yardley, D. A. nab-Paclitaxel mechanisms of action and delivery. *J. Controlled Release* **170**, 365–372 (2013).
17. Klein, I. & Lehmann, H. C. Pathomechanisms of Paclitaxel-Induced Peripheral Neuropathy. *Toxics* **9**, 229 (2021).

18. Chua, K. C., El-Haj, N., Priotti, J. & Kroetz, D. L. Mechanistic insights into the pathogenesis of microtubule-targeting agent-induced peripheral neuropathy from pharmacogenetic and functional studies. *Basic Clin. Pharmacol. Toxicol.* **130 Suppl 1**, 60–74 (2022).
19. Staff, N. P. *et al.* Pathogenesis of paclitaxel-induced peripheral neuropathy: A current review of in vitro and in vivo findings using rodent and human model systems. *Exp. Neurol.* **324**, 113121 (2020).
20. Pease-Raissi, S. E. *et al.* Paclitaxel Reduces Axonal Bclw to Initiate IP3R1-Dependent Axon Degeneration. *Neuron* **96**, 373-386.e6 (2017).
21. Li, Y. *et al.* The Cancer Chemotherapeutic Paclitaxel Increases Human and Rodent Sensory Neuron Responses to TRPV1 by Activation of TLR4. *J. Neurosci. Off. J. Soc. Neurosci.* **35**, 13487–13500 (2015).
22. Schinke, C. *et al.* Modeling chemotherapy induced neurotoxicity with human induced pluripotent stem cell (iPSC) -derived sensory neurons. *Neurobiol. Dis.* **155**, 105391 (2021).
23. Xiong, C. *et al.* Human Induced Pluripotent Stem Cell Derived Sensory Neurons are Sensitive to the Neurotoxic Effects of Paclitaxel. *Clin. Transl. Sci.* **14**, 568–581 (2021).
24. Chua, K. C. *et al.* Genomewide Meta-Analysis Validates a Role for S1PR1 in Microtubule Targeting Agent-Induced Sensory Peripheral Neuropathy. *Clin. Pharmacol. Ther.* **108**, 625–634 (2020).

25. Chambers, S. M. *et al.* Combined small molecule inhibition accelerates developmental timing and converts human pluripotent stem cells into nociceptors. *Nat. Biotechnol.* **30**, 715–720 (2012).
26. Oun, R., Moussa, Y. E. & Wheate, N. J. The side effects of platinum-based chemotherapy drugs: a review for chemists. *Dalton Trans. Camb. Engl.* **2003** **47**, 6645–6653 (2018).
27. Ramsey, S. D., Berry, K., Moinpour, C., Giedzinska, A. & Andersen, M. R. Quality of life in long term survivors of colorectal cancer. *Am. J. Gastroenterol.* **97**, 1228–1234 (2002).
28. Robinson, A. M. *et al.* Effects of Oxaliplatin Treatment on the Enteric Glial Cells and Neurons in the Mouse Ileum. *J. Histochem. Cytochem. Off. J. Histochem. Soc.* **64**, 530–545 (2016).
29. Brehmer, A. Classification of human enteric neurons. *Histochem. Cell Biol.* **156**, 95–108 (2021).
30. Fung, C. & Vanden Berghe, P. Functional circuits and signal processing in the enteric nervous system. *Cell. Mol. Life Sci. CMLS* **77**, 4505–4522 (2020).
31. Bódi, N., Szalai, Z. & Bagyánszki, M. Nitroergic Enteric Neurons in Health and Disease-Focus on Animal Models. *Int. J. Mol. Sci.* **20**, E2003 (2019).
32. Barber, K., Studer, L. & Fattahi, F. Derivation of enteric neuron lineages from human pluripotent stem cells. *Nat. Protoc.* **14**, 1261–1279 (2019).
33. Majd, H. *et al.* hPSC-Derived Enteric Ganglioids Model Human ENS Development and Function. 2022.01.04.474746 Preprint at <https://doi.org/10.1101/2022.01.04.474746> (2022).

34. Johnstone, T. C., Suntharalingam, K. & Lippard, S. J. Third row transition metals for the treatment of cancer. *Philos. Transact. A Math. Phys. Eng. Sci.* **373**, 20140185 (2015).
35. Kris, M. G., Gralla, R. J., Clark, R. A., Tyson, L. B. & Groshen, S. Control of chemotherapy-induced diarrhea with the synthetic enkephalin BW942C: a randomized trial with placebo in patients receiving cisplatin. *J. Clin. Oncol. Off. J. Am. Soc. Clin. Oncol.* **6**, 663–668 (1988).
36. Vasey, P. A. *et al.* Phase III randomized trial of docetaxel-carboplatin versus paclitaxel-carboplatin as first-line chemotherapy for ovarian carcinoma. *J. Natl. Cancer Inst.* **96**, 1682–1691 (2004).
37. Zhu, X. *et al.* Phase II clinical trial of advanced and metastatic gastric cancer based on continuous infusion of 5-fluorouracil combined with epirubicin and oxaliplatin. *J. Cancer Res. Clin. Oncol.* **134**, 929–936 (2008).
38. Levi, F. *et al.* Oxaliplatin activity against metastatic colorectal cancer. A phase II study of 5-day continuous venous infusion at circadian rhythm modulated rate. *Eur. J. Cancer Oxf. Engl. 1990* **29A**, 1280–1284 (1993).
39. Rivera, L. R., Poole, D. P., Thacker, M. & Furness, J. B. The involvement of nitric oxide synthase neurons in enteric neuropathies. *Neurogastroenterol. Motil. Off. J. Eur. Gastrointest. Motil. Soc.* **23**, 980–988 (2011).
40. Wood, J. D. Enteric Nervous System: Neuropathic Gastrointestinal Motility. *Dig. Dis. Sci.* **61**, 1803–1816 (2016).

41. Holland, A. M., Bon-Frauches, A. C., Keszthelyi, D., Melotte, V. & Boesmans, W. The enteric nervous system in gastrointestinal disease etiology. *Cell. Mol. Life Sci.* **78**, 4713–4733 (2021).
42. Pini, A. *et al.* Glucagon-like peptide 2 counteracts the mucosal damage and the neuropathy induced by chronic treatment with cisplatin in the mouse gastric fundus. *Neurogastroenterol. Motil. Off. J. Eur. Gastrointest. Motil. Soc.* **28**, 206–216 (2016).
43. Zeltner, N. *et al.* Capturing the biology of disease severity in a PSC-based model of familial dysautonomia. *Nat. Med.* **22**, 1421–1427 (2016).
44. Shabab, T., Khanabdali, R., Moghadamtousi, S. Z., Kadir, H. A. & Mohan, G. Neuroinflammation pathways: a general review. *Int. J. Neurosci.* **127**, 624–633 (2017).
45. Wick, W. *et al.* Phase III study of enzastaurin compared with lomustine in the treatment of recurrent intracranial glioblastoma. *J. Clin. Oncol. Off. J. Am. Soc. Clin. Oncol.* **28**, 1168–1174 (2010).
46. Rocha, C. R. R., Silva, M. M., Quinet, A., Cabral-Neto, J. B. & Menck, C. F. M. DNA repair pathways and cisplatin resistance: an intimate relationship. *Clin. Sao Paulo Braz.* **73**, e478s (2018).
47. Goldar, S., Khaniani, M. S., Derakhshan, S. M. & Baradaran, B. Molecular mechanisms of apoptosis and roles in cancer development and treatment. *Asian Pac. J. Cancer Prev. APJCP* **16**, 2129–2144 (2015).
48. Keiser, M. J. *et al.* Relating protein pharmacology by ligand chemistry. *Nat. Biotechnol.* **25**, 197–206 (2007).

49. Szklarczyk, D. *et al.* STRING v11: protein-protein association networks with increased coverage, supporting functional discovery in genome-wide experimental datasets. *Nucleic Acids Res.* **47**, D607–D613 (2019).
50. Syrovatkina, V., Alegre, K. O., Dey, R. & Huang, X.-Y. Regulation, Signaling, and Physiological Functions of G-Proteins. *J. Mol. Biol.* **428**, 3850–3868 (2016).
51. Tehse, J. & Taghibiglou, C. The overlooked aspect of excitotoxicity: Glutamate-independent excitotoxicity in traumatic brain injuries. *Eur. J. Neurosci.* **49**, 1157–1170 (2019).
52. Chapple, C. R. Muscarinic receptor antagonists in the treatment of overactive bladder. *Urology* **55**, 33–46; discussion 50 (2000).
53. Niesler, B., Kuerten, S., Demir, I. E. & Schäfer, K.-H. Disorders of the enteric nervous system - a holistic view. *Nat. Rev. Gastroenterol. Hepatol.* **18**, 393–410 (2021).
54. De Giorgio, R. *et al.* Enteric neuropathies: Yesterday, Today and Tomorrow. *Adv. Exp. Med. Biol.* **891**, 123–133 (2016).
55. Elmentaite, R. *et al.* Cells of the human intestinal tract mapped across space and time. *Nature* **597**, 250–255 (2021).
56. Morarach, K. *et al.* Diversification of molecularly defined myenteric neuron classes revealed by single-cell RNA sequencing. *Nat. Neurosci.* **24**, 34–46 (2021).
57. Wright, C. M. *et al.* scRNA-Seq Reveals New Enteric Nervous System Roles for GDNF, NRTN, and TBX3. *Cell. Mol. Gastroenterol. Hepatol.* **11**, 1548-1592.e1 (2021).


58. May-Zhang, A. A. *et al.* Combinatorial Transcriptional Profiling of Mouse and Human Enteric Neurons Identifies Shared and Disparate Subtypes In Situ. *Gastroenterology* **160**, 755-770.e26 (2021).
59. Tchieu, J. *et al.* A Modular Platform for Differentiation of Human PSCs into All Major Ectodermal Lineages. *Cell Stem Cell* **21**, 399-410.e7 (2017).
60. Hao, Y. *et al.* Integrated analysis of multimodal single-cell data. *Cell* **184**, 3573-3587.e29 (2021).
61. Linderman, G. C., Zhao, J. & Kluger, Y. *Zero-preserving imputation of scRNA-seq data using low-rank approximation*. <http://biorxiv.org/lookup/doi/10.1101/397588> (2018) doi:10.1101/397588.
62. Fung, C. & Vanden Berghe, P. Functional circuits and signal processing in the enteric nervous system. *Cell. Mol. Life Sci. CMLS* **77**, 4505–4522 (2020).
63. Brehmer, A. Classification of human enteric neurons. *Histochem. Cell Biol.* **156**, 95–108 (2021).
64. Ramsey, S. D., Berry, K., Moinpour, C., Giedzinska, A. & Andersen, M. R. Quality of life in long term survivors of colorectal cancer. *Am. J. Gastroenterol.* **97**, 1228–1234 (2002).
65. Camilleri, M. Gastrointestinal motility disorders in neurologic disease. *J. Clin. Invest.* **131**, 143771 (2021).
66. Yoo, B. B. & Mazmanian, S. K. The Enteric Network: Interactions between the Immune and Nervous Systems of the Gut. *Immunity* **46**, 910–926 (2017).
67. Lee, H. *et al.* Directed Differentiation and Transplantation of Human Embryonic Stem Cell-Derived Motoneurons. *Stem Cells* **25**, 1931–1939 (2007).

68. Chambers, S. M. *et al.* Highly efficient neural conversion of human ES and iPS cells by dual inhibition of SMAD signaling. *Nat. Biotechnol.* **27**, 275–280 (2009).
69. Takazawa, T. *et al.* Maturation of Spinal Motor Neurons Derived from Human Embryonic Stem Cells. *PLoS ONE* **7**, e40154 (2012).
70. Majd, H. *et al.* *Deriving Schwann Cells from hPSCs Enables Disease Modeling and Drug Discovery for Diabetic Peripheral Neuropathy.*
<http://biorxiv.org/lookup/doi/10.1101/2022.08.16.504209> (2022)
doi:10.1101/2022.08.16.504209.
71. Bertolizio, G. *et al.* Multimodal Analgesic Plan for Children Undergoing Chimeric 14.18 Immunotherapy. *J. Pediatr. Hematol. Oncol.* **43**, e169–e172 (2021).
72. Zhong, L. *et al.* Small molecules in targeted cancer therapy: advances, challenges, and future perspectives. *Signal Transduct. Target. Ther.* **6**, 201 (2021).
73. Yan, W. *et al.* The molecular and cellular insight into the toxicology of bortezomib-induced peripheral neuropathy. *Biomed. Pharmacother. Biomedecine Pharmacother.* **142**, 112068 (2021).

Publishing Agreement

It is the policy of the University to encourage open access and broad distribution of all theses, dissertations, and manuscripts. The Graduate Division will facilitate the distribution of UCSF theses, dissertations, and manuscripts to the UCSF Library for open access and distribution. UCSF will make such theses, dissertations, and manuscripts accessible to the public and will take reasonable steps to preserve these works in perpetuity.

I hereby grant the non-exclusive, perpetual right to The Regents of the University of California to reproduce, publicly display, distribute, preserve, and publish copies of my thesis, dissertation, or manuscript in any form or media, now existing or later derived, including access online for teaching, research, and public service purposes.

DocuSigned by:

F20648332BB24F7... Author Signature

3/10/2023
Date